



A strain-programmed patch for the healing of diabetic wounds

Georgios Theocharidis^{1,12}, Hyunwoo Yuk^{2,10,12}✉, Heejung Roh^{2,12}, Liu Wang^{2,11,12}, Ikram Mezghani¹, Jingjing Wu^{2,3}, Antonios Kafanas⁴, Mauricio Contreras⁵, Brandon Sumpio¹, Zhuqing Li¹, Enya Wang¹, Lihong Chen¹, Chuan Fei Guo³, Navin Jayaswal¹, Xanthi-Leda Katopodi⁶, Nikolaos Kalavros⁶, Christoph S. Nabzdyk⁷, Ioannis S. Vlachos^{6,8}, Aristidis Veves¹✉ and Xuanhe Zhao^{2,9}✉

Diabetic foot ulcers and other chronic wounds with impaired healing can be treated with bioengineered skin or with growth factors. However, most patients do not benefit from these treatments. Here we report the development and preclinical therapeutic performance of a strain-programmed patch that rapidly and robustly adheres to diabetic wounds, and promotes wound closure and re-epithelialization. The patch consists of a dried adhesive layer of crosslinked polymer networks bound to a pre-stretched hydrophilic elastomer backing, and implements a hydration-based shape-memory mechanism to mechanically contract diabetic wounds in a programmable manner on the basis of analytical and finite-element modelling. In mouse and human skin, and in mini-pigs and humanized mice, the patch enhanced the healing of diabetic wounds by promoting faster re-epithelialization and angiogenesis, and the enrichment of fibroblast populations with a pro-regenerative phenotype. Strain-programmed patches might also be effective for the treatment of other forms of acute and chronic wounds.

Impaired wound healing capability and consequent chronic wounds, such as diabetic foot ulcers (DFU), are one of the major and rapid growing complications in diabetic patients, with over 750,000 new DFU each year^{1,2}. Chronic DFU inflict substantial clinical and economic burdens including 70,000 lower-extremity amputations, a dramatic reduction in life quality² and associated costs reaching over US\$11 billion annually in the United States alone³. Although various therapeutic strategies, such as bioengineered skin^{4,5} and growth factor-based treatments⁶, have been introduced in clinical practice in the past few decades, their benefits are rather limited as more than 50% of treated DFU patients fail to respond^{7,8}. The rapidly rising number of diabetic patients worldwide and the lack of effective treatment highlight the critical importance of developing new therapeutic solutions for diabetic wound healing.

Mechanical modulation of wounded or scarred skin has been a promising strategy to repair and remodel the skin in both animal models and human clinical trials^{9–15}. In addition, animal studies have indicated that the reduced contractility of diabetic wounds compared with non-diabetic wounds is one of the sources of impaired diabetic wound healing^{7,13,16–18}. We recently discovered a fibroblast subpopulation with increased expression of extracellular matrix (ECM) remodelling and inflammatory response-related genes uniquely present in DFU that successfully heal¹⁹. This suggests that mesenchymal cells play an important role in regulating diabetic wound repair and given their well-known mechanore-

sponsive nature²⁰, manipulating tissue mechanics could favourably impact healing outcomes. Therefore, mechanical modulation such as inducing contraction of diabetic wounds can be an attractive approach to accelerate diabetic wound healing. However, the potential therapeutic benefits of the mechanical modulation approach have not been well investigated for diabetic wounds such as DFU due to several technical limitations. Existing wound dressings and bandages in the standard-of-care for diabetic skin wounds lack the capabilities to form rapid and robust adhesion on wet wounded skin over the long term (for example, days) or to provide precisely programmed mechanical contraction for wounds (Fig. 1a–c), limiting their use only for passive coverage, ineffective and uncontrolled contraction, and/or fully closed wounds^{21–23}. To the best of our knowledge, there exists no method that can provide precisely controlled and long-term contraction on wet wounded skin, leaving this potential therapeutic strategy untapped for diabetic wounds.

We have shown a strain-programmed patch for the controlled and consistent mechanical modulation of wet wounded tissues over days, and for the accelerated healing of diabetic wounds (Fig. 1d,e). The strain-programmed patch synergistically combines a dry-crosslinking mechanism²⁴ and a hydration-based shape-memory mechanism to simultaneously achieve robust, long-lasting and on-demand detachable adhesion on diabetic wounds and precisely controlled mechanical modulation of the wounds (resolved stress concentration at wound edge, wound

¹Joslin-Beth Israel Deaconess Foot Center and The Rongxiang Xu, MD, Center for Regenerative Therapeutics, Beth Israel Deaconess Medical Center, Harvard Medical School, Boston, MA, USA. ²Department of Mechanical Engineering, Massachusetts Institute of Technology, Cambridge, MA, USA. ³Department of Materials Science and Engineering, Southern University of Science and Technology, Shenzhen, China. ⁴Lincoln County Hospital, Northern Lincolnshire and Goole NHS Foundation Trust, Lincoln, Lincolnshire, UK. ⁵Division of Vascular Surgery, Department of Surgery, Beth Israel Deaconess Medical Center, Harvard Medical School, Boston, MA, USA. ⁶Cancer Research Institute, HMS Initiative for RNA Medicine, Department of Pathology, Beth Israel Deaconess Medical Center, Harvard Medical School, Boston, MA, USA. ⁷Department of Anesthesiology and Perioperative Medicine, Mayo Clinic, Rochester, MN, USA. ⁸Broad Institute of MIT and Harvard, Cambridge, MA, USA. ⁹Department of Civil and Environmental Engineering, Massachusetts Institute of Technology, Cambridge, MA, USA. ¹⁰Present address: SanaHeal, Inc., Boston, MA, USA. ¹¹Present address: CAS Key Laboratory of Mechanical Behavior and Design of Materials, Department of Modern Mechanics, University of Science and Technology of China, Hefei, Anhui, China. ¹²These authors contributed equally: Georgios Theocharidis, Hyunwoo Yuk, Heejung Roh, Liu Wang. These authors jointly supervised this work: Aristidis Veves, Xuanhe Zhao. ✉e-mail: hyunwoo@mit.edu; aveves@bidmc.harvard.edu; zhaox@mit.edu

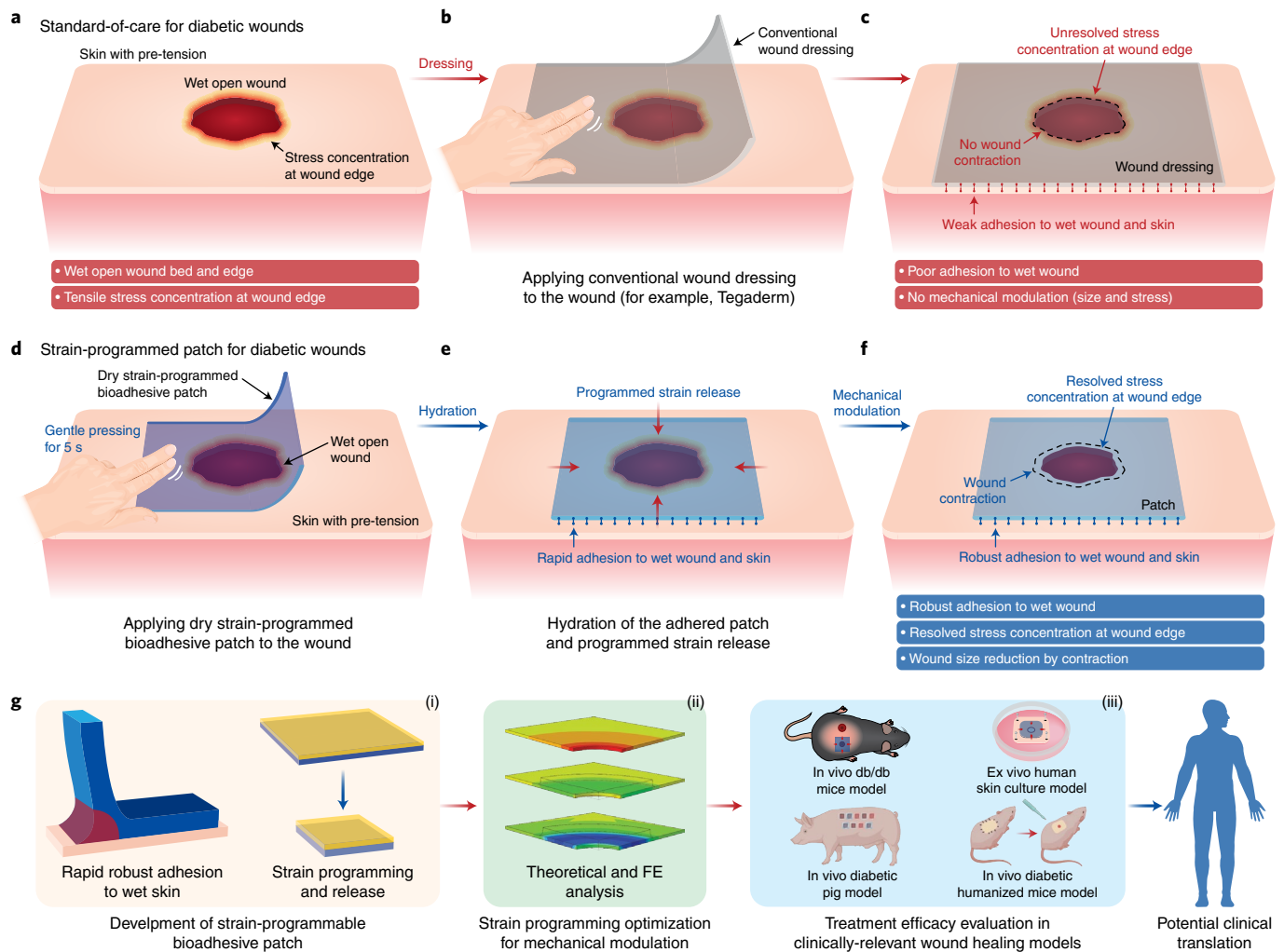


Fig. 1 | Strain-programmed patch for diabetic skin wounds. **a, b**, Schematic illustrations of the standard-of-care for diabetic skin wounds (**a**) by conventional wound dressings (**b**). **c**, Limitations of the conventional wound dressing-based treatment for the diabetic skin wound. **d, e**, Schematic illustrations for the treatment of diabetic skin wounds by application of the strain-programmed patch (**d**) and subsequent mechanical modulation of the diabetic skin wound (**e**). **f**, Advantages of the strain-programmed patch for diabetic wound healing. **g**, Schematic summary of the study consisting of (i) development of the strain-programmed bioadhesive patch, (ii) optimization of the strain-programmed patch for mechanical modulation of diabetic wounds and (iii) validation of the diabetic wound healing efficacy based on in vivo db/db mouse skin, ex vivo human skin culture, in vivo porcine skin and in vivo humanized mouse skin models. FE, finite element. Parts of **g**(iii) were created with BioRender.com.

contraction), respectively (Fig. 1f). The strain-programmed patch takes the form of a thin flexible dressing such as conventional wound dressings in the standard-of-care for diabetic skin wounds (for example, Tegaderm), offering potentially streamlined clinical translation within the existing treatment workflow. As summarized in Fig. 1g, we perform systematic characterization to establish strain programming, release capability and adhesion performance of the strain-programmed patch. We further develop theoretical and numerical models to rationally optimize the strain-programmed patch for mechanical modulation of diabetic mouse skin, porcine skin and human skin wounds. The diabetic wound healing efficacy of the strain-programmed patch is validated on the basis of in vivo diabetic mouse skin, ex vivo human skin culture, in vivo diabetic porcine skin and in vivo humanized diabetic mouse wound healing models.

Results

Design and mechanisms of the strain-programmed patch. The strain-programmed patch consists of two layers: (i) a non-adhesive

elastomer backing based on a hydrophilic polyurethane and (ii) a bioadhesive layer based on crosslinked networks of poly(acrylic acid) grafted with *N*-hydroxysuccinimide ester (PAA-NHS ester) and chitosan (Fig. 2a and Extended Data Fig. 1). The hydration-based shape-memory mechanism of the strain-programmed patch relies on a drastic change in the mechanical properties of the bioadhesive layer based on its hydration states^{25–27} (see Supplementary Discussion 1 for details on the hydration-based shape-memory mechanism). The hydrated bioadhesive in the rubbery state is soft (that is, Young's modulus ~40 kPa) and stretchable (that is, over 4 times the original length), whereas the dry bioadhesive becomes a glassy polymer with over 5 orders of magnitudes increase in stiffness (that is, Young's modulus ~5 GPa) (Supplementary Fig. 1). To programme the strain in the patch, an assembly of the hydrated bioadhesive layer bonded with the elastomer backing is pre-stretched along in-plane directions by the ratio of $\lambda_{\text{patch}}^{\text{pre}}$ (Fig. 2a and Supplementary Fig. 2). The pre-stretches on the assembly are maintained until the bioadhesive layer is dried to the glassy state. The glassy bioadhesive layer 'freezes' the applied pre-stretches in itself^{28–30} and constrains the

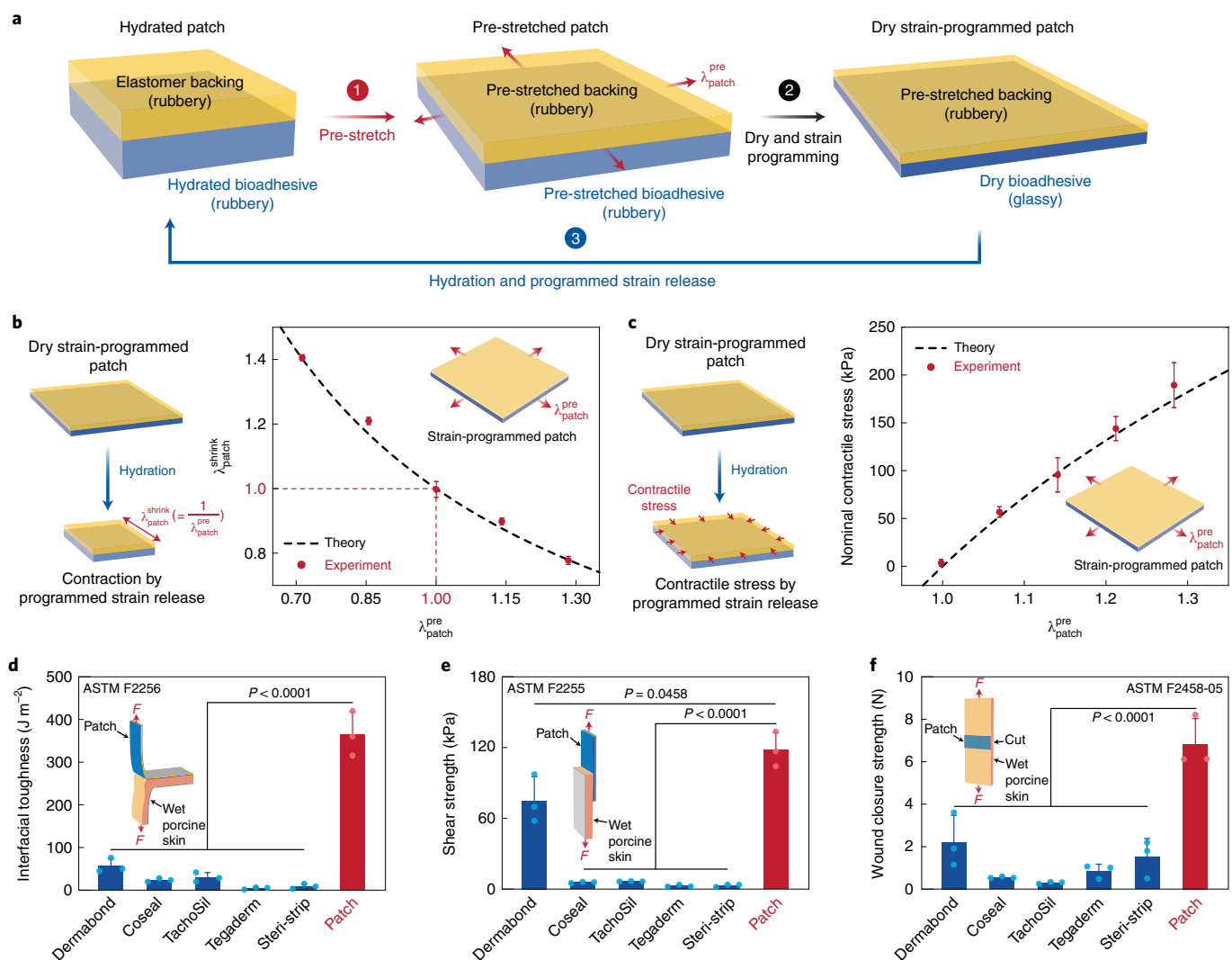


Fig. 2 | Design and mechanical properties of the strain-programmed patch. **a**, Strain programming and release of the bioadhesive patch by a hydration-based shape-memory mechanism. **b,c**, Theoretical and experimental values of contraction ($\lambda_{\text{patch}}^{\text{shrink}}$) (**b**) and nominal contractile stress (**c**) generated by programmed strain release upon hydration of the strain-programmed patch with varying $\lambda_{\text{patch}}^{\text{pre}}$. **d-f**, Interfacial toughness (measured by ASTM F2256) (**d**), shear strength (measured by ASTM F2255) (**e**) and wound closure strength (measured by ASTM F2458-05) (**f**) of the strain-programmed patch ($\lambda_{\text{patch}}^{\text{pre}} = 1.3$) and commercially available tissue adhesives on wet porcine skin. Values in **b-f** represent the mean \pm s.d. ($n = 4$ for **b,c**; $n = 3$ for **d-f**). Statistical significance and P values were determined by two-sided t -test for the comparison between two groups and by one-way ANOVA followed by Bonferroni's multiple comparison test for the comparison between multiple groups.

elastomer backing from releasing the pre-stretches due to the much higher rigidity of the glassy bioadhesive than the backing (Fig. 2a and Supplementary Figs. 2–4; see Supplementary Discussion 1 for details on the fabrication and strain-programming process).

Upon application of the strain-programmed patch on wet wounded tissues, the bioadhesive layer in the patch provides rapid robust adhesion to the tissue surface within 5 s by absorbing native physiological fluids and/or moisture from the wet wounded tissue and forming crosslinks via the dry-crosslinking mechanism^{24,27} (Extended Data Fig. 1; see Supplementary Discussion 2 for details on the dry-crosslinking mechanism). Meanwhile, as the bioadhesive layer becomes hydrated, it quickly returns to the soft rubbery state within 30 s, during which the strain-programmed patch releases the programmed strain along the in-plane directions and contracts by the ratio of $\lambda_{\text{patch}}^{\text{shrink}} = 1/\lambda_{\text{patch}}^{\text{pre}}$ (Fig. 2b and Supplementary Fig. 2). Furthermore, the release of programmed strain upon hydration of the strain-programmed patch can generate contractile mechanical

stress in a highly predictable manner (Fig. 2c; see Supplementary Discussion 3 for details on the theoretical analysis).

Rapid, robust and on-demand detachable adhesion. To evaluate the adhesion performance of the strain-programmed patch on wet wounded tissues, we conduct three standard mechanical tests for tissue adhesives to measure the interfacial toughness (by 180° peel test, ASTM F2256), shear strength (by lap-shear test, ASTM F2255) and wound closure strength (by ASTM F2392-05) on the basis of wet porcine skin as the model tissue^{22,24} (Fig. 2d–f). The strain-programmed patch (with $\lambda_{\text{patch}}^{\text{pre}} = 1.3$) can establish robust adhesion rapidly upon contact and gentle pressure (1 kPa) application for less than 5 s with high interfacial toughness of over 350 J m⁻² (Fig. 2d), shear strength of over 115 kPa (Fig. 2e) and wound closure strength of over 7 N (Fig. 2f) on wet tissues. Also, the strain-programmed patch maintains robust adhesion on wet tissues stably over days (Supplementary Fig. 5a). The adhesion

performance of the strain-programmed patch outperforms that of commercially available tissue adhesives and wound dressings, including cyanoacrylate adhesives (for example, Dermabond), polyethylene glycol-based adhesives (for example, Coseal), fibrin-based adhesives (for example, TachoSil), wound dressings (for example, Tegaderm) and wound bandages (for example, Steri-Strip) (Fig. 2d–f).

After adhering on tissues and releasing programmed strains, the swollen strain-programmed patch becomes a thin hydrogel layer with tissue-like softness (Young's modulus ~ 50 kPa), stretchability (over 3.5 times the original length) (Supplementary Fig. 1f) and high fracture toughness (over 400 J m^{-2}) (Supplementary Fig. 6). The robust interfacial integration between the non-adhesive elastomer backing and the bioadhesive layer in the swollen strain-programmed patch (interfacial toughness over 650 J m^{-2}) provides mechanical stability and integrity in wet physiological environments (Supplementary Fig. 7).

This synergistic combination of the dry-crosslinking mechanism for rapid robust wet adhesion and the hydration-based shape-memory mechanism for strain-programming enables facile and highly effective mechanical modulation of wet wounded tissues by the strain-programmed patch (Supplementary Video 1). Notably, the flexible strain programming capability of the strain-programmed patch allows its use for various types of wounds, such as incisional wounds (Extended Data Fig. 2 and Supplementary Video 2). Furthermore, taking advantage of the on-demand detachment capability of the bioadhesive layer³¹, the adhered strain-programmed patch can be atraumatically detached from the tissue on-demand by applying a biocompatible detachment solution to cleave physical and covalent crosslinks with the tissue surface (Extended Data Figs. 1c and 3, and Supplementary Video 3; see Supplementary Discussion 2 for details of on-demand detachment). Such benign on-demand removal of the strain-programmed patch can be potentially beneficial in the care of chronic diabetic wounds in clinical settings where frequent wound dressing changes are required^{32,33}.

Mechanical modulation of diabetic wounds. To provide quantitative guidelines for mechanical modulation of wounds by the strain-programmed patch, we utilize both analytical solutions (Supplementary Figs. 8 and 9) and finite-element method (Supplementary Fig. 10) to model the wound contraction and the remodelling of stresses in the skin around the wound by the strain-programmed patch (see Supplementary Discussion 3 for details on the analytical and finite-element modelling). Without loss of generality, we study a circular wound in the skin, which is a common form of diabetic wound. In our models, we consider a natively existing pre-strain and tension in the skin to better elucidate the mechanical modulation of wounds by the strain-programmed patch^{34–36}. Due to the native pre-strain and tension in the skin, the wound undergoes an initial enlargement in diameter (Supplementary Fig. 9b,d) and a substantial increase in hoop stress (over 2 times the native state) (Supplementary Fig. 9c,e), yielding a stress concentration around the wound edge which can impair wound closure and healing especially in diabetic wounds^{13–15} (Fig. 3b and Supplementary Fig. 11b).

From the above results, we hypothesize that the strain-programmed patch can potentially promote wound healing in diabetic wounds at different time frames. In acute or short-term period, the strain-programmed patch can promote diabetic wound healing by applying mechanical contraction and subsequently approximating the wound edges right after the application on wet wounded tissues (Fig. 3c, Supplementary Fig. 11c and Video 4). In chronic or long-term periods, the strain-programmed patch can promote diabetic wound healing by providing a favourable mechanical environment through the remodelling of the stress state around the wound, including reduction in the hoop stress

concentration (Fig. 3e and Supplementary Fig. 11e). Hence, the strain-programmed patch can be optimized by identifying the programmed strain ($\lambda_{\text{patch}}^{\text{pre}}$) that can provide wound contraction as well as removal of hoop stress concentration around the wound edge.

The theoretical and finite-element analyses show that the strain-programmed patch can mechanically modulate the wound in human skin and diabetic mouse skin by (i) reducing the wound diameter (Fig. 3b–d and Supplementary Fig. 11b–d) and (ii) reducing the hoop stress around the wound edge (Fig. 3e and Supplementary Fig. 11e) to various degrees on the basis of the relative size of the patch to the wound and the amount of programmed strain ($\lambda_{\text{patch}}^{\text{pre}}$). These results identify that the strain-programmed patch can effectively contract the wound and remove the hoop stress concentration around the wound edge at $\lambda_{\text{patch}}^{\text{pre}} = 1.3$ for the human skin (Fig. 3d,e) and $\lambda_{\text{patch}}^{\text{pre}} = 1.2$ for the diabetic mouse skin (Supplementary Fig. 11d,e). Furthermore, the strain-programmed patch can maintain the resultant mechanical modulation of wet wounds over days (Supplementary Fig. 5b). Notably, too large programmed strain may not be desirable due to potential discomfort to patients by generating excessive wound contraction (Fig. 3d and Supplementary Fig. 11d) or compressive stress around the wound (Fig. 3e and Supplementary Fig. 11e), and therefore, is not used in this study.

To further explore the applicability of the strain-programmed patch for clinically relevant diabetic wounds, we utilize two representative examples of DFU taken from patients at the Joslin-Beth Israel Deaconess Foot Center (Fig. 3g,j). We re-create the equivalent wounds on ex vivo porcine skin on the basis of the DFU images (Fig. 3h,k). Digital photography and finite-element results show that the strain-programmed patch can efficiently contract the wounds and resolve hoop stress concentration around the wounds (Fig. 3i,l). Moreover, the strain-programmed patch displays the same effectiveness in a particularly large re-created wound resembling another clinical case (Supplementary Fig. 12). Altogether, these results offer encouraging insights into the strain-programmed patch's applicability and potential translation in the clinic for treating diabetic wounds.

In vitro and in vivo biocompatibility. To evaluate biocompatibility of the strain-programmed patch and its on-demand detachment process, we perform an in vitro cell viability assay on the basis of mouse embryonic fibroblasts and an in vivo dorsal subcutaneous implantation on the basis of a rat model (Extended Data Fig. 4). The in vitro biocompatibility of the strain-programmed patch is comparable to that of the control media, showing no statistically significant difference in cell viability for mouse embryonic fibroblasts after 24 h culture (Extended Data Fig. 4a). The histological assessment made by a blinded pathologist indicates that the strain-programmed patch generates a mild to moderate inflammatory reaction, comparable to or lesser than that generated by US Food and Drug Administration (FDA)-approved commercially available tissue adhesives Coseal and Dermabond, respectively, after 2 weeks post-implantation (Extended Data Fig. 4b–d,g). Furthermore, the on-demand detachment process of the strain-programmed patch by the detachment solution generates a mild inflammatory reaction comparable to that generated by the sham control group (surgery without implantation) after 2 weeks post-surgery (Extended Data Fig. 4e–g).

Wound healing efficacy in an in vivo diabetic mouse model. To assess the efficiency of the strain-programmed patch in vivo, we employ an established model of impaired diabetic wound healing; the db/db mouse^{37,38}. Unlike wild-type rodents, these genetically diabetic mice with a leptin receptor gene mutation, heal mostly by re-epithelialization and less by contraction similar to human skin wound healing, which makes them well-suited for the study of delayed diabetic wound repair with implications for DFU patients³⁹

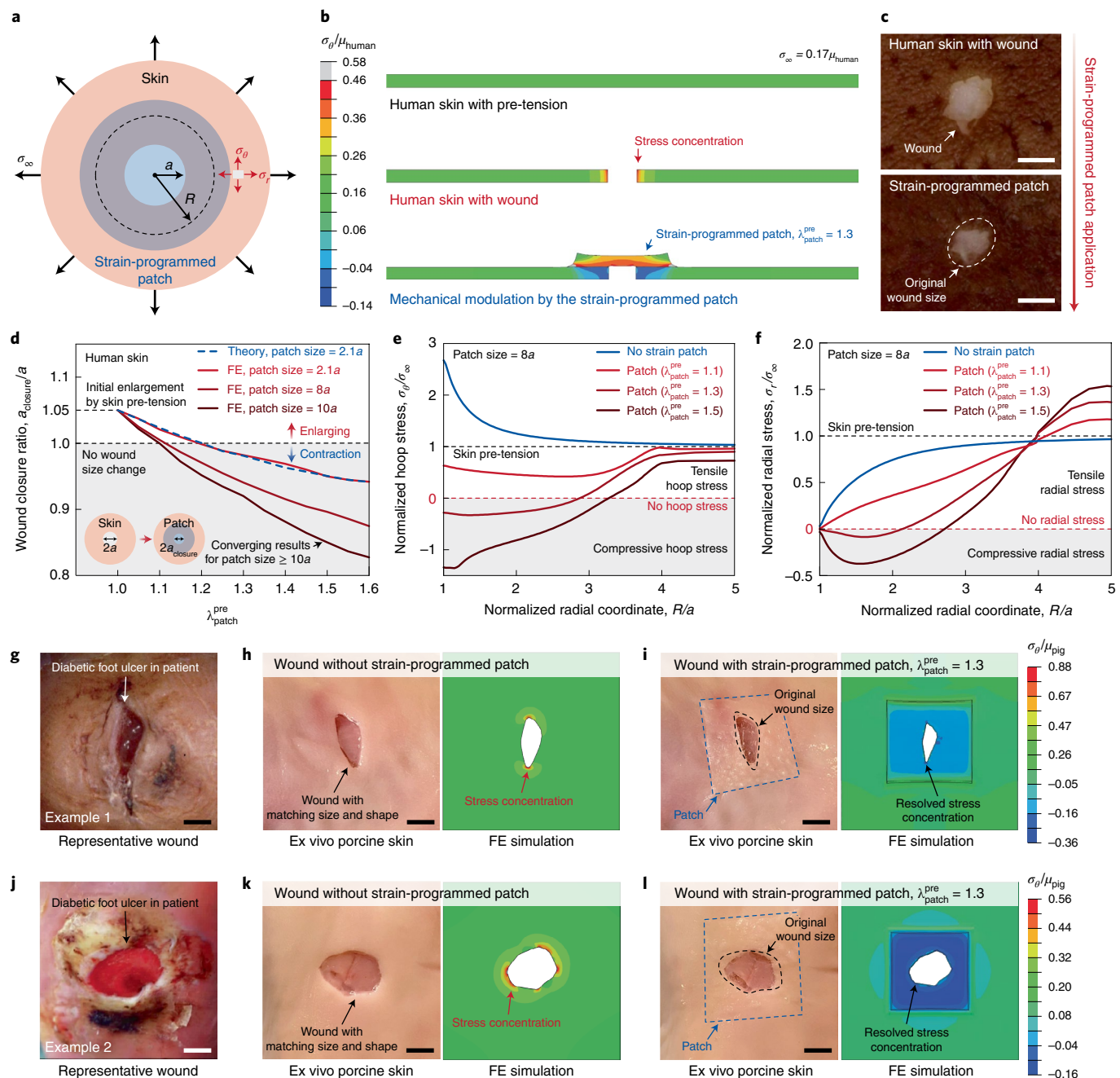


Fig. 3 | Mechanical modulation of human skin wounds. **a**, Schematic illustration of the theoretical and finite-element analyses. **b,c**, Representative finite-element results (**b**) and the corresponding experiment images of the ex vivo human skin (**c**) mechanically modulated by the strain-programmed patch ($\lambda_{\text{patch}}^{\text{pre}} = 1.3$; size = 4 times the wound diameter). The shear modulus of the human skin is denoted as μ_{human} , the hoop stress in the human skin as σ_{θ} and the residual stress in the intact human skin as σ_{∞} . **d**, Finite-element and experimental results for the wound closure ratio as a function of $\lambda_{\text{patch}}^{\text{pre}}$. **e,f**, Finite-element results for the hoop (σ_{θ} , **e**) and the radial (σ_r , **f**) stress around the wound for the strain-programmed patch with varying $\lambda_{\text{patch}}^{\text{pre}}$. **g,j**, Representative examples of DFU with varying shapes in patients. **h,k**, Ex vivo porcine skin wounds and finite-element results based on the DFU examples. **i,l**, Mechanical modulation of ex vivo porcine skin wounds and the corresponding finite-element results by the strain-programmed patch ($\lambda_{\text{patch}}^{\text{pre}} = 1.3$). Wound contraction and removal of wound-edge stress concentration are indicated in the experimental images and finite-element results. The shear modulus of the porcine skin is denoted as μ_{pig} and the hoop stress in the porcine skin as σ_{θ} . Scale bars, 5 mm (**c, g–l**).

(Supplementary Fig. 13). Application of the strain-programmed patch ($\lambda_{\text{patch}}^{\text{pre}} = 1.2$) onto 6 mm dorsal excisional wounds results in markedly improved wound closure at both 5 and 10 d post-injury (days 5 and 10), as evaluated by the percentage of open wound, degree of re-epithelialization and area of the migrating hyperproliferative neo-epidermis (Fig. 4) compared with the no strain patch

($\lambda_{\text{patch}}^{\text{pre}} = 1$) and Tegaderm (TD) conditions. The strain-programmed patch wounds on day 10 also display well-formed granulation tissue with thick collagen bundles and increased cellularity, which are indicative of advanced healing (Fig. 4d). In addition, the strain-programmed patch-treated wounds exhibit enhanced vascularization as evidenced by the higher density of CD31+ vessels

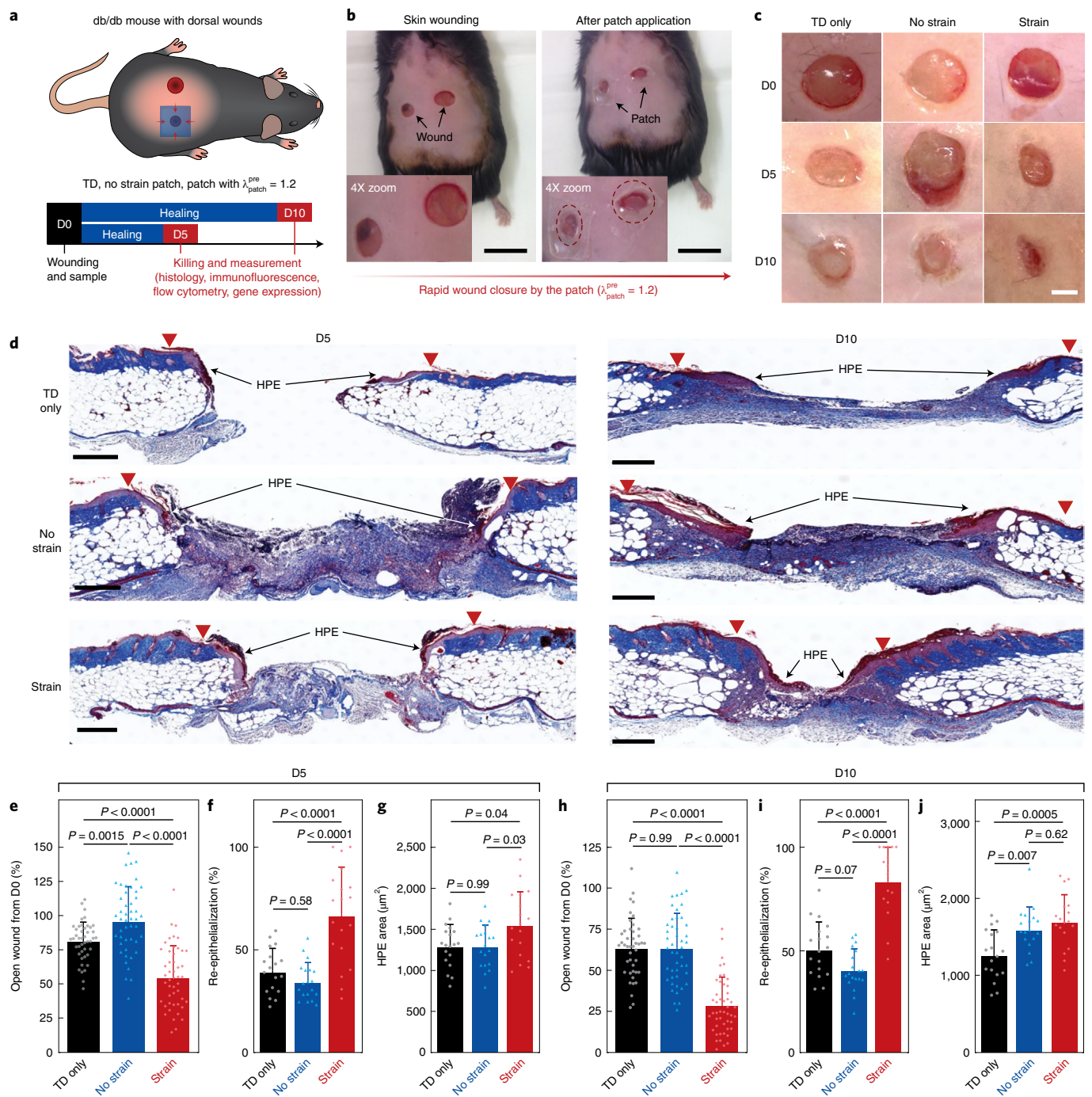


Fig. 4 | Evaluation of diabetic wound healing in a db/db mouse model. **a**, Schematic illustration of the study design. **b**, Representative images of db/db mouse dorsal wounds before (left) and after (right) the strain-programmed patch application. **c**, Representative macroscopic views of wounds on day 0 (D0), day 5 (D5) and day 10 (D10) for TD only, no strain ($\lambda_{\text{patch}}^{\text{pre}} = 1$) and strain-programmed ($\lambda_{\text{patch}}^{\text{pre}} = 1.2$) patch experimental groups. The adhered patches were removed before imaging and measurement. **d**, Representative images of wounds with MTS. Red triangles denote wound margins. HPE, hyperproliferative epidermis. **e–g**, Quantification of the wound closure expressed as % of open wound compared to D0 (**e**), the re-epithelialization expressed as %, with 100% being fully covered (**f**), and the HPE area (**g**) on D5. **h–j**, Quantification of the wound closure expressed as % of open wound compared to D0 (**h**), the re-epithelialization expressed as % (**i**), and the HPE area (**j**) on D10. Values in **e–j** represent the mean \pm s.d. ($n = 44$ for TD only, 47 for no strain and 48 for strain in **e**; $n = 18$ for TD only, 19 for no strain and 19 for strain in **f**; $n = 19$ for TD only, 19 for no strain and 18 for strain in **g**; $n = 44$ for TD only, 46 for no strain and 48 for strain in **h**; $n = 18$ for TD only, 19 for no strain and 16 for strain in **i**; $n = 18$ for TD only, 18 for no strain and 18 for strain in **j**; independent samples). Statistical significance and P values were determined by one-way ANOVA followed by Tukey's multiple comparison test. Scale bars, 20 mm (**b**); 3 mm (**c**); 500 μm (**d**, left); and 400 μm (**d**, right).

(Fig. 5a–d). There are also fewer active Caspase-3+ apoptotic cells in the wound bed of strain-programmed patch-treated mice on day 5 (Extended Data Fig. 5c) and more proliferating Ki67+ epi-

dermal cells on day 10 wounds (Extended Data Fig. 5e). Consistent with augmented blood vessel formation, ECM production and rapid keratinocyte migration, the gene expression levels of several

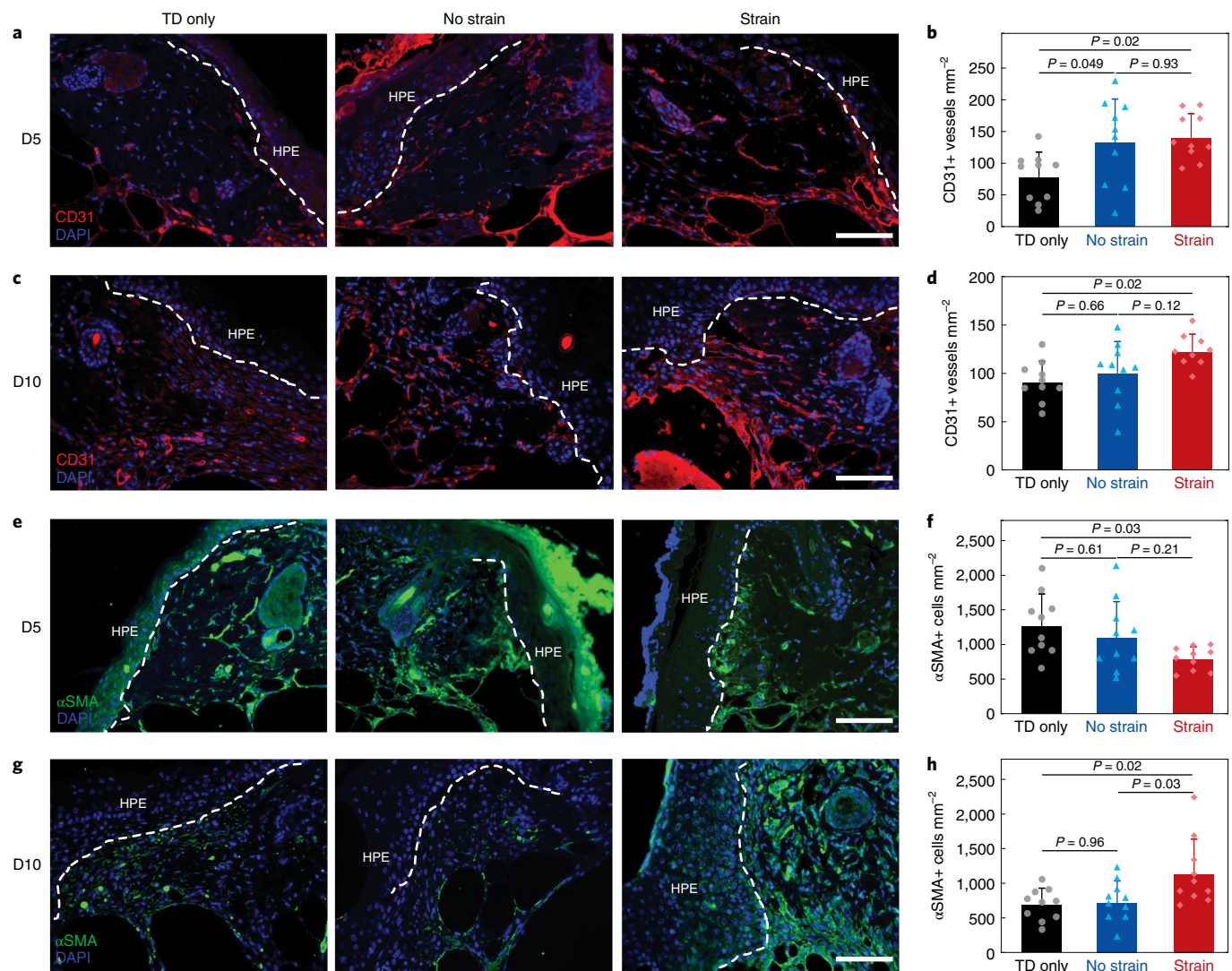


Fig. 5 | Immunofluorescence staining analysis of diabetic mouse wounds. **a,b**, Representative immunofluorescence images for CD31 (**a**) and quantification of CD31+ vessels per unit area (**b**) on D5. **c,d**, Representative immunofluorescence images for CD31 (**c**) and quantification of CD31+ vessels per unit area (**d**) on D10. **e,f**, Representative immunofluorescence images for αSMA (**e**) and quantification of αSMA+ cells per unit area (**f**) on D5. **g,h**, Representative immunofluorescence images for αSMA (**g**) and quantification of αSMA+ cells per unit area (**h**) on D10. In immunofluorescence images, blue fluorescence corresponds to cell nuclei stained with DAPI; red fluorescence corresponds to the expression on blood vessels (CD31); green fluorescence corresponds to the expression on fibroblast (αSMA); dashed line represents the epidermis border. Experimental groups are TD only, no strain ($\lambda_{\text{patch}}^{\text{pre}} = 1$) and strain-programmed ($\lambda_{\text{patch}}^{\text{pre}} = 1.2$) patch for both D5 and D10. Values in **b,d,f** and **h** represent the mean \pm s.d. ($n = 10$ for all experimental groups in **b,d,f** and **h**, except for strain in **h** where $n = 9$; independent samples). Statistical significance and P values were determined by one-way ANOVA followed by Tukey's multiple comparison test. Scale bars, 100 μm (**a,c,e** and **g**).

key pro-angiogenic and pro-healing growth factors are elevated in the strain-programmed patch-treated wounds, especially on day 5, including *Col3a1*, *Tgfb1*, *Vegfa*, *Fgf2* and *Hgf* (Supplementary Fig. 14a,b,d,e). db/db mice have a well-documented deficiency in wound contraction capability⁴⁰ with dysregulated fibroblast to myofibroblast conversion throughout the healing duration⁴¹, so we examine αSMA expression to determine whether modifying the wound stress levels via the strain-programmed patch application influences myofibroblast levels⁴². We find that the strain-programmed patch modifies the presence of αSMA+ cells in the wounds, with significantly reduced numbers on day 5, but increased numbers on day 10 (Fig. 5e–h). This is accompanied by diminished expression of *Engrailed-1* (*En1*) (Supplementary Fig. 14c,f), a transcription factor recently shown to define an important role in wound repair in a dermal fibroblast subpopulation responsible for fibrosis^{43–45}.

We hypothesize that initial strain-programmed patch application stress-shields the tissue and leads to decreased myofibroblasts, but as healing rapidly progresses, newly deposited granulation tissue alters the mechanical properties of the wound and activates more αSMA+ cells on day 10. Furthermore, adipocyte to myofibroblast differentiation⁴⁶ or the reverse⁴⁷ could also be implicated in the higher day 10 levels observed as previously reported.

We then characterize the wound inflammatory cell infiltrate with multicolour flow cytometry⁴⁸ to profile the major immune cell types affected by the patch application. Our gating strategy is illustrated on Supplementary Figs. 15 and 16. In contrast with the strain-programmed patch and TD groups, there are more total immune cells (CD45+) in the no strain patch-treated wounds on day 5 (Extended Data Fig. 6a), including more neutrophils (CD45+ CD64-Ly6G+) (Extended Data Fig. 6b) and monocytes

(CD45+ CD11b+ CD64-/intLy6C+) (Extended Data Fig. 6c), but fewer macrophages (CD45+ CD11b+ CD64+ F4/80+) (Extended Data Fig. 6d) and T cells (CD45+ CD3+) (Extended Data Fig. 6f). The strain-programmed patch also induces an amplified immune response but to a moderate extent compared with the no strain patch. This is to be expected, as any interaction of a biomaterial with the immune system triggers an immune response⁴⁹. We also analyse the expression of established macrophage polarization markers and discover that on day 5, the strain-programmed patch-treated groups display an M1-skewed phenotype, with increased % of CD80 and CD86 M1 macrophages (Extended Data Fig. 6i,j) and reduced % of CD163 and CD301b M2 macrophages (Extended Data Fig. 6k,m). Interestingly, they also show higher % of typically M2-associated CD206 cells (Extended Data Fig. 6l). On day 10, there are more immune cells and neutrophils in the strain-programmed patch and no strain patch-treated wounds (Extended Data Fig. 7a,b) and more monocytes and fewer macrophages in the no strain patch-treated wounds (Extended Data Fig. 7c,d). The sustained increased number of monocytes and reduced macrophages denote insufficient monocyte to macrophage differentiation and a prolonged inflammatory state. In addition, macrophages in the strain-programmed patch-treated wounds more frequently exhibit an M2-like phenotype with decreasing % of CD80 (Extended Data Fig. 7j) and increasing % of CD163 and CD301b (Extended Data Fig. 7k,m), suggesting that the healing process has transitioned towards the proliferation phase⁵⁰.

Next, to better understand the mechanisms of the observed wound healing acceleration, we perform bulk RNA-seq on day 10 wound tissues. Principal component analysis (PCA) shows separate clusters of the samples according to treatment, indicating distinct transcriptome profiles (Fig. 6a). Differential gene expression analysis with $\log(\text{fold change}) < 1$ or > 1 and false discovery rate (FDR) < 0.05 on the strain-programmed patch vs TD-treated wounds identifies 3,581 significantly modified genes (1,681 upregulated) (Fig. 6b) and 62 genes (14 upregulated) in the strain-programmed patch vs no strain patch-treated wounds (Fig. 6c). The volcano plots and heat maps (Fig. 6b,c and Supplementary Fig. 17) illustrate the most highly expressed features (complete lists are presented in Supplementary Data 1). Furthermore, over-representation analysis of the top differentially expressed genes highlights the enrichment of multiple processes linked to muscle contraction, which agrees with our observation of more $\alpha\text{SMA}+$ cells in the strain-programmed patch-treated wounds by day 10 (Fig. 6d–g). A similar analysis for the no strain patch vs TD-treated wounds yields cytokine-related pathways as most enriched (Supplementary Fig. 18).

To further characterize our transcriptomic data, we harness a publicly available dataset of single-cell RNA sequencing (scRNA-seq) mouse wounded tissue that bears similarities to our wounds⁵¹. In this work, three distinct myofibroblast subtypes are described using a model of large wounds regeneration: types I and II possibly derived from adipocyte precursors and type III associated with fibrotic response. CIBERSORTx annotation of cell abundances according to scRNA-seq cell cluster identity reveals minimal contribution of type III cells and an enrichment of type II myofibroblasts (Myf2) in the strain-programmed patch-treated wounds (Supplementary Fig. 19). Notably, two of the genes (*Tnfrsf6* and *Timp1*) in the list of top 10 significantly differentially expressed genes of this cluster are also overexpressed in the human healing-associated fibroblasts of our recent work¹⁹, possibly inferring common roles for these cell types. Other highly expressed genes have also been shown to positively influence cell functions such as migration^{52,53} (*Cd44*, *Aqp1*) and proliferation⁵⁴ (*Hist1h2ap*, *Cks2*, *Ube2c*, *Pclaf*, *Birc5*). Collectively, these findings indicate that applying the strain-programmed patch on diabetic murine cutaneous wounds promotes healing by positively affecting multiple integral reparative processes, including keratinocyte migration, angiogenesis and proliferation. It also

alleviates the tension of the tissue leading to an initially diminished and subsequently increased myofibroblast presence, with enrichment of a myofibroblast subpopulation which also proves beneficial for wound closure.

Wound healing efficacy in an ex vivo human skin culture model.

To examine the wound healing efficacy of the strain-programmed patch on human skin, we inflict 6 mm punch biopsy wounds on panniculectomy-derived discarded skin kept in cell culture conditions^{55,56} and monitor healing over 4 d (Fig. 7a,b). We quantify the distance between the two edges of the migrating epidermis as a measure of wound healing and find that the strain-programmed patch promotes faster re-epithelialization compared with the no strain patch and TD conditions (Fig. 7c,e). Masson's trichrome staining (MTS) for the assessment of collagen fibres and scoring by an experienced pathologist demonstrate elevated intensity in the strain-programmed patch-treated wounds, suggesting that the strain-programmed patch also influences the dermal ECM (Fig. 7d,f). We observe no differences in the number of fibroblast-like cells or vessels (Fig. 7g,h). Furthermore, the beneficial outcome in wound healing is also consistently prominent in an ex vivo human skin culture model with re-created native pre-tension (Extended Data Fig. 8f) where the skin is pre-strained to mimic the physiological pre-strain in human skin³⁵ (Extended Data Fig. 8a–e).

Wound healing efficacy in an in vivo diabetic porcine model.

To further verify the strain-programmed patch's efficacy, we select a porcine wound healing model that most closely mirrors the human wound healing process (Fig. 8). Porcine skin bears resemblance to that of humans, with similar dermal and epidermal architecture, substantial subcutaneous adipose depots, sparse hair follicle distribution, presence of structures such as rete ridges and most importantly, re-epithelialization-centric wound repair process⁵⁷. Diabetes is induced in Yucatan mini-pigs through Alloxan injection. After 20 weeks of diabetic state, an array of square full-thickness wounds (2.25 cm² wound area) is created on both sides of the dorsum (Fig. 8a). To optimize the strain-programmed patch for porcine skin wounds, we repeat analyses on the basis of the finite-element method similar to diabetic mouse and human skin wounds (Supplementary Fig. 20). We identify that the strain-programmed patch with $\lambda_{\text{patch}}^{\text{pre}} = 1.3$ can effectively provide wound contraction as well as removal of hoop stress concentration at the wound edge for porcine skin (Supplementary Fig. 20d,e). Furthermore, an additional finite-element analysis shows that the strain-programmed patch can favourably modulate skin wounds with diverse geometries including square wounds adopted in the porcine model (Supplementary Fig. 21).

After wounding, different treatments based on TD, no strain patch ($\lambda_{\text{patch}}^{\text{pre}} = 1$) and strain-programmed patch ($\lambda_{\text{patch}}^{\text{pre}} = 1.3$) are applied in an alternating manner to ensure no interference of the strain-programmed patch on adjacent wounds (Fig. 8b). The wounds are subsequently left undisturbed until study completion after 7 or 14 d. The strain-programmed patch-treated wounds show expedited wound closure at both examined time points (Fig. 8c–e,h). On day 7, the strain-programmed patch-treated wounds exhibit increased % re-epithelialization (Fig. 8f) and area of the migrating hyperproliferative neo-epidermis (Fig. 8g). By day 14, all wounds are almost fully re-epithelialized (Fig. 8d, right). However, only the strain-programmed patch treatment leads to thicker epidermis (Fig. 8i) with complete stratification and enhanced formation of numerous rete ridge structures (Fig. 8j), which are strong indications of the skin attaining its pre-injury form.

Immunostaining analysis for CD31 demonstrates elevated angiogenesis for the strain-programmed patch-treated wounds on day 7 (Extended Data Fig. 9a,b) and no differences on day 14 (Extended Data Fig. 9c,d). In addition, we find no $\alpha\text{SMA}+$ cells

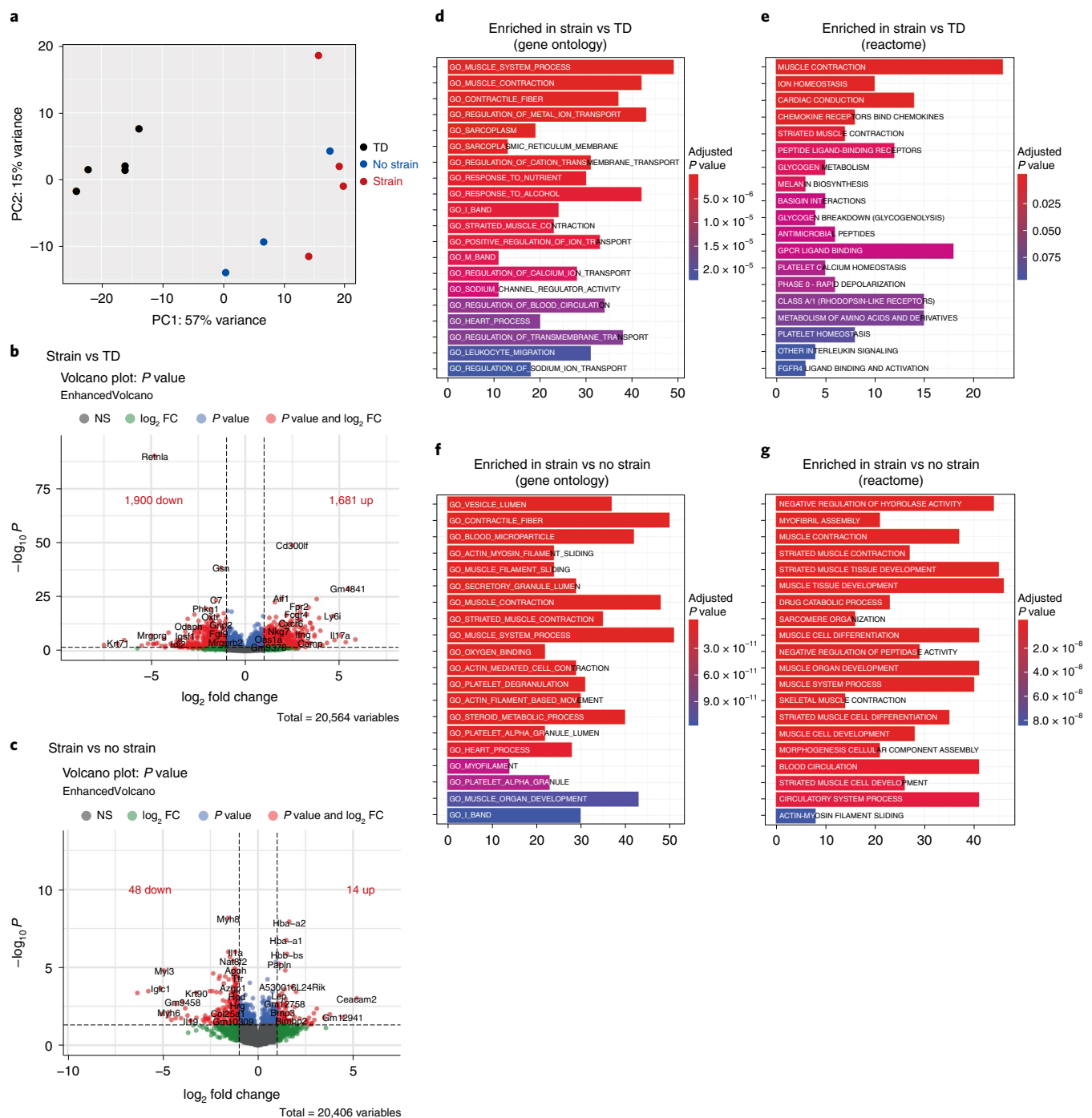


Fig. 6 | Transcriptomic analysis of diabetic mouse wounds. **a**, PCA plot illustrating the variances of the TD only (black dots, $n=5$), no strain ($\lambda_{\text{patch}}^{\text{pre}} = 1$) (blue dots, $n=3$) and strain-programmed ($\lambda_{\text{patch}}^{\text{pre}} = 1.2$) (red dots, $n=4$) patch datasets. **b,c**, Volcano plots displaying gene expression profiles when comparing the strain-programmed patch against TD (**b**) and the strain-programmed against no strain (**c**) patches. Red coloured data points represent genes that meet the thresholds of fold change (FC) above 1 or under -1 , $\text{FDR} < 0.05$. **d-g**, Functional over-representation analysis utilizing the top 500 differentially expressed genes results for strain vs TD and strain vs no strain in gene ontology (GO) (**d,f**) and reactome (**e,g**) databases. The x axis corresponds to the number of genes implicated in each pathway and the colour of the bars correlates with the adjusted P values as shown in the legends. The P values were determined by one-sided Fisher's exact test and adjusted by Storey's correction method.

on day 14 with only blood vessels staining positive for the marker (Extended Data Fig. 9g), while there is a decrease of αSMA^+ cells on day 7 (Extended Data Fig. 9e,f) similar to what we observe in db/db mouse earlier time point wounds (day 5). This suggests that the mesenchymal cell populations have adopted a non-myofibroblast-like phenotype by day 14. We further probe for selected markers with

quantitative PCR with reverse transcription (RT-qPCR) and identify that the strain-programmed patch-treated wounds on day 7 exhibit increased expression of important growth factors influencing angiogenesis (*VEGFA*) and keratinocyte migration and proliferation (*FGF2*, *EGF*) (Supplementary Fig. 22b). There is also higher expression of previously described regenerative markers *EGR1* and

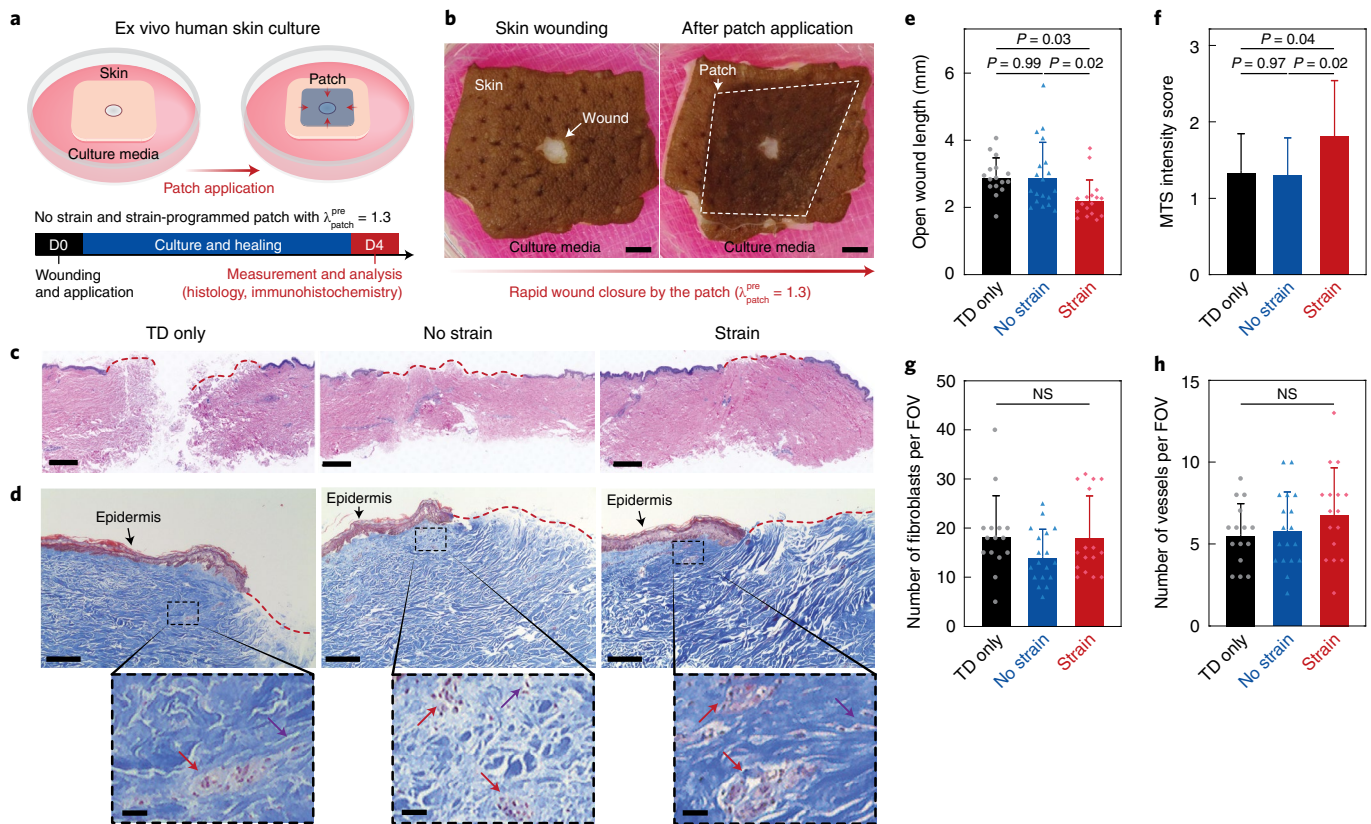


Fig. 7 | Evaluation of diabetic wound healing in a human skin model. **a**, Schematic illustration of the study design. **b**, Representative images of an ex vivo human skin culture setup before (left) and after (right) the strain-programmed patch application. **c,d**, Representative images from day 4 wounds for TD only, no strain ($\lambda_{\text{patch}}^{\text{pre}} = 1$) and strain-programmed ($\lambda_{\text{patch}}^{\text{pre}} = 1.3$) patch experimental groups with H&E (**c**) and MTS (**d**). Red dashed line marks the non-epithelialized tissue. Red arrows denote vessels and purple arrows denote fibroblast-like cells. **e–h**, Quantification of open wound length (**e**), MTS intensity score (**f**), number of fibroblast-like cells per field of view (FOV) (**g**) and number of vessels per FOV (**h**) on day 4. Values in **e–h** represent the mean \pm s.d. ($n = 16$ for TD only, 19 for no strain and 17 for strain in **e**; $n = 17$ for TD only, 16 for no strain and 18 for strain in **f**; $n = 15$ for TD only, 18 for no strain and 16 for strain in **g**; $n = 15$ for TD only, 18 for no strain and 16 for strain in **h**; skin derived from 3 individual patients' skin; independent samples). Statistical significance and P values were determined by one-way ANOVA followed by Tukey's multiple comparison test; NS, not significant. Scale bars, 5 mm (**b**); 800 μm (**c**); 200 μm (**d**, top); and 50 μm (**d**, bottom).

MFGE8 which characterize porcine and human fibroblast subtypes in environments with alleviated mechanical tension⁵⁸. Notably, the expression of *EN1* does not follow the pattern of the diabetic mouse wounds as it is not a conserved marker. The expression patterns are largely equalized across groups by day 14, with only *EGF* still remaining enriched in the strain-programmed patch treatment group. Cumulatively, our results indicate that a single application of the strain-programmed patch on sizable full-thickness diabetic porcine wounds is sufficient to promote wound closure by prompting re-epithelialization, amplified angiogenesis and a shift in fibroblast populations to a pro-regenerative phenotype.

Wound healing efficacy in an in vivo diabetic humanized mouse model. As an additional preclinical animal model with high translational relevance, we transplant human skin onto the backs of athymic nude mice for in vivo humanized mouse wound healing (Extended Data Fig. 10a). After 5 weeks of transplant engraftment period, we administer streptozotocin to induce diabetes^{59,60}. Following 7 weeks of confirmed hyperglycaemia, the human skin grafts are wounded with a 3 mm punch biopsy and either no strain patch ($\lambda_{\text{patch}}^{\text{pre}} = 1$) or strain-programmed patch ($\lambda_{\text{patch}}^{\text{pre}} = 1.3$, for human skin) is applied for 5 d. In line with other wound healing models discussed earlier, the strain-programmed patch-treated wounds exhibit acceleration in wound closure and re-epithelialization by day 5 (Extended

Data Fig. 10b–d). Higher counts of $\alpha\text{SMA}+$ cells are detected in the strain-programmed patch-treated wound edges, which can be attributable to the fact that the primary antibody used binds to both human and murine antigens, and mouse cells are responsible for the initial matrix deposition in this model⁶¹. Hence, their behaviour is akin to the db/db mouse wounds at the later time point where $\alpha\text{SMA}+$ cells appear more abundant. The gene expression of multiple human growth factors and regenerative markers, namely *VEGFA*, *FGF2*, *EGF*, *EGR1* and *MFGE8*, is also enriched for the strain-programmed patch treatment group, in agreement with the porcine wound healing model results (Supplementary Fig. 23).

Discussion

FDA has approved four products for DFU treatment and all of them were developed in the 1990s: becaplermin (rhPDGF-BB), a recombinant growth factor⁶; two bioengineered skin substitutes (Apligraf[®] and Dermagraft[®]); and Omnigraft that is based on Integra dermal regeneration matrix⁶². Not only is their cost considerable, but the efficacy of these products is rather limited, as in the pivotal trials, half or more of the participants failed to heal their wounds^{7,8}. Numerous other clinical trials with additional growth factors, including bFGF, EGF and VEGF, devices and other techniques have all failed to show meaningful efficacy⁶³. Furthermore, although basic research studies have indicated that Dipeptidyl-peptidase 4 (DPP4) inhibitors may

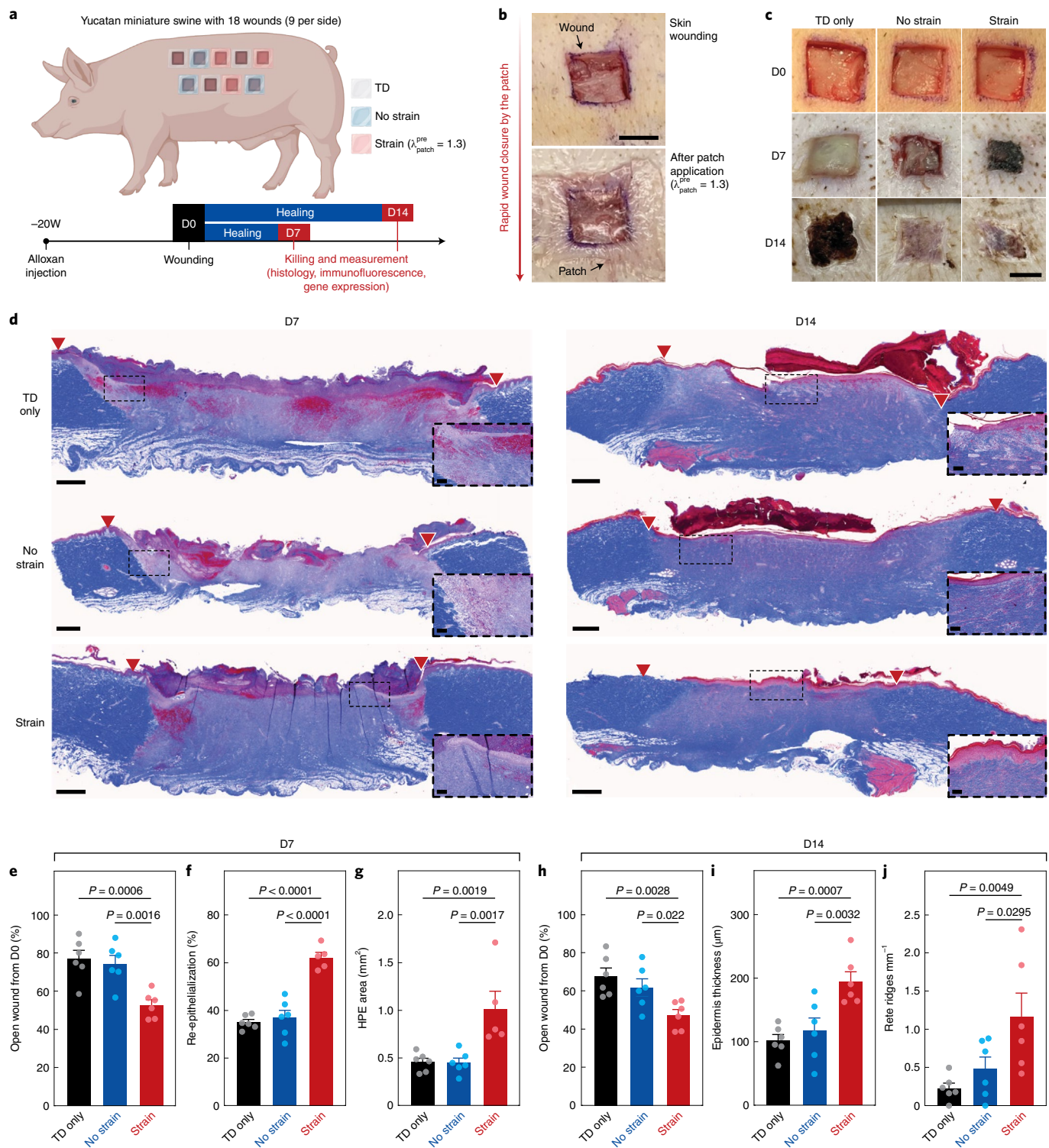


Fig. 8 | Accelerated diabetic wound healing in vivo porcine skin. **a**, Schematic illustration of the study design. **b**, Representative images of a porcine wound before (top) and after (bottom) the strain-programmed patch application. **c**, Representative macroscopic views of wounds on D0, D7 and D14 for TD only, no strain ($\lambda_{\text{patch}}^{\text{pre}} = 1$) and strain-programmed ($\lambda_{\text{patch}}^{\text{pre}} = 1.3$) patch experimental groups. The adhered patches were removed before imaging and measurement. **d**, Representative images from D7 (left) and D14 (right) wounds with MTS. Red triangles denote wound margins; inset images highlight areas of interest. **e–g**, Quantification of wound closure expressed as % of open wound compared to D0 (e), re-epithelialization expressed as % (f) and HPE area (g) on D7. **h–j**, Quantification of wound closure expressed as % of open wound compared to D0 (h), epidermal thickness (i) and number of rete ridges (j) on D14. Values in **e–j** represent the mean \pm s.d. ($n = 6$ for all experimental groups in **e, f, g, h, i** and **j**, except for strain in **f** and **g** where $n = 5$; independent samples). Statistical significance and P values were determined by one-way ANOVA followed by Fisher's least significant difference (LSD) post-hoc test. Scale bars, 10 mm (b); 10 mm (c); 1 mm (d); and 100 μm (d, inset). Parts of **a** were created with BioRender.com.

promote wound healing and reduce fibrosis⁴³, there is no concrete clinical evidence that these inhibitors can have any effect on DFU healing. This underscores the critical need to develop new therapies that could be tested in future clinical trials.

It has been well-established that mechanical reinforcement or stimuli to alleviate the adverse stress concentration around the wound can facilitate wound healing of healthy skin both in animal models and human clinical trials^{10,11,13,15,58}. However, any potential therapeutic effects of such mechanical stimuli are underexplored in chronic diabetic wounds such as DFU with impaired wound healing, including a reduced degree in contractility of wound edges and subsequent closure of wounds^{7,13,16–18}. We hypothesize that a tissue adhesive biomaterial capable of providing programmed mechanical contractions can facilitate the healing of diabetic wounds by addressing this mechanical imbalance. To implement this hypothesis into a viable therapeutic system, we developed a strain-programmed patch that synergistically incorporates the hydration-based shape-memory mechanism and the dry-crosslinking mechanism to achieve rapid, robust and controlled mechanical modulation of wet wounded tissue. We provide a quantitative design guideline for the predictable and rational optimization of the proposed strain-programmed patch on the basis of theoretical, numerical and experimental analysis and modelling. We further validate biocompatibility and diabetic wound healing efficacy of the strain-programmed patch via *in vitro* and *in vivo* rodent and porcine models. Taking advantage of these unique capabilities, we also demonstrate that the strain-programmed patch can be readily translated into human-scale diabetic wound healing applications on the basis of *ex vivo* human skin and humanized mouse skin wound healing models.

Our results show that application of the strain-programmed patch on db/db mouse wounds achieves a 50% wound closure and 70% re-epithelialization by day 5 post-injury and a remarkable 75% wound closure and 90% re-epithelialization on day 10. This outcome outperforms the previously reported interventions in similar models^{64–66}, including PDGF treatment⁶⁷ which is the only FDA-approved recombinant growth factor therapy for DFU⁶⁸. Our findings that modulation of wound tension ameliorates healing complement and expand on recent work⁴⁴ that used both a device to control wound mechanical forces and a pharmacological inhibition strategy to demonstrate that *Engrailed-1* expressing fibroblasts activated via mechanotransduction signalling are responsible for fibrosis in the wound and blocking them results in regeneration. Here we show that a similar approach is also highly effective in impaired diabetic wound healing.

Profiling the major immune cell types involved in murine wound healing, we discover that the strain-programmed patch elicits an inflammatory response comparable to the standard-of-care control (Tegaderm), which however does not prove detrimental to wound closure. Chronic diabetic wounds, such as DFU, are mainly characterized by the persistence of low-grade inflammation and inability to progress to the next phase of wound healing^{13,16–18}. Previous studies in our unit have shown that approaches that improve wound healing in diabetic murine models exert their beneficial effects by converting the low-grade chronic inflammation to an acute one and that this conversion is adequate to promote linear progression to the next phases and accelerate wound healing^{69,70}. Similar findings have also been reported by us and others in human studies^{71,72}.

Outlook

Our findings in diabetic swine and humanized mice wounds substantiate the efficiency of the strain-programmed patch in models of increased clinical relevance. A single application of the strain-programmed patch confers substantial benefits in several aspects of wound healing, and thus could be translated in clinical practice with minimized interference with the wound, compared

with necessary repeated dressing changes in similar approaches⁵⁸. Comparative transcriptomic analyses and gene expression studies confirm the heterogeneity of the wound microenvironment fibroblast populations and point to their importance as central orchestrators in diabetic wound repair processes. Taken together, our results indicate that the strain-programmed patch consistently improves re-epithelialization and appears to favour pro-regenerative fibroblasts across different models and species, signifying that it affects common mechanisms to guide diabetic tissue regrowth.

Overall, the diabetic wound healing data based on four different preclinical models support our hypothesis and suggest that the strain-programmed patch can offer a promising therapeutic solution for the treatment of chronic diabetic wounds. We envision that the strain-programmed patch has the potential for commercialization and eventual translation as a clinical treatment for chronic diabetic wounds. The patch could also be effective in other conditions of acute or chronic wounds, such as burn injuries, venous ulcers and pressure sores. However, additional steps would need to be taken for further investigation and potential clinical translation. Future investigations should focus on employing multi-omics methods to comprehensively map the different cell populations and signalling pathways influenced by the strain-programmed patch treatment^{19,73}. In addition, before the patch could be used in a clinical setting, further studies are required to define indications, frequency of application and suitable strain levels for different parts of the body and patient populations.

Methods

Materials. All chemicals were obtained from Sigma-Aldrich unless otherwise mentioned and used without further purification. For preparation of the strain-programmed patch, acrylic acid, α -ketoglutaric acid, poly(ethylene glycol methacrylate) (PEGDMA; Mn = 550), chitosan (Mw = 250–300 kDa with degree of deacetylation >90%; ChitoLytic), hydrophilic polyurethane (HydroMed D3, AdvanSource Biomaterials) and NHS ester functionalized monomer with disulfide bond were used. The NHS ester functionalized monomer with disulfide bond was synthesized following the previously reported protocol³¹. To prepare the detachment solution, sodium bicarbonate and reduced L-glutathione were used. All porcine skin tissues for *ex vivo* experiments were purchased from a research-grade porcine tissue vendor (Sierra Medical).

Preparation of the strain-programmed patch. The bioadhesive layer was prepared on the basis of the previously reported protocol^{34,31}. Acrylic acid (30% w/w), chitosan (2% w/w), α -ketoglutaric acid (0.2% w/w) and PEGDMA (0.03% w/w) were dissolved in deionized water. Then, 100 mg NHS ester functionalized monomer with disulfide bond was dissolved in 1 ml acetone and added to 10 ml of the above stock solution to get a precursor solution. The precursor solution was then poured on a glass mould with spacers (210 μ m thickness unless otherwise mentioned) and cured in an ultraviolet (UV) crosslinker (365 nm, 10 W power) for 30 min. As a non-adhesive elastomer backing resin, 10% w/w hydrophilic polyurethane in ethanol/water mixture (95:5 v/v) was spin-coated on the as-prepared bioadhesive at various speeds (Supplementary Fig. 24; 100 r.p.m. was used unless otherwise mentioned).

The as-prepared bioadhesive layer coated with the non-adhesive elastomer backing resin underwent multi-step processes to fabricate the strain-programmed patch (Supplementary Fig. 2). Detailed fabrication steps are described in Supplementary Discussion 1. The prepared dry strain-programmed patch was sealed in a plastic bag with desiccants and stored at room temperature before use. To prepare the detachment solution, 0.5 M sodium bicarbonate and reduced L-glutathione were dissolved in PBS.

In vivo diabetic mouse skin wound healing study. All procedures for *in vivo* diabetic mouse skin wound healing study were approved by the BIDMC Institutional Animal Care and Use Committee (IACUC). Male db/db mice (strain no. 000642) were obtained from Jackson Laboratories and acclimated to the animal facility for at least one week before surgery. They were routinely weighed and their blood glucose was assessed with a commercially available glucometer (Contour, Bayer) and confirmed to be >250 mg dl⁻¹. Mice were housed on a 12/12 light/dark cycle with constant temperature (22 °C) and humidity (50–60%). Regular chow and water were available *ad libitum*. Mice (12 weeks old) were anaesthetized using isoflurane and two circular biopsy-punched 6 mm (Integra Miltenex) full-thickness wounds were created on their depilated and disinfected dorsum. The strain-programmed patches ($\lambda_{\text{patch}}^{\text{pre}} = 1.2$), no strain patches ($\lambda_{\text{patch}}^{\text{pre}} = 1$) or no patches (25 mm wide and 25 mm long) were immediately placed on the

wounds. The wounds were then covered with an occlusive dressing (Tegaderm, 3M) for protection. The mice were housed individually after surgery and observed every day until euthanized with excess CO₂ on days 5 or 10. The wounds were photographed on days 0, 5 and 10 with a standard iPhone5 camera secured on a stand and measured with digital calipers (ThermoFisher, 14-648-17). A ruler was placed beside the wounds as a scale bar for area calculation. Wound closure was quantified using both ImageJ (version 2.1.0) and caliper measurements and expressed as percentage healed compared to day 0.

Ex vivo human skin culture wound healing study. Skin specimens were obtained from a commercial vendor (BioIVT) and were collected from the vendor's Institutional Review Board-approved abdominoplasty procedures of three female patients aged 28 to 41 years. De-identified samples were provided with removed subcutaneous adipose tissue in sterile PBS at 4 °C on the day of surgery and were immediately processed. Before wounding, skin specimens were sterilized by sequential washes with iodine, 70% ethanol and PBS, and were then cut into evenly sized squares to fit into a 60 mm tissue culture dish (ThermoFisher). A 6 mm biopsy punch was used to gently punch the skin's epidermis partially penetrating into the papillary dermis to create a wound. The strain-programmed patches ($\lambda_{\text{patch}}^{\text{pre}} = 1.3$), no strain patches ($\lambda_{\text{patch}}^{\text{pre}} = 1$) (25 mm wide and 25 mm long) or Tegaderm were applied onto the wounds. A sterile gauze was placed on top of the tissue culture dish and soaked with high-glucose DMEM (Gibco) supplemented with 10% heat-inactivated fetal bovine serum (FBS; Sigma-Aldrich) and 1% penicillin-streptomycin (P/S; Gibco). Skin specimens were next placed dermis side down onto the culturing dishes and incubated at 37 °C and 5% CO₂. Media were changed every day.

To re-create native pre-tension in the ex vivo human skin culture wound healing model, split-thickness skin samples from abdominoplasties of two female patients aged 28 and 47 years were used (obtained from BioIVT). UV-sterilized dental wax (Polysciences) was cut in octagonal pieces and stacked in three layers inside a 100 mm tissue culture dish to serve as a substrate. Evenly cut squares of human skin samples were pre-strained and fixed at the corners with autoclaved 25 mm stainless steel pins on top of media-soaked sterile gauze on the basis of the pre-calculated locations for pins (3.5–5% tensile pre-strain). Skin wounds were created, and the strain-programmed patches ($\lambda_{\text{patch}}^{\text{pre}} = 1.3$) and no strain patches ($\lambda_{\text{patch}}^{\text{pre}} = 1$) (25 mm wide and 25 mm long) were applied and monitored as outlined above.

In vivo diabetic porcine skin wound healing study. All procedures were approved by the BIDMC IACUC. Two neutered Yucatan miniature swine of either sex were obtained from Sinclair Bio Resources. Diabetes was induced by Sinclair with intravenous administration of alloxan monohydrate (100 mg kg⁻¹) at 5 months of age and sustained for approximately 5 months before wounding, with fasting blood glucose maintained with daily insulin glargine (Lantus) injections at levels between 300 and 500 mg dl⁻¹. Before surgery, an acrylic board template was fabricated to replicate the desired wound distribution. Each square was identical at 1.5 × 1.5 cm, with 2.5 cm intra-square spacing. The template was then sterilized by autoclaving. General anaesthesia was administered by the BIDMC Animal Research Facility veterinary staff and established with intramuscular injection of 10 mg kg⁻¹ telazol. Animals were intubated with an endotracheal tube and maintained on 1.5–3% of inhaled isoflurane for the duration of the surgery. Once the animal was fully anaesthetized, it was placed on its side and the dorsum was cleaned with 70% alcohol and Povidone-iodine. A sterile fenestrated drape was placed over the entire animal with dorsum exposure only. The acrylic template was positioned horizontally, 5 cm from the spine, between the scapula and iliac crest. Markings of each individual square were then made with a sterile surgical marker and using a No. 11 blade scalpel, each dermal full-thickness (approximately 0.6 cm deep) wound was created, removing the skin by careful dissection with skin forceps and double-blade cutting scissors. The procedure was repeated until all 9 wounds were completed. Each individual wound's photo was taken and exact size was measured with a surgical ruler and recorded. The strain-programmed patches ($\lambda_{\text{patch}}^{\text{pre}} = 1.3$), no strain patches ($\lambda_{\text{patch}}^{\text{pre}} = 1$) (3.5 cm wide and 3.5 cm long) or no patches were applied onto the wounds and then covered with Tegaderm. To further protect the dermal wounds, a cotton dressing was applied to cover and completely shield the wounded area, securing it with elastic tape (Elastoplast) at the edges. The animal was then rotated to its opposite side and prepared the same way to create the additional 9 dermal wounds. Once all 18 dermal wounds were completed and treatments applied, a custom-made fenestrated jacket (Lomir Biomedical) was fitted into the animal at the end of the surgical procedure before waking up. Analgesics Buprenorphine and Fentanyl patch were administered according to US Department of Agriculture guidelines. The wounds were photographed and re-measured on the days of euthanasia.

In vivo diabetic humanized nude mice wound healing study. All procedures were approved by the BIDMC IACUC. To generate a humanized skin graft mouse model, 6-week-old nude male mice (homozygous *Foxn1*tm, Jackson strain no. 002019) were used as the recipient animals. These mice are devoid of T cells and suffer from a lack of cell-mediated immunity, making them a model of choice for xenograft studies. Mice were housed on a 12/12 light/dark cycle

with constant temperature (22 °C) and humidity (50–60%). Regular chow and water were available ad libitum. Mice dorsal skin of an approximate 2 cm × 3 cm area was excised and a graft of human skin was sutured onto the gap. Human skin was obtained from the commercial vendor's (BioIVT) Institutional Review Board-approved abdominoplasty procedure of a 54-year-old female patient. Grafted mice were left to heal and accommodate the new tissue for 5 weeks. Diabetes was induced 5 weeks post-grafting via 5 consecutive intraperitoneal injections with 50 mg kg⁻¹ streptozotocin and an extra single dose of 180 mg kg⁻¹ in case the animal did not turn diabetic. Diabetes was confirmed with blood glucose measurements greater than 250 mg dl⁻¹. Mice sustained a hyperglycaemic state for 7 weeks before wounding experiments. Wounds were inflicted on the transplanted human skin with a 3 mm punch biopsy and monitored for healing for 5 d. The strain-programmed patches ($\lambda_{\text{patch}}^{\text{pre}} = 1.3$) or no strain patches ($\lambda_{\text{patch}}^{\text{pre}} = 1$) (15 mm diameter) were applied onto the wounds immediately after injury and then covered with Tegaderm.

Histology, immunohistochemistry and immunofluorescence. Mouse, human or porcine wound tissues following completion of the study on days 5 and 10 (mouse), 4 (human) and 7 and 14 (porcine) were bisected at the wound centre. One-half was immediately snap-frozen and stored at –80 °C, or immediately placed in RNAlater solution (ThermoFisher), while the other was fixed in 10 % formalin and processed for paraffin embedding. Sections of 5 µm thickness were used. MTS and hematoxylin and eosin (H&E) staining were performed at BIDMC Histology Core. Whole-slide image acquisition was performed at the DF/HCC Research Pathology Cores with an Aperio CS2 scanner (Leica Biosystems) or at iHisto with a Motic EasyScan Infinity slide scanner. Re-epithelialization was quantified from H&E and MTS images by measuring the length of the migrating epithelial tongue covering the wound and dividing by the entire length of the wound. An experienced dermatopathologist (A.K.) scored the human wound MTS slides according to intensity on a scale of 1 to 3 and counted the number of fibroblast-like cells and blood vessels from acquired images (×4 magnification) including the entire wound margin. For immunohistochemistry, tissue sections were de-paraffinized, rehydrated and antigen-retrieved with citrate buffer pH 6.0 in a pressure cooker for 15 min. They were then blocked in 1% BSA for 1.5 h at r.t. The Vectastain Elite ABC rabbit IgG kit (Vector Laboratories) was used following the manufacturer's instructions. Sections were incubated with rabbit anti-active caspase-3 (1:40, BD, 559565) for mouse wound sections or rabbit anti-CD31 (1:50, Abcam ab28364) for pig wound sections overnight at 4 °C. Visualization of the secondary biotinylated antibody binding was performed using NovaRED substrate kit (Vector Laboratories). Images of sections were obtained at ×4 or ×10 magnification with Eclipse E200 upright microscope (Nikon) using Motic Images Plus 3.0 software.

For immunofluorescence staining, de-paraffinization and antigen retrieval of the paraffin-embedded mice or pig wound sections were performed as previously described. The primary antibodies used were: mouse monoclonal anti-cytokeratin 14 (1:1,000, Abcam ab7800), rat monoclonal anti-Ki67 (1:200, eBioscience, 14-5698-82), rabbit polyclonal anti-CD31 (1:50, Abcam ab28364) and goat polyclonal anti-alpha smooth muscle actin (1:1,000, Abcam ab21027). Sections were first blocked (5% donkey serum, 1% BSA in 0.1% Triton-X PBS) for 1 h at r.t. and then incubated with primary antibodies overnight at 4 °C in a humidified chamber. The secondary antibodies used were all donkey at 1:500 dilution: anti-mouse IgG H&L (Alexa Fluor 488, ab150109); anti-rat IgG H&L (Alexa Fluor 647, ab150155); anti-rabbit IgG H&L (Alexa Fluor 594, ab150064); anti-goat IgG H&L (Alexa Fluor 488, ab150133); anti-rabbit IgG H&L (Alexa Fluor 594, ab150064); and anti-goat IgG H&L (Alexa Fluor 647, ab150131). Nuclear counterstaining was performed with 4',6-diamidino-2-phenylindole (DAPI) (Invitrogen). Sections were quenched for 5 min using the TrueView autofluorescence quenching kit to decrease background (Vector Laboratories) and covered with VECTASHIELD anti-fade mounting medium (Vector Laboratories). Images were obtained at ×10 and ×20 magnification with an Axio Imager A2 microscope using Zen Blue edition software (Zeiss). Quantification was performed on ImageJ (version 2.1.0) by counting the positive cells/structures for a particular marker and dividing by the area of the tissue for normalization.

Skin dissociation and flow cytometry. Immediately following euthanasia, mouse skin composed of wound and approximately 0.5 mm of peri-wound tissue was excised and kept on ice-cold sterile PBS until processing within 2 h. Four wounds from two mice were pooled as one sample to ensure enough single cells. The skin was finely minced with a scalpel and placed for 30 min at 37 °C on a shaker in a digesting enzyme cocktail of 2 mg ml⁻¹ Collagenase P (Roche), 2 mg ml⁻¹ Dispase (Gibco) and 1 mg ml⁻¹ DNase I (Stemcell Technologies) in DMEM (Gibco) with 10% FBS and 1% P/S, using glass pipettes to break down the extracellular matrix every 10 min. Single-cell suspensions were passed through a 40 µm cell strainer, counted with a K2 cellometer (Nexcelom Bioscience) and cryopreserved in 90% FBS and 10% dimethylsulfoxide until processing.

Cells were quickly thawed and adjusted to a concentration of 10⁶ cells per ml. A LIVE/DEAD fixable dead cell stain kit was used to exclude dead cells from the analysis (ThermoFisher). AbC total antibody and amine reactive ArC compensation bead kits (ThermoFisher, A10497 and A10346) were included for single stain controls. After completing viability staining following the

manufacturer's instructions, cells were blocked (Biolegend FACS buffer with 0.05% anti-mouse CD16/32, Biolegend 101320 and 0.05% Tru-stain monoclonal blocker, Biolegend 426103) for 10 min at r.t. An antibody cocktail with details listed on Supplementary Dataset 2 was then added for 25 min on ice. Cells were washed 2 times, fixed with 0.4% PFA and stored at 4 °C protected from light until analysis the next day. The samples were run on a CytoFLEX LX flow cytometer (Beckman Coulter) and data were processed and analysed with CytExpert software (Beckman Coulter) at the BIDMC Flow Cytometry Core.

RNA extraction, sequencing and analysis. RNA extraction, library preparations and sequencing reactions were conducted at GENEWIZ. Total RNA was extracted using the Qiagen RNeasy Plus Universal mini kit following the manufacturer's instructions (Qiagen). Extracted RNA samples were quantified using Qubit 2.0 fluorometer (Life Technologies) and RNA integrity was checked on Agilent TapeStation 4200 (Agilent Technologies). RNA sequencing libraries were prepared using the NEBNext Ultra RNA library prep kit for Illumina following the manufacturer's instructions (NEB). Briefly, messenger RNAs were first enriched with Oligo(dT) beads. Enriched mRNAs were fragmented for 15 min at 94 °C. First strand and second strand complementary DNAs were subsequently synthesized. cDNA fragments were end-repaired and adenylated at 3' ends, and universal adapters were ligated to cDNA fragments, followed by index addition and library enrichment by limited-cycle PCR. The sequencing libraries were validated on the Agilent TapeStation (Agilent Technologies) and quantified using Qubit 2.0 fluorometer (Invitrogen) as well as by quantitative PCR (KAPA Biosystems). The sequencing libraries were clustered on one lane of a flow cell. After clustering, the flow cell was loaded on the Illumina HiSeq 4000 instrument and the samples were sequenced using a 2 × 150 bp paired-end configuration. Image analysis and base calling were conducted by the HiSeq Control software. Raw sequence data (.bcl files) generated from Illumina HiSeq were converted into fastq files and de-multiplexed using Illumina's bcl2fastq 2.17 software. One mismatch was allowed for index sequence identification.

Read quality was evaluated using FastQC and data were pre-processed with Cutadapt⁷⁴ for adapter removal following best practices⁷⁵. Gene expression against the GRCh38 transcriptome (Ensembl version 93)⁷⁶ was quantified with STAR⁷⁷ and featureCounts⁷⁸. Differential gene expression analysis was performed using DESeq2⁷⁹, while ClusterProfiler⁸⁰ was utilized for functional enrichment investigations. Genes with $\log_2[\text{fold change}] \geq 1$ and $\text{FDR} \leq 0.05$ were considered statistically significant. CIBERSORTx⁸¹ was used for abundance estimation of cell types accounting for at least 1% of cells in the scRNA-seq dataset in our bulk RNA-seq data. Gene set enrichment analysis⁸² was used to assess differences in gene signatures enrichment between groups.

RT-qPCR. The miScript II RT kit or RT2 first strand kit (Qiagen) was used according to the manufacturer's protocol for cDNA synthesis from 1 µg of RNA. For each PCR reaction, 30–45 ng cDNA was used. QuantiTect or RT2 primers were all purchased from Qiagen: *B2m* (QT01149547), *Col1a1* (QT00162204), *Col3a1* (QT01055516), *Egf* (QT00151018), *En1* (QT00248248), *Fgf2* (QT00128135), *Fgf7* (QT00172004), *Fn1* (QT00135758), *Hgf* (QT00158046), *Tgfb1* (QT00145250) and *Vegfa* (QT00160769) for mouse samples. *GAPDH* (QT00079247 or PPH00150F), *FGF7* (QT00101850), *VEGFA* (QT001010184), *TGFB1* (QT00000728), *COL1A1* (PPH01299F), *COL3A1* (PPH00439F), *EGF* (PPH00137B), *EGR1* (PPH00139A), *FGF2* (PPH00257C), *FN1* (PPH00143B) and *MFG8* (PPH07218A) for human samples. *ACTB* (PPS71698A), *COL1A1* (PPS72004A), *COL3A1* (PPS02256A), *EGF* (PPS00423A), *EGR1* (PPS19407A), *EN1* (PPS11650A), *FGF2* (PPS00943A), *FGF7* (PPS00608A), *FN1* (PPS00923A), *MFG8* (PPS00853A), *RPL4* (PPS07992A), *TGFB1* (PPS00418A) and *VEGFA* (PPS00495A) for pig samples. RT-qPCR was run with QuantiTect SYBR Green PCR kit or RT² SYBR Green qPCR Mastermix (Qiagen) on a Stratagene Mx3005P with MxPro qPCR software (Agilent Technologies). The cycling conditions used were according to the respective kit protocol (Qiagen). Quantification was performed using the 2^{-ΔΔC_T} method. Gene expression was normalized against the housekeeping gene *B2m* for mouse samples, *GAPDH* for human samples and *ACTB* / *RPL4* for pig samples.

Statistical analysis. GraphPad Prism (version 7.04) was used to assess the statistical significance of all comparison studies in this work. Data distribution was assumed to be normal for all parametric tests, but not formally tested. In the statistical analysis for comparison between multiple data groups, one-way analysis of variance (ANOVA) followed by Bonferroni's, Tukey's or Fisher's multiple comparison tests were conducted with thresholds of $*P < 0.05$, $**P \leq 0.01$ and $***P \leq 0.001$. In the statistical analysis for comparison between two data groups, two-sided *t*-test was used with thresholds of $*P < 0.05$, $**P \leq 0.01$ and $***P \leq 0.001$.

Reporting summary. Further information on research design is available in the Nature Research Reporting Summary linked to this article.

Data availability

The main data supporting the results in this study are available within the paper and its Supplementary Information. The RNA-seq data are available from the Gene Expression Omnibus (GEO) database, with accession number [GSE154132](https://www.ncbi.nlm.nih.gov/geo/query/acc.cgi?acc=GSE154132).

Publicly available single-cell RNA-seq data were obtained from GEO (accession number, [GSE141814](https://www.ncbi.nlm.nih.gov/geo/query/acc.cgi?acc=GSE141814)). Additional raw datasets generated during the study are too large to be publicly shared, yet they are available from the corresponding authors on reasonable request.

Received: 24 December 2021; Accepted: 27 May 2022;

Published online: 04 July 2022

References

1. *National Diabetes Statistics Report* (Centers for Disease Control and Prevention, 2017).
2. Geiss, L. S. et al. Resurgence of diabetes-related nontraumatic lower extremity amputation in the young and middle-aged adult U.S. population. *Diabetes Care* **42**, 50–54 (2019).
3. Boulton, A. J., Vileikyte, L., Ragnarson-Tennvall, G. & Apelqvist, J. The global burden of diabetic foot disease. *Lancet* **366**, 1719–1724 (2005).
4. Veves, A., Falanga, V., Armstrong, D. G., Sabolinski, M. L. & Apligraf Diabetic Foot Ulcer Study Graftskin, a human skin equivalent, is effective in the management of noninfected neuropathic diabetic foot ulcers: a prospective randomized multicenter clinical trial. *Diabetes Care* **24**, 290–295 (2001).
5. Marston, W. A., Hanft, J., Norwood, P. & Pollak, R. The efficacy and safety of Dermagraft in improving the healing of chronic diabetic foot ulcers: results of a prospective randomized trial. *Diabetes Care* **26**, 1701–1705 (2003).
6. Wieman, T. J., Smiell, J. M. & Su, Y. Efficacy and safety of a topical gel formulation of recombinant human platelet-derived growth factor-BB (becaplermin) in patients with chronic neuropathic diabetic ulcers. A phase III randomized placebo-controlled double-blind study. *Diabetes Care* **21**, 822–827 (1998).
7. Tecilazich, F., Dinh, T. & Veves, A. Treating diabetic ulcers. *Expert Opin. Pharmacother.* **12**, 593–606 (2011).
8. Tecilazich, F., Dinh, T. L. & Veves, A. Emerging drugs for the treatment of diabetic ulcers. *Expert Opin. Emerg. Drugs* **18**, 207–217 (2013).
9. Singer, A. J. & Clark, R. A. Cutaneous wound healing. *N. Engl. J. Med.* **341**, 738–746 (1999).
10. George Broughton, I., Janis, J. E. & Attinger, C. E. The basic science of wound healing. *Plast. Reconstr. Surg.* **117**, 12S–34S (2006).
11. Gurtner, G. C., Werner, S., Barrandon, Y. & Longaker, M. T. Wound repair and regeneration. *Nature* **453**, 314–321 (2008).
12. Wong, V. W. et al. A mechanomodulatory device to minimize incisional scar formation. *Adv. Wound Care* **2**, 185–194 (2013).
13. Eming, S. A., Martin, P. & Tomic-Canic, M. Wound repair and regeneration: mechanisms, signaling, and translation. *Sci. Transl. Med.* **6**, 265sr266 (2014).
14. Barnes, L. A. et al. Mechanical forces in cutaneous wound healing: emerging therapies to minimize scar formation. *Adv. Wound Care* **7**, 47–56 (2018).
15. Harn, H. I. C. et al. The tension biology of wound healing. *Exp. Dermatol.* **28**, 464–471 (2019).
16. Falanga, V. Wound healing and its impairment in the diabetic foot. *Lancet* **366**, 1736–1743 (2005).
17. Loots, M. A. et al. Differences in cellular infiltrate and extracellular matrix of chronic diabetic and venous ulcers versus acute wounds. *J. Invest. Dermatol.* **111**, 850–857 (1998).
18. Brem, H. & Tomic-Canic, M. Cellular and molecular basis of wound healing in diabetes. *J. Clin. Invest.* **117**, 1219–1222 (2007).
19. Theodoridis, G. et al. Single cell transcriptomic landscape of diabetic foot ulcers. *Nat. Commun.* **13**, 181 (2022).
20. Wang, J. H.-C., Thampatty, B. P., Lin, J.-S. & Im, H.-J. Mechanoregulation of gene expression in fibroblasts. *Gene* **391**, 1–15 (2007).
21. Gurtner, G. C. et al. Improving cutaneous scar formation by controlling the mechanical environment: large animal and phase I studies. *Ann. Surg.* **254**, 217–225 (2011).
22. Li, J. et al. Tough adhesives for diverse wet surfaces. *Science* **357**, 378–381 (2017).
23. Blacklow, S. et al. Bioinspired mechanically active adhesive dressings to accelerate wound closure. *Sci. Adv.* **5**, eaaw3963 (2019).
24. Yuk, H. et al. Dry double-sided tape for adhesion of wet tissues and devices. *Nature* **575**, 169–174 (2019).
25. Kelley, F. N. & Bueche, F. Viscosity and glass temperature relations for polymer-diluent systems. *J. Polym. Sci.* **50**, 549–556 (1961).
26. Frisch, H., Wang, T. & Kwei, T. Diffusion in glassy polymers. II. *J. Polym. Sci. A-2* **7**, 879–887 (1969).
27. Mao, X., Yuk, H. & Zhao, X. Hydration and swelling of dry polymers for wet adhesion. *J. Mech. Phys. Solids* **137**, 103863 (2020).
28. Lendlein, A. & Langer, R. Biodegradable, elastic shape-memory polymers for potential biomedical applications. *Science* **296**, 1673–1676 (2002).
29. Mather, P. T., Luo, X. & Rousseau, I. A. Shape memory polymer research. *Annu. Rev. Mater. Res.* **39**, 445–471 (2009).

30. Meng, H. & Li, G. A review of stimuli-responsive shape memory polymer composites. *Polymer* **54**, 2199–2221 (2013).
31. Chen, X., Yuk, H., Wu, J., Nabzdyk, C. S. & Zhao, X. Instant tough bioadhesive with triggerable benign detachment. *Proc. Natl Acad. Sci. USA* **117**, 15497–15503 (2020).
32. Upton, D., Solowiej, K., Hender, C. & Woo, K. Stress and pain associated with dressing change in patients with chronic wounds. *J. Wound Care* **21**, 53–61 (2012).
33. Than, U. T. T., Guanzon, D., Leavesley, D. & Parker, T. Association of extracellular membrane vesicles with cutaneous wound healing. *Int. J. Mol. Sci.* <https://doi.org/10.3390/ijms18050956> (2017).
34. Flynn, C., Taberner, A. & Nielsen, P. Mechanical characterisation of in vivo human skin using a 3D force-sensitive micro-robot and finite element analysis. *Biomech. Model. Mechanobiol.* **10**, 27–38 (2011).
35. Berezovsky, A. B. et al. Primary contraction of skin grafts: a porcine preliminary study. *Plast. Aesthet. Res.* **25**, 22–26 (2015).
36. Joodaki, H. & Panzer, M. B. Skin mechanical properties and modeling: a review. *Proc. Inst. Mech. Eng. H* **232**, 323–343 (2018).
37. Grada, A., Mervis, J. & Falanga, V. Research techniques made simple: animal models of wound healing. *J. Invest. Dermatol.* **138**, 2095–2105.e1 (2018).
38. Scherer, S. S. et al. Wound healing kinetics of the genetically diabetic mouse. *Wounds* **20**, 18–28 (2008).
39. Volk, S. W. & Bohling, M. W. Comparative wound healing—are the small animal veterinarian's clinical patients an improved translational model for human wound healing research? *Wound Repair Regen.* **21**, 372–381 (2013).
40. Chen, L., Mirza, R., Kwon, Y., DiPietro, L. A. & Koh, T. J. The murine excisional wound model: contraction revisited. *Wound Repair Regen.* **23**, 874–877 (2015).
41. Wang, X. T., McKeever, C. C., Vonu, P., Patterson, C. & Liu, P. Y. Dynamic histological events and molecular changes in excisional wound healing of diabetic DB/DB mice. *J. Surg. Res.* **238**, 186–197 (2019).
42. Hinz, B. Formation and function of the myofibroblast during tissue repair. *J. Invest. Dermatol.* **127**, 526–537 (2007).
43. Rinkevich, Y. et al. Skin fibrosis. Identification and isolation of a dermal lineage with intrinsic fibrogenic potential. *Science* **348**, aaa2151 (2015).
44. Mascharak, S. et al. Preventing Engrailed-1 activation in fibroblasts yields wound regeneration without scarring. *Science* **372**, eaba2374 (2021).
45. Jiang, D. et al. Two succeeding fibroblastic lineages drive dermal development and the transition from regeneration to scarring. *Nat. Cell Biol.* **20**, 422–431 (2018).
46. Shook, B. A. et al. Dermal adipocyte lipolysis and myofibroblast conversion are required for efficient skin repair. *Cell Stem Cell* **26**, 880–895.e6 (2020).
47. Plikus, M. V. et al. Regeneration of fat cells from myofibroblasts during wound healing. *Science* **355**, 748–752 (2017).
48. Joshi, N. et al. Comprehensive characterization of myeloid cells during wound healing in healthy and healing-impaired diabetic mice. *Eur. J. Immunol.* **50**, 1335–1349 (2020).
49. Mariani, E., Lisignoli, G., Borzi, R. M. & Pulsatelli, L. Biomaterials: foreign bodies or tuners for the immune response? *Int. J. Mol. Sci.* <https://doi.org/10.3390/ijms20030636> (2019).
50. Krzyszczyk, P., Schloss, R., Palmer, A. & Berthiaume, F. The role of macrophages in acute and chronic wound healing and interventions to promote pro-wound healing phenotypes. *Front. Physiol.* **9**, 419 (2018).
51. Gay, D. et al. Phagocytosis of Wnt inhibitor SFRP4 by late wound macrophages drives chronic Wnt activity for fibrotic skin healing. *Sci. Adv.* **6**, eaay3704 (2020).
52. Acharya, P. S. et al. Fibroblast migration is mediated by CD44-dependent TGF β activation. *J. Cell Sci.* **121**, 1393–1402 (2008).
53. Ruiz-Ederra, J. & Verkman, A. Aquaporin-1-facilitated keratocyte migration in cell culture and in vivo corneal wound healing models. *Exp. Eye Res.* **89**, 159–165 (2009).
54. Xie, T. et al. Single-cell deconvolution of fibroblast heterogeneity in mouse pulmonary fibrosis. *Cell Rep.* **22**, 3625–3640 (2018).
55. Stojadinovic, O. & Tomic-Canic, M. Human ex vivo wound healing model. *Methods Mol. Biol.* **1037**, 255–264 (2013).
56. Gherardini, J., van Lessen, M., Piccini, I., Edelkamp, J. & Bertolini, M. Human wound healing ex vivo model with focus on molecular markers. *Methods Mol. Biol.* **2154**, 249–254 (2020).
57. Summerfield, A., Meurens, F. & Ricklin, M. E. The immunology of the porcine skin and its value as a model for human skin. *Mol. Immunol.* **66**, 14–21 (2015).
58. Chen, K. et al. Disrupting biological sensors of force promotes tissue regeneration in large organisms. *Nat. Commun.* **12**, 5256 (2021).
59. Martínez-Santamaría, L. et al. The regenerative potential of fibroblasts in a new diabetes-induced delayed humanised wound healing model. *Exp. Dermatol.* **22**, 195–201 (2013).
60. Ding, J. & Tredget, E. E. in *Fibrosis. Methods in Molecular Biology* Vol. 1627 (ed. Rittié, L.) 65–80 (Humana Press, 2017).
61. Démarchez, M., Hartmann, D. J., Herbage, D., Ville, G. & Pruniéras, M. Wound healing of human skin transplanted onto the nude mouse: II. An immunohistological and ultrastructural study of the epidermal basement membrane zone reconstruction and connective tissue reorganization. *Dev. Biol.* **121**, 119–129 (1987).
62. Driver, V. R. et al. A clinical trial of Integra Template for diabetic foot ulcer treatment. *Wound Repair Regen.* **23**, 891–900 (2015).
63. Baltzis, D., Eleftheriadou, I. & Veves, A. Pathogenesis and treatment of impaired wound healing in diabetes mellitus: new insights. *Adv. Ther.* **31**, 817–836 (2014).
64. Castleberry, S. A. et al. Self-assembled wound dressings silence MMP-9 and improve diabetic wound healing in vivo. *Adv. Mater.* **28**, 1809–1817 (2016).
65. Shibata, S. et al. Adiponectin regulates cutaneous wound healing by promoting keratinocyte proliferation and migration via the ERK signaling pathway. *J. Immunol.* **189**, 3231–3241 (2012).
66. Gao, M. et al. Acceleration of diabetic wound healing using a novel protease-anti-protease combination therapy. *Proc. Natl Acad. Sci. USA* **112**, 15226–15231 (2015).
67. Brown, R. L., Breeden, M. P. & Greenhalgh, D. G. PDGF and TGF- α act synergistically to improve wound healing in the genetically diabetic mouse. *J. Surg. Res.* **56**, 562–570 (1994).
68. Smiell, J. M. et al. Efficacy and safety of becaplermin (recombinant human platelet-derived growth factor-BB) in patients with nonhealing, lower extremity diabetic ulcers: a combined analysis of four randomized studies. *Wound Repair Regen.* **7**, 335–346 (1999).
69. Leal, E. C. et al. Substance P promotes wound healing in diabetes by modulating inflammation and macrophage phenotype. *Am. J. Pathol.* **185**, 1638–1648 (2015).
70. Tellechea, A. et al. Topical application of a mast cell stabilizer improves impaired diabetic wound healing. *J. Invest. Dermatol.* **140**, 901–911.e911 (2020).
71. Stone, R. C. et al. A bioengineered living cell construct activates an acute wound healing response in venous leg ulcers. *Sci. Transl. Med.* <https://doi.org/10.1126/scitranslmed.aaf8611> (2017).
72. Theocharidis, G. et al. Integrated skin transcriptomics and serum multiplex assays reveal novel mechanisms of wound healing in diabetic foot ulcers. *Diabetes* **69**, 2157–2169 (2020).
73. Asp, M., Bergenstrahle, J. & Lundberg, J. Spatially resolved transcriptomes—next generation tools for tissue exploration. *Bioessays* **42**, e1900221 (2020).
74. Martin, M. Cutadapt removes adapter sequences from high-throughput sequencing reads. *EMBnet J.* **17**, 10–12 (2011).
75. Conesa, A. et al. A survey of best practices for RNA-seq data analysis. *Genome Biol.* **17**, 13 (2016).
76. Cunningham, F. et al. Ensembl 2019. *Nucleic Acids Res.* **47**, D745–D751 (2019).
77. Dobin, A. et al. STAR: ultrafast universal RNA-seq aligner. *Bioinformatics* **29**, 15–21 (2013).
78. Liao, Y., Smyth, G. K. & Shi, W. featureCounts: an efficient general purpose program for assigning sequence reads to genomic features. *Bioinformatics* **30**, 923–930 (2014).
79. Love, M. I., Huber, W. & Anders, S. Moderated estimation of fold change and dispersion for RNA-seq data with DESeq2. *Genome Biol.* **15**, 550 (2014).
80. Yu, G., Wang, L.-G., Han, Y. & He, Q.-Y. clusterProfiler: an R package for comparing biological themes among gene clusters. *OMICS* **16**, 284–287 (2012).
81. Newman, A. M. et al. Determining cell type abundance and expression from bulk tissues with digital cytometry. *Nat. Biotechnol.* **37**, 773–782 (2019).
82. Subramanian, A. et al. Gene set enrichment analysis: a knowledge-based approach for interpreting genome-wide expression profiles. *Proc. Natl Acad. Sci. USA* **102**, 15545–15550 (2005).

Acknowledgements

We thank the Koch Institute Swanson Biotechnology Center for technical support, specifically K. Cormier and the Histology Core for the histological processing and analysis. This work was supported by Defense Advanced Research Projects Agency (DARPA) (5(GG0015670) to X.Z. and A.V.) and Department of Defense Congressionally Directed Medical Research Programs (CDMRP) (PR200524P1 to X.Z. and A.V.). A.V. received funding from the National Rongxiang Xu Foundation. G.T. received a George and Marie Vergottis Foundation Postdoctoral Fellowship. H.Y. acknowledges the financial support from Samsung Scholarship. H.R. acknowledges the financial support from Kwanjeong Educational Foundation Scholarship.

Author contributions

H.Y., G.T., A.V. and X.Z. designed the study. H.Y. conceived the idea and developed the materials and method for the strain-programmed patch. H.Y., H.R. and C.S.N. designed the in vitro and ex vivo experiment. H.Y. and H.R. conducted the in vitro and ex vivo experiment and analysis. L.W. and C.F.G. designed and conducted the theoretical and numerical modelling and analysis. H.Y. and J.W. designed and conducted the in vivo biocompatibility experiment. G.T., I.M., L.C. and A.V. designed and conducted the

in vivo diabetic mouse wound healing experiment and analysis. G.T., M.C., B.S. and A.V. designed and conducted the in vivo diabetic porcine wound healing experiment. G.T., I.M., B.S., L.Z. and E.W. designed and conducted the in vivo diabetic humanized mice wound healing experiment. G.T., I.M., Z.L., E.W. and N.J. completed the flow cytometry, histology, immunofluorescence, gene expression and human skin ex vivo experiment analyses. A.K. performed histology assessment and scoring. X.-L.K., N.K. and I.S.V. performed sequencing analysis. H.Y. and G.T. prepared the figures. G.T., H.Y., X.Z. and A.V. wrote the manuscript with inputs from all authors.

Competing interests

H.Y., H.R., X.Z., G.T. and A.V. are the inventors of a patent application (U.S. Application No. 63/148,901) that covers the design and mechanism of the strain-programmed patch for diabetic wound healing. H.Y., C.S.N. and X.Z. have a financial interest in SanaHeal, Inc., a biotechnology company focused on the development of medical devices for surgical sealing and repair. All other authors declare no competing interests.

Additional information

Extended data is available for this paper at <https://doi.org/10.1038/s41551-022-00905-2>.

Supplementary information The online version contains supplementary material available at <https://doi.org/10.1038/s41551-022-00905-2>.

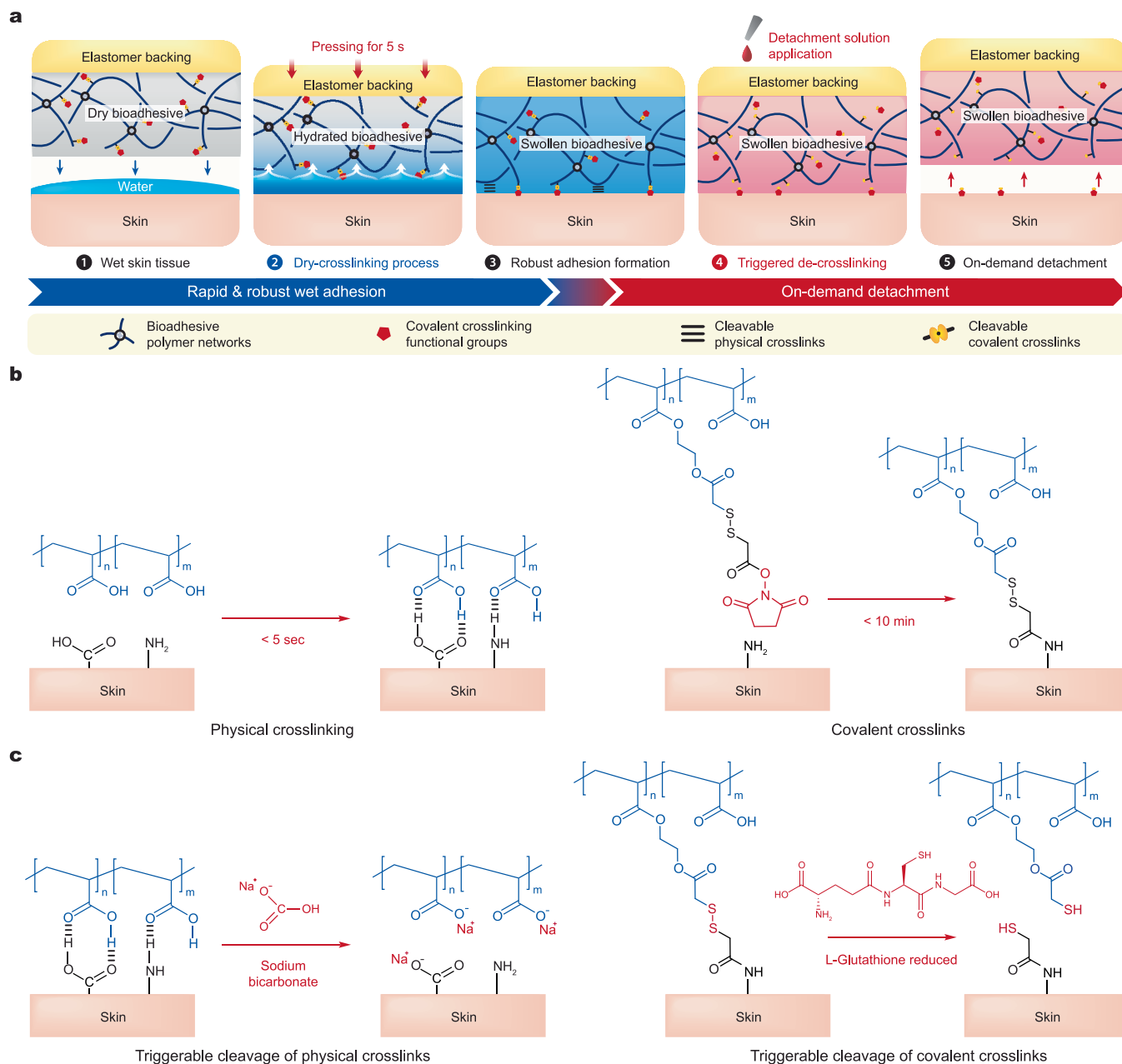
Correspondence and requests for materials should be addressed to Hyunwoo Yuk, Aristidis Veves or Xuanhe Zhao.

Peer review information *Nature Biomedical Engineering* thanks the anonymous reviewers for their contribution to the peer review of this work. Peer reviewer reports are available.

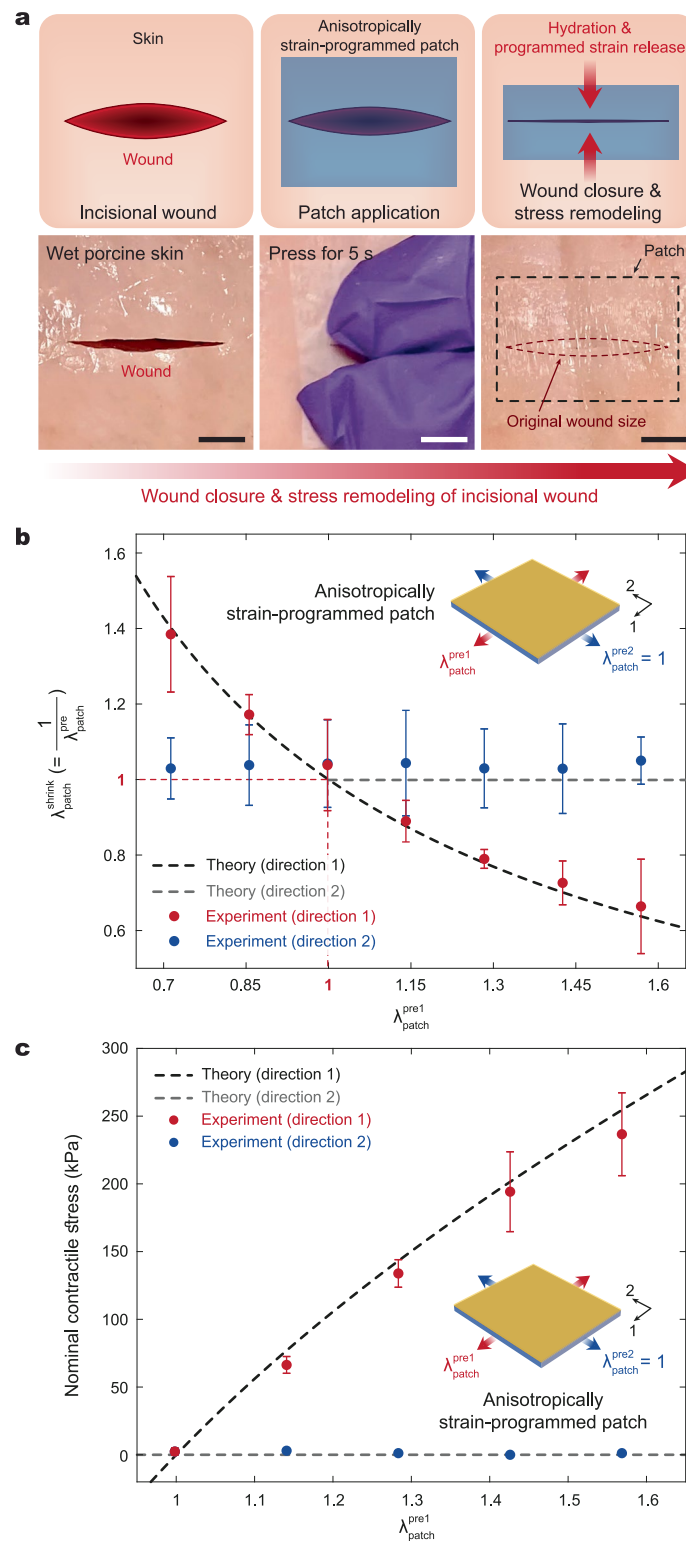
Reprints and permissions information is available at www.nature.com/reprints.

Publisher's note Springer Nature remains neutral with regard to jurisdictional claims in published maps and institutional affiliations.

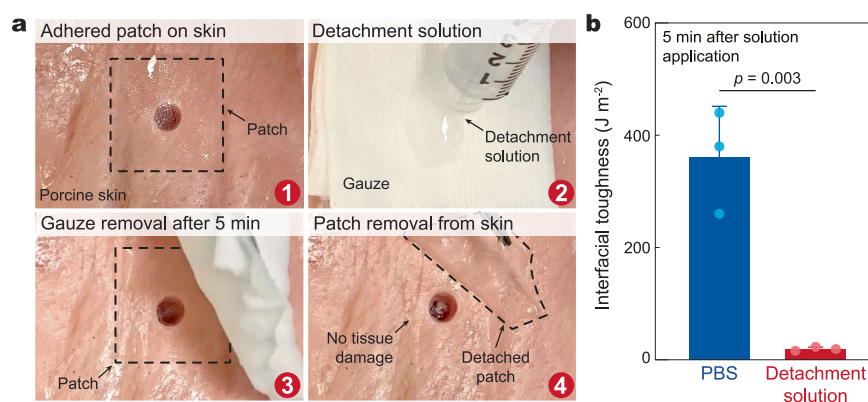
© The Author(s), under exclusive licence to Springer Nature Limited 2022



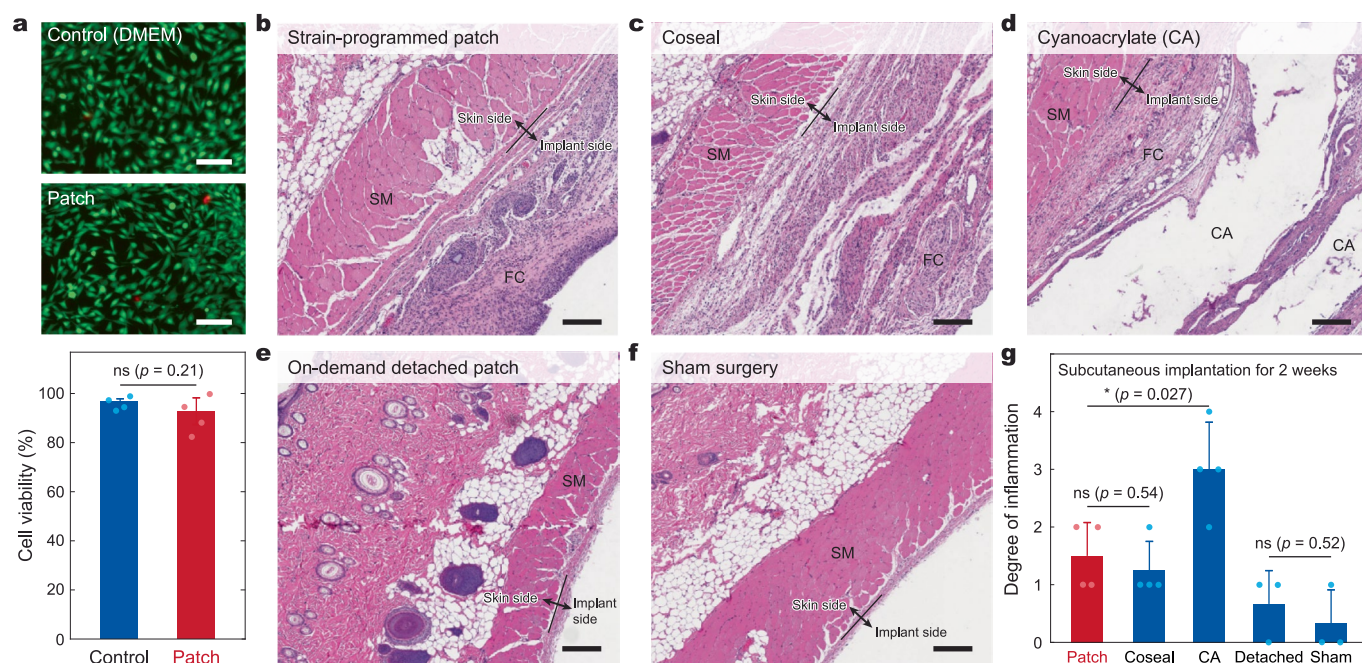
Extended Data Fig. 1 | Rapid wet adhesion and on-demand detachment of the strain-programmed patch. a, Rapid wet adhesion and on-demand detachment of the strain-programmed patch. **b,c**, Chemistry of the physical and covalent crosslinks for rapid wet adhesion (b) and on-demand detachment (c) of the strain-programmed patch.



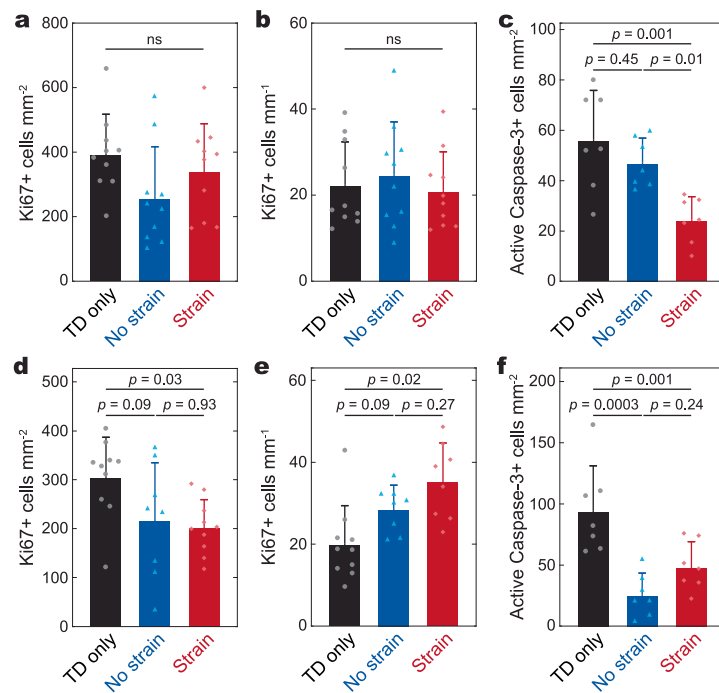
Extended Data Fig. 2 | Anisotropically strain-programmed patch. **a**, Closure of an incisional wound on porcine skin by the anisotropically strain-programmed patch. **b,c**, Theoretical and experimental values of contraction ($\lambda_{\text{shrink patch}}^{\text{pre}}$) (b) and nominal contractile stress (c) generated by programmed strain release upon hydration of the anisotropically strain-programmed patch with varying $\lambda_{\text{patch}}^{\text{pre1}}$. Values in **b,c** represent the mean and the standard deviation ($n = 4$; independent samples). Scale bars, 10 mm (a).



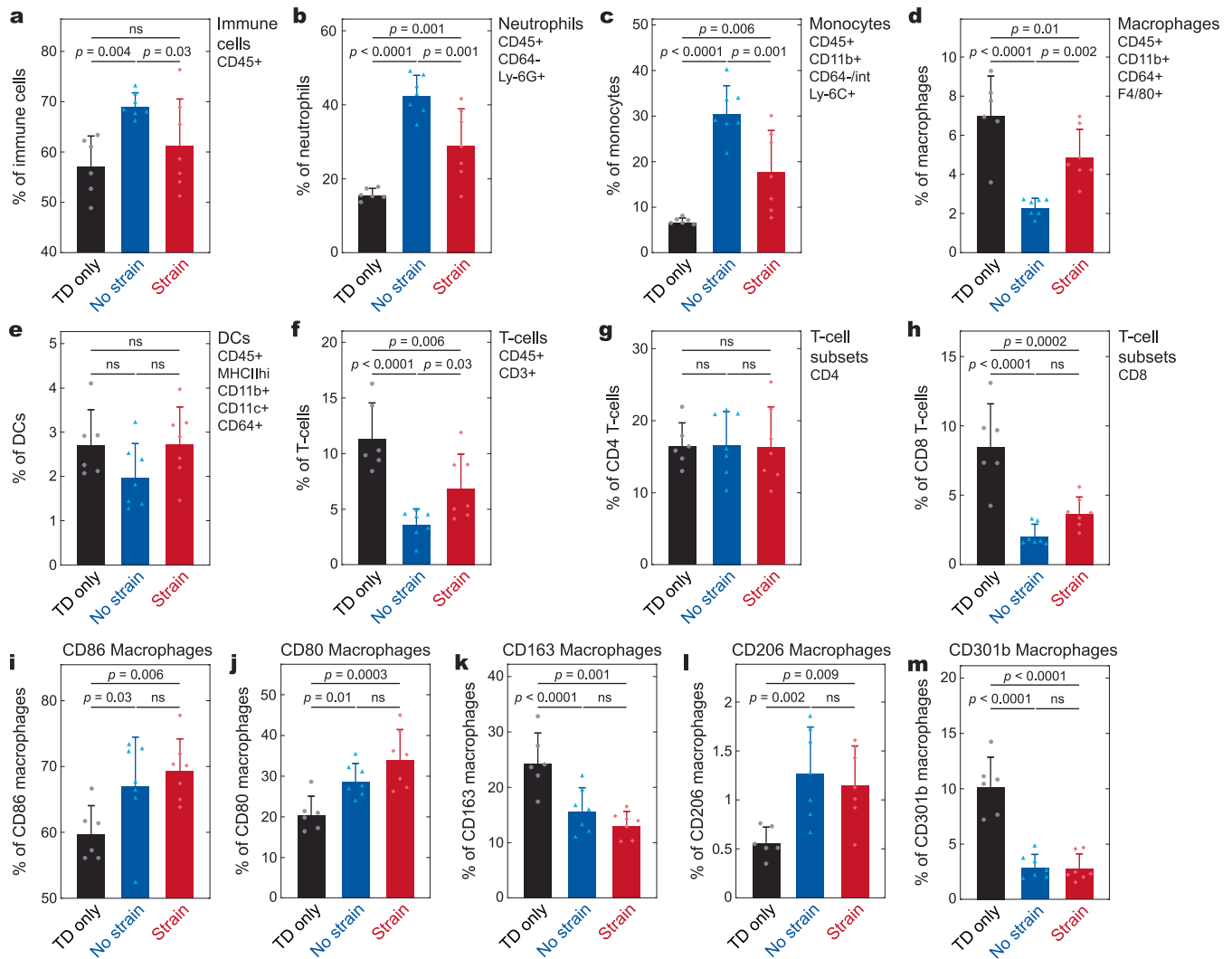
Extended Data Fig. 3 | On-demand detachment of the strain-programmed patch. **a**, On-demand detachment of the strain-programmed patch adhered on a porcine skin by application of a detachment solution. **b**, Interfacial toughness of the strain-programmed patch adhered on porcine skin 5 min after applying PBS or the detachment solution. Values in **b** represent the mean and the standard deviation ($n=3$; independent samples). Statistical significance and p values are determined by two-sided t -test.



Extended Data Fig. 4 | In vitro and in vivo biocompatibility of the strain-programmed patch. **a**, Representative LIVE/DEAD assay images and the cell viability of mouse embryonic fibroblasts (mEFs) for control (DMEM) and the strain-programmed patch after 24-h culture. DMEM, Dulbecco's modified eagle medium. **b-f**, Representative histological images for the subcutaneously implanted strain-programmed patch (**b**), Coseal (**c**), Dermabond cyanoacrylate (CA) adhesive (**d**), strain-programmed patch after on-demand detachment (**e**), and sham surgery (**f**) after 2 weeks post-implantation stained with hematoxylin and eosin (H&E). **g**, Degree of inflammation of various groups evaluated by a blinded pathologist (0, normal; 1, mild; 2, moderate; 3, severe; 4, very severe) after 2 weeks post-implantation. Skin side and implant side in the histological images are indicated by arrows. SM, skeletal muscle; FC, fibrous capsule. All experiments are repeated four biological replicates with similar results. Values in **a,g** represent the mean and the standard deviation ($n = 4$; independent samples). Statistical significance and p values are determined by two-sided t -test; ns, not significant; * $p < 0.05$. Scale bars, 200 μm (a-f).

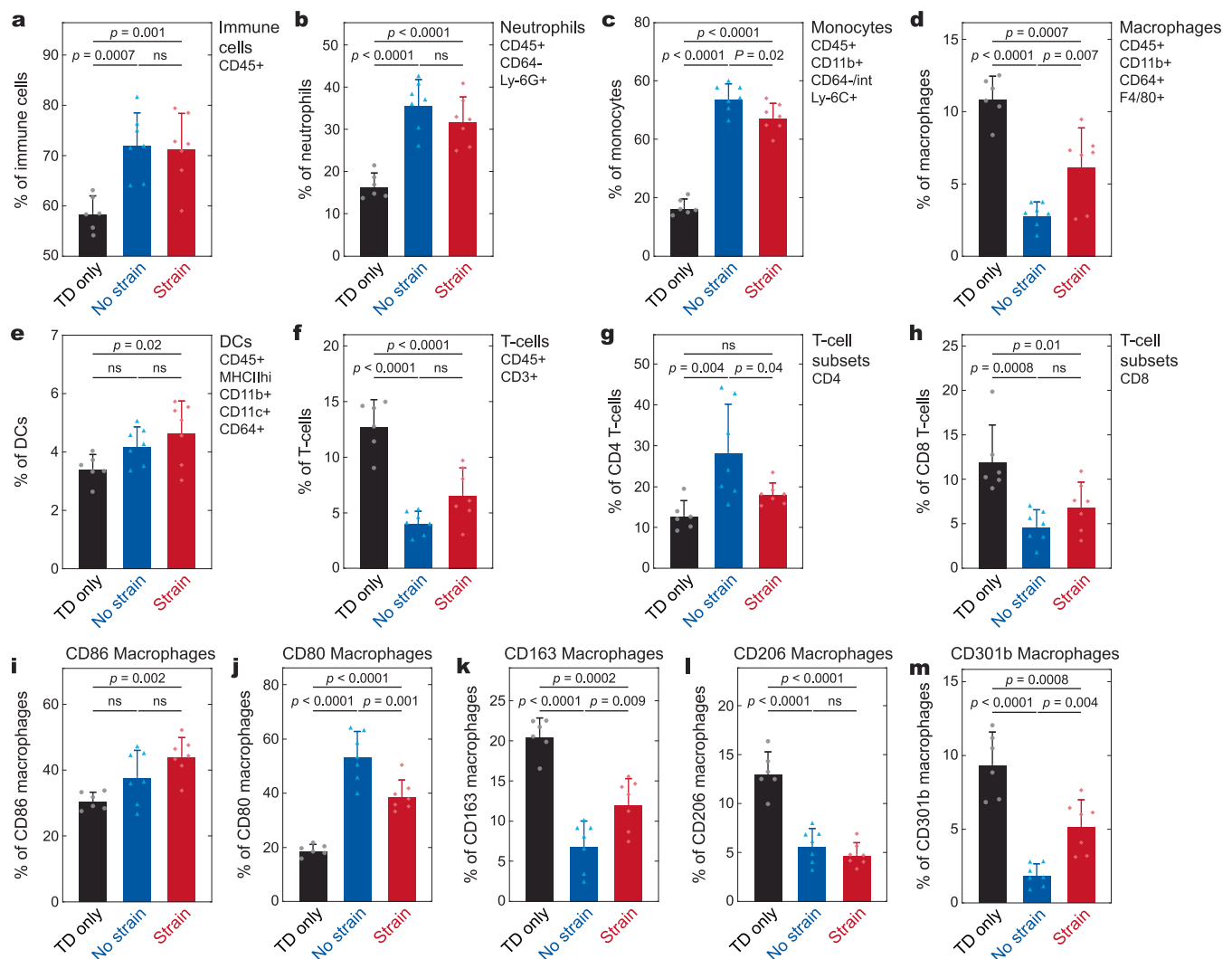


Extended Data Fig. 5 | Proliferation and apoptosis of the wound cells. **a,b**, Quantification of proliferation marker Ki67+ cells in the dermis (a) and the epidermis (b) of day 5 (D5) wounds. **c**, Quantification of apoptosis marker active Caspase-3+ cells in the dermis of D5 wounds. **d,e**, Quantification of proliferation marker Ki67+ cells in the dermis (d) and the epidermis (e) of day 10 (D10) wounds. **f**, Quantification of apoptosis marker active Caspase-3+ cells in the dermis of D10 wounds. Values represent the mean and the standard deviation ($n = 10$ in **a** and **b**; $n = 7$ in **c** and **f**; $n = 10$ for TD Only, 8 for No Strain and 10 for Strain in **d**; $n = 10$ for TD Only, 8 for No Strain and 8 for Strain in **e**; independent samples). Statistical significance and p values are determined by one-way ANOVA followed by Tukey's multiple comparison test; ns, not significant.



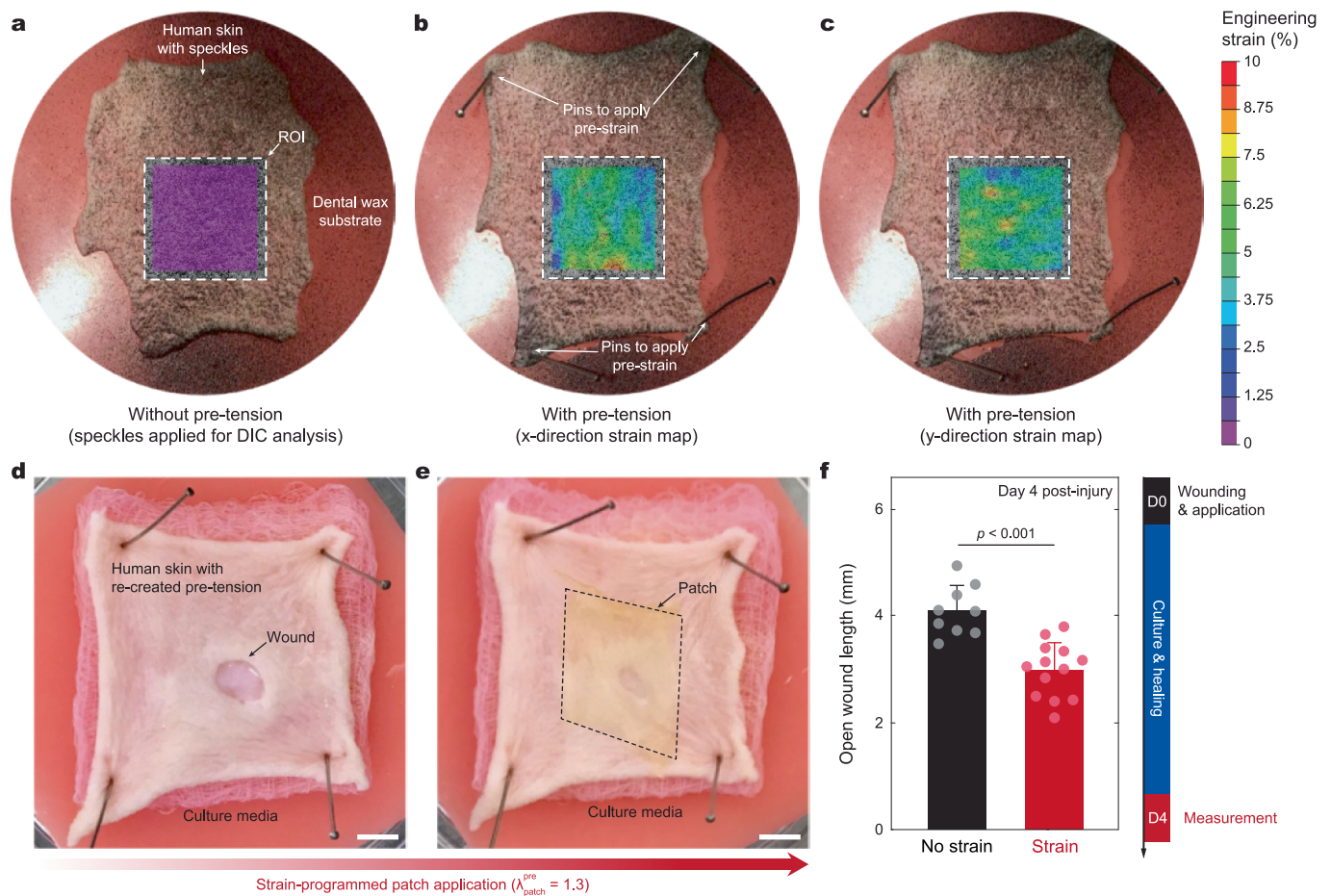
Extended Data Fig. 6 | Flow-cytometric quantification of major immune cell populations and macrophage polarized states in D5 wounds.

a-m, Single-cell suspensions were generated from excised wound and peri-wound tissues and stained for the indicated cell surface proteins. Percentage of immune cells (a), neutrophils (b), monocytes (c), macrophages (d), dendritic cells (DCs) (e), and T-cells (f) and T-cell subsets (g,h). Percentage of macrophages expressing markers CD86 (i), CD80 (j), CD163 (k), CD206 (l), and CD301b (m). Each data point represents pooled cells from two mice (four wounds). Values represent the mean and the standard deviation ($n=6$ for TD Only, 7 for No Strain and 7 for Strain; independent samples). Statistical significance and p values are determined by one-way ANOVA followed by Fisher's least significant difference (LSD) post-hoc test; ns, not significant.

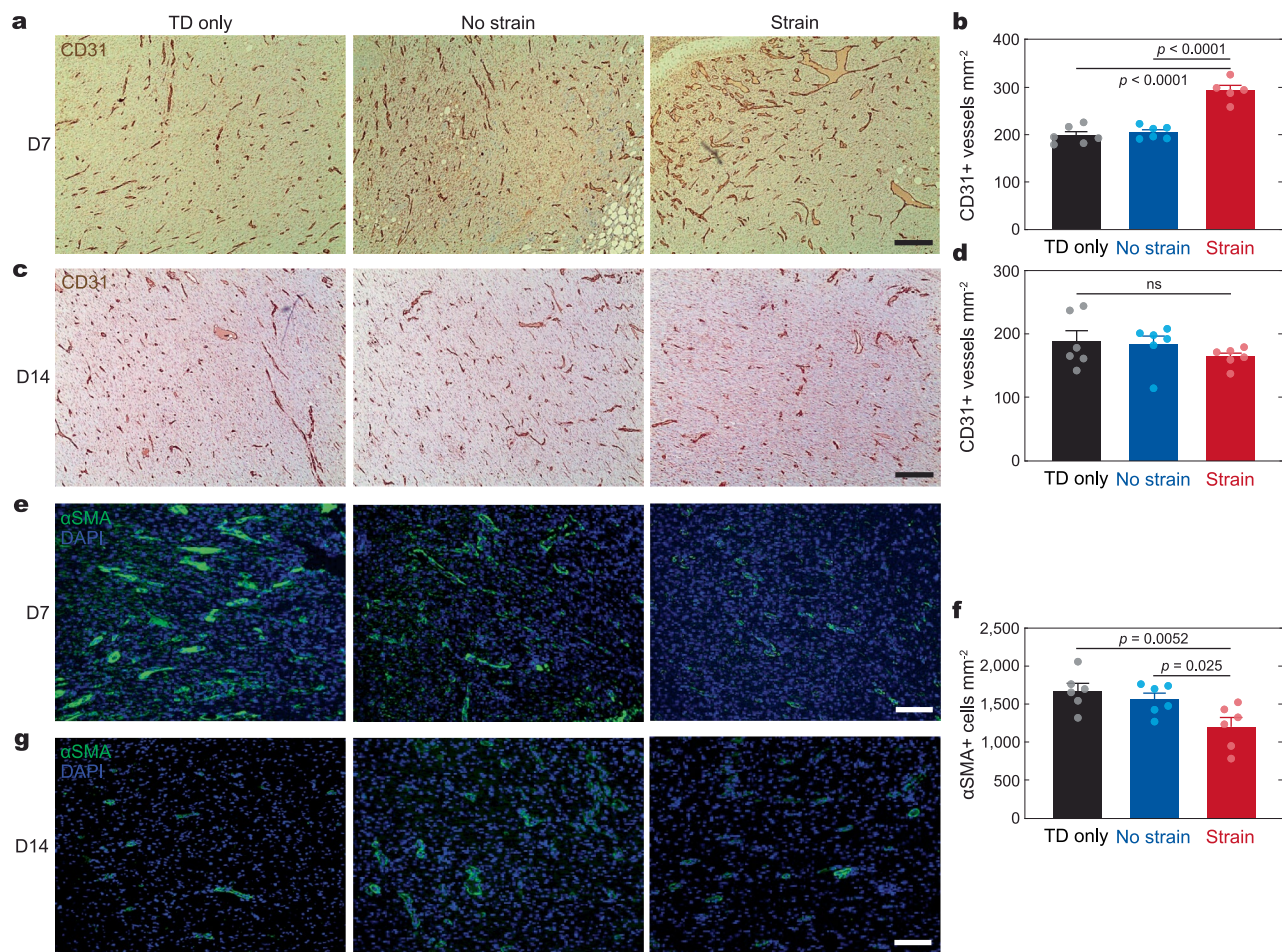


Extended Data Fig. 7 | Flow-cytometric quantification of major immune cell populations and macrophage polarized states in D10 wounds.

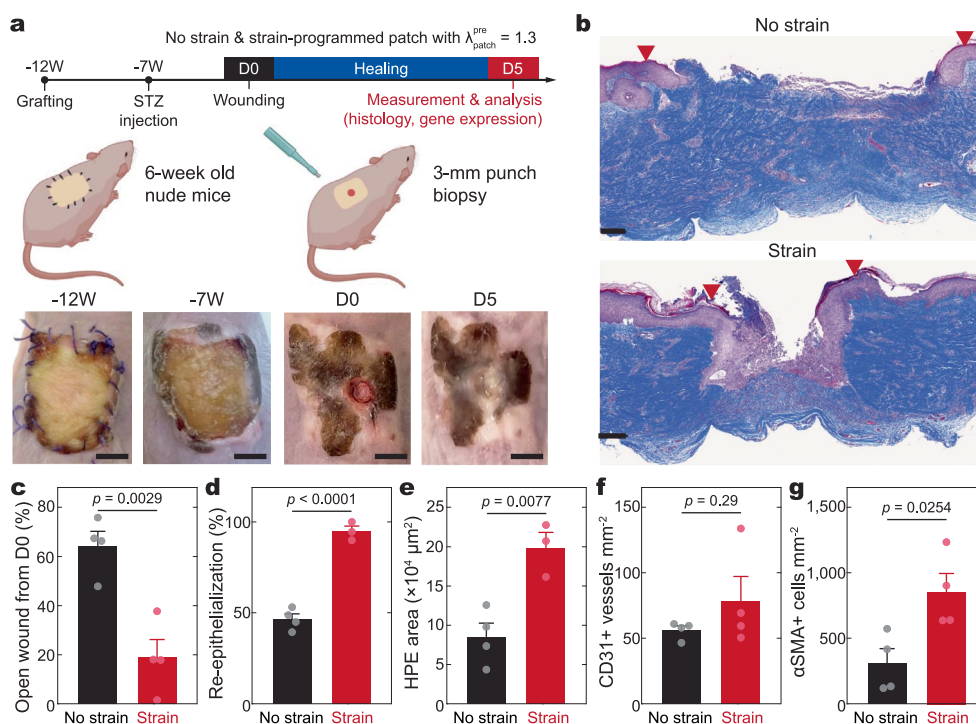
a-m, Single-cell suspensions were generated from excised wound and peri-wound tissues and stained for the indicated cell surface proteins. Percentage of immune cells (a), neutrophils (b), monocytes (c), macrophages (d), dendritic cells (DCs) (e), and T-cells (f) and T-cell subsets (g,h). Percentage of macrophages expressing markers CD86 (i), CD80 (j), CD163 (k), CD206 (l), and CD301b (m). Each data point represents pooled cells from two mice (four wounds). Values represent the mean and the standard deviation ($n=6$ for TD Only, 7 for No Strain and 7 for Strain; independent samples). Statistical significance and p values are determined by one-way ANOVA followed by Fisher's least significant difference (LSD) post-hoc test; ns, not significant.



Extended Data Fig. 8 | Ex vivo human skin wound-healing model with pre-tension. a–c, Ex vivo human skin with speckles and corresponding digital image correlation (DIC) analysis results without pre-tension (a) and with pre-tension in x-direction (b) and in y-direction (c). ROI, region of interest. **d,e,** Representative images of an ex vivo human skin culture setup with pre-tension before (d) and after (e) the strain-programmed patch application. **f,** Quantification of the open wound length on day 4 (D4) post-injury. Values in **f** represent the mean and the standard deviation ($n=9$ wounds for No Strain and 13 wounds for Strain from 2 individual patients' skin; independent samples). Statistical significance and p values are determined by two-sided t -test. Scale bars, 5 mm (d,e).



Extended Data Fig. 9 | Immunostaining analysis of diabetic in vivo wound healing of porcine skin. **a,b**, Representative immunohistochemistry images for CD31 (**a**) and quantification of CD31+ vessels per unit area (**b**) on day 7 (D7). **c,d**, Representative immunohistochemistry images for CD31 (**c**) and quantification of CD31+ vessels per unit area (**d**) on day 14 (D14). **e,f**, Representative immunofluorescence images for αSMA (**e**) and quantification of αSMA+ cells per unit area (**f**) on D7. **g**, Representative immunofluorescence images for αSMA on D14. In immunohistochemistry images, the NOVA Red peroxidase substrate chromogenic stain was used. In immunofluorescence images, blue fluorescence corresponds to cell nuclei stained with 4',6-diamidino-2-phenylindole (DAPI); green fluorescence corresponds to the expression of αSMA. Experimental groups are Tegaderm (TD) only, no strain ($\lambda_{\text{patch}}^{\text{pre}} = 1$) and strain-programmed ($\lambda_{\text{patch}}^{\text{pre}} = 1.3$) patch for both D7 and D14. Values in **b,d,f** represent the mean and the standard deviation ($n = 6$; independent samples). Statistical significance and p values are determined by one-way ANOVA followed by Fisher's least significant difference (LSD) post-hoc test; ns, not significant. Scale bars, 100 μm (**a,c,e,g**).



Extended Data Fig. 10 | Accelerated diabetic in vivo wound healing of humanized mouse skin. **a**, Schematic illustrations for the xenotransplantation procedure, diabetes induction, and experimental plan. W, week. **b**, Representative images from Day 5 wounds with Masson's trichrome stain (MTS). Red triangles denote wound margins. **c–g**, Quantification of the wound closure expressed as % of open wound compared to Day 0 (**c**), the re-epithelialization expressed as % (**d**), the hyperproliferative epidermis (HPE) area (**e**), the number of CD31+ vessels per unit area (**f**), and the number of $\alpha\text{SMA}+$ cells per unit area (**g**) on Day 5. Values in **c–g** represent the mean and the standard deviation ($n = 4$ in **c, f, g**; $n = 4$ for No Strain and 3 for Strain in **d** and **e**; independent samples). Statistical significance and p values are determined by two-sided t -test. Scale bars, 5 mm (**a**); 250 μm (**b**). Parts of (**a**) were created with BioRender.com.

Reporting Summary

Nature Research wishes to improve the reproducibility of the work that we publish. This form provides structure for consistency and transparency in reporting. For further information on Nature Research policies, see our [Editorial Policies](#) and the [Editorial Policy Checklist](#).

Statistics

For all statistical analyses, confirm that the following items are present in the figure legend, table legend, main text, or Methods section.

- | n/a | Confirmed |
|-------------------------------------|--|
| <input type="checkbox"/> | <input checked="" type="checkbox"/> The exact sample size (n) for each experimental group/condition, given as a discrete number and unit of measurement |
| <input type="checkbox"/> | <input checked="" type="checkbox"/> A statement on whether measurements were taken from distinct samples or whether the same sample was measured repeatedly |
| <input type="checkbox"/> | <input checked="" type="checkbox"/> The statistical test(s) used AND whether they are one- or two-sided
<i>Only common tests should be described solely by name; describe more complex techniques in the Methods section.</i> |
| <input checked="" type="checkbox"/> | <input type="checkbox"/> A description of all covariates tested |
| <input type="checkbox"/> | <input checked="" type="checkbox"/> A description of any assumptions or corrections, such as tests of normality and adjustment for multiple comparisons |
| <input type="checkbox"/> | <input checked="" type="checkbox"/> A full description of the statistical parameters including central tendency (e.g. means) or other basic estimates (e.g. regression coefficient) AND variation (e.g. standard deviation) or associated estimates of uncertainty (e.g. confidence intervals) |
| <input type="checkbox"/> | <input checked="" type="checkbox"/> For null hypothesis testing, the test statistic (e.g. F , t , r) with confidence intervals, effect sizes, degrees of freedom and P value noted
<i>Give P values as exact values whenever suitable.</i> |
| <input checked="" type="checkbox"/> | <input type="checkbox"/> For Bayesian analysis, information on the choice of priors and Markov chain Monte Carlo settings |
| <input checked="" type="checkbox"/> | <input type="checkbox"/> For hierarchical and complex designs, identification of the appropriate level for tests and full reporting of outcomes |
| <input checked="" type="checkbox"/> | <input type="checkbox"/> Estimates of effect sizes (e.g. Cohen's d , Pearson's r), indicating how they were calculated |

Our web collection on [statistics for biologists](#) contains articles on many of the points above.

Software and code

Policy information about [availability of computer code](#)

Data collection	No software was used for data collection.
Data analysis	<p>Microscopic images were analysed by using ImageJ (Version: 2.1.0). All statistical analyses were performed by using Prism (Version: 7.04 GraphPad). Digital image correlation (DIC) analysis was performed with Vic-2D (version 2009). Flow-cytometry data analysis was performed with CytExpert (version 2.4).</p> <p>Raw sequencing data (.bcl files) generated from Illumina HiSeq were converted into fastq files and de-multiplexed using Illumina's bcl2fastq software (version 2.17). Read quality was evaluated using FastQC (version 0.11.9) and data were preprocessed with Cutadapt (version 3.1). Gene expression against the GRCm38 transcriptome (Ensembl 93 version) was quantified with STAR (version 2.7.3a) and featureCounts (version 1.6.2). Differential gene-expression analysis was performed using DESeq2 (version 1.31.2), while ClusterProfiler (version 3.18) was used for functional-enrichment investigations. Gene Set Enrichment Analysis (GSEA version 4.2.3) was used to assess differences in gene-signatures enrichment between groups.</p>

For manuscripts utilizing custom algorithms or software that are central to the research but not yet described in published literature, software must be made available to editors and reviewers. We strongly encourage code deposition in a community repository (e.g. GitHub). See the Nature Research [guidelines for submitting code & software](#) for further information.

Data

Policy information about [availability of data](#)

All manuscripts must include a [data availability statement](#). This statement should provide the following information, where applicable:

- Accession codes, unique identifiers, or web links for publicly available datasets
- A list of figures that have associated raw data
- A description of any restrictions on data availability

The main data supporting the results in this study are available within the paper and its Supplementary Information. The RNA-seq data are available from the Gene Expression Omnibus (GEO) database, with accession number GSE154132. Publicly available single-cell RNA-seq data were obtained from GEO (accession number, GSE141814). Additional raw datasets generated during the study are too large to be publicly shared, yet they are available from the corresponding authors on reasonable request.

Field-specific reporting

Please select the one below that is the best fit for your research. If you are not sure, read the appropriate sections before making your selection.

☒ Life sciences ☐ Behavioural & social sciences ☐ Ecological, evolutionary & environmental sciences

For a reference copy of the document with all sections, see nature.com/documents/nr-reporting-summary-flat.pdf

Life sciences study design

All studies must disclose on these points even when the disclosure is negative.

Sample size	<p>In vivo experiments on rats were conducted to investigate biocompatibility. An appropriate sample size (n = 4) was used on the basis of published literature on similar evaluations (for example, Yuk et al., Nature 575, 169–174 (2019)).</p> <p>In vivo experiments on db/db and nude diabetic humanized mice and diabetic swine were conducted to investigate in vivo diabetic wound healing. An appropriate sample size was used on the basis of published literature on similar evaluations and of a pilot experiment for power analysis. The pilot study showed that, when comparing the closure of mice wounds treated with the control versus those treated with the patches, we had three levels, a pooled standard deviation of 15 and a minimum difference between the two patches and the control group of 33, which indicated that 6 wounds per group would allow us to detect a difference in wound-healing improvement with 80% power and a 5% level of significance. Expecting similar effects with the swine model, we also included at least 6 wounds per treatment group.</p> <p>We also expected similar effects in the ex vivo human wound-healing experiments, and included at least 6 wounds per treatment group created on skin specimens collected from 3 (non pre-stretch model) or 2 (pre-stretch model) different patients.</p>
Data exclusions	No data were excluded.
Replication	The in vivo studies for biocompatibility and diabetic wound healing were reliably reproduced, on the basis of comparable histological assessment for each case by the blinded pathologist. All in vivo studies were independently performed with at least 1 day between surgeries. All attempts at replication were successful.
Randomization	All the tests were performed with randomly allocated experimental groups.
Blinding	All measurements were conducted in a blinded fashion.

Reporting for specific materials, systems and methods

We require information from authors about some types of materials, experimental systems and methods used in many studies. Here, indicate whether each material, system or method listed is relevant to your study. If you are not sure if a list item applies to your research, read the appropriate section before selecting a response.

Materials & experimental systems

n/a	Involved in the study
<input type="checkbox"/>	<input checked="" type="checkbox"/> Antibodies
<input type="checkbox"/>	<input checked="" type="checkbox"/> Eukaryotic cell lines
<input checked="" type="checkbox"/>	<input type="checkbox"/> Palaeontology and archaeology
<input type="checkbox"/>	<input checked="" type="checkbox"/> Animals and other organisms
<input checked="" type="checkbox"/>	<input type="checkbox"/> Human research participants
<input checked="" type="checkbox"/>	<input type="checkbox"/> Clinical data
<input checked="" type="checkbox"/>	<input type="checkbox"/> Dual use research of concern

Methods

n/a	Involved in the study
<input checked="" type="checkbox"/>	<input type="checkbox"/> ChIP-seq
<input type="checkbox"/>	<input checked="" type="checkbox"/> Flow cytometry
<input checked="" type="checkbox"/>	<input type="checkbox"/> MRI-based neuroimaging

Antibodies

Antibodies used

Primary antibodies for tissue immunofluorescence/immunohistochemistry
 Mouse monoclonal anti-Cytokeratin 14 (1:1000, Abcam ab7800, clone LL002), rat monoclonal anti- Ki67 (1:200, eBioscience, 14-5698-82, clone SolA15), rabbit polyclonal anti-CD31 (1:50, Abcam ab28364), goat polyclonal anti-alpha smooth muscle actin (1:1000, Abcam ab21027) and rabbit monoclonal anti-active caspase-3 (1:40, BD, 559565, clone C92-605).

Secondary antibodies

All donkey, at 1:500 dilution: anti-mouse IgG H&L (Alexa Fluor 488, ab150109); anti-rat IgG H&L (Alexa Fluor 647, ab150155), anti-rabbit IgG H&L (Alexa Fluor 594, ab150064); anti-goat IgG H&L (Alexa Fluor 488, ab150133); anti-rabbit IgG H&L (Alexa Fluor 594, ab150064); anti-goat IgG H&L (Alexa Fluor 647, ab150131).

Flow-cytometry antibodies, all Biolegend

Rat monoclonal Alexa Fluor 700 anti-mouse CD45 Antibody (1:1000, Cat# 103128, clone 30-F11)
 Rat monoclonal APC/Cyanine7 anti-mouse/human CD11b Antibody (1:1000, Cat# 101226, clone M1/70)
 Rat monoclonal PerCP/Cyanine5.5 anti-mouse/human CD11b Antibody (1:500, Cat# 101228, clone M1/70)
 Rat monoclonal Brilliant Violet 605 anti-mouse F4/80 Antibody (1:200, Cat# 123133, clone BM8)
 Mouse monoclonal APC anti-mouse CD64 (FcγRI) Antibody (1:200, Cat# 139306, clone X54-5/7.1)
 Armenian hamster monoclonal FITC anti-mouse CD3ε Antibody (1:200, Cat# 100306, clone 145-2C11)
 Rat monoclonal PE/Cyanine7 anti-mouse CD4 Antibody (1:200, Cat# 116016, clone RM4-4)
 Rat monoclonal Brilliant Violet 650 anti-mouse CD8a Antibody (1:200, Cat# 100741, clone 53-6.7)
 Rat monoclonal APC/Cyanine7 anti-mouse Ly-6G Antibody (1:200, Cat# 127624, clone 1A8)
 Rat monoclonal Brilliant Violet 421 anti-mouse Ly-6C Antibody (1:200, Cat# 128031, clone HK1.4)
 Armenian hamster monoclonal PE anti-mouse CD11c Antibody (1:500, Cat# 117308, clone N418)
 Rat monoclonal Brilliant Violet 785 anti-mouse I-A/I-E Antibody (1:1000, Cat# 107645, clone M5/114.15.2)
 Armenian hamster monoclonal Brilliant Violet 421 anti-mouse CD80 Antibody (1:200, Cat# 104725, clone 16-10A1)
 Rat monoclonal FITC anti-mouse CD86 Antibody (1:200, Cat# 105006, clone GL-1)
 Rat monoclonal PerCP/Cyanine5.5 anti-mouse CD301b (MGL2) Antibody (1:100, Cat# 146810, clone URA-1)
 Rat monoclonal Brilliant Violet 650 anti-mouse CD206 (MMR) Antibody (1:200, Cat# 141723, clone C068C2)
 Rat monoclonal PE anti-mouse CD163 Antibody (1:300, Cat# 155308, clone S15049I)

Validation

All antibodies are commercially available and have been tested by the manufacturer. Vendors and catalogue numbers are listed above, and validation information can be found on the manufacturer's website:

<https://www.abcam.com/cytokeratin-14-antibody-ll002-ab7800.html>
<https://www.thermofisher.com/antibody/product/Ki-67-Antibody-clone-SolA15-Monoclonal/14-5698-82>
<https://www.abcam.com/cd31-antibody-ab28364.html>
<https://www.abcam.com/alpha-smooth-muscle-actin-antibody-ab21027.html>
<https://www.bdbiosciences.com/en-us/products/reagents/flow-cytometry-reagents/research-reagents/single-color-antibodies-ruo/purified-rabbit-anti-active-caspase-3.559565>

<https://www.abcam.com/donkey-mouse-igg-hl-alexa-fluor-488-preadsorbed-ab150109.html>
<https://www.abcam.com/donkey-rat-igg-hl-alexa-fluor-647-preadsorbed-ab150155.html>
<https://www.abcam.com/donkey-rabbit-igg-hl-alexa-fluor-594-preadsorbed-ab150064.html>
<https://www.abcam.com/donkey-goat-igg-hl-alexa-fluor-488-preadsorbed-ab150133.html>
<https://www.abcam.com/donkey-rabbit-igg-hl-alexa-fluor-594-preadsorbed-ab150064.html>
<https://www.abcam.com/donkey-goat-igg-hl-alexa-fluor-647-ab150131.html>

<https://www.biolegend.com/en-us/products/alexa-fluor-700-anti-mouse-cd45-antibody-3407>
<https://www.biolegend.com/en-us/products/apc-cyanine7-anti-mouse-human-cd11b-antibody-3930>
<https://www.biolegend.com/en-us/products/percp-cyanine5-5-anti-mouse-human-cd11b-antibody-4257>
<https://www.biolegend.com/en-us/products/brilliant-violet-605-anti-mouse-f4-80-antibody-8702>
<https://www.biolegend.com/en-us/products/apc-anti-mouse-cd64-fcγmari-antibody-7874>
<https://www.biolegend.com/en-us/products/fic-anti-mouse-cd3ε-antibody-23>
<https://www.biolegend.com/en-us/products/pe-cyanine7-anti-mouse-cd4-antibody-9321>
<https://www.biolegend.com/en-us/products/brilliant-violet-650-anti-mouse-cd8a-antibody-7635>
<https://www.biolegend.com/en-us/products/apc-cyanine7-anti-mouse-ly-6g-antibody-6755>
<https://www.biolegend.com/en-us/products/brilliant-violet-421-anti-mouse-ly-6c-antibody-8586>
<https://www.biolegend.com/en-us/products/pe-anti-mouse-cd11c-antibody-1816>
<https://www.biolegend.com/en-us/products/brilliant-violet-785-anti-mouse-i-a-i-e-antibody-12087>
<https://www.biolegend.com/en-us/products/brilliant-violet-421-anti-mouse-cd80-antibody-7357>
<https://www.biolegend.com/en-us/products/fic-anti-mouse-cd86-antibody-254>
<https://www.biolegend.com/en-us/products/percp-cyanine5-5-anti-mouse-cd301b-mgl2-antibody-9660>
<https://www.biolegend.com/en-us/products/brilliant-violet-650-anti-mouse-cd206-mmr-antibody-8842>
<https://www.biolegend.com/en-us/products/pe-anti-mouse-cd163-antibody-18223>

Eukaryotic cell lines

Policy information about [cell lines](#)

Cell line source(s)

NIH/3T3 (ATCC CRL-1658)

Authentication	NIH/3T3 cells from ATCC were authenticated by ATCC, on the basis of standard techniques including morphology check, isoenzyme analysis and mycoplasma detection.
Mycoplasma contamination	Mycoplasma contamination was not detected.
Commonly misidentified lines (See ICLAC register)	No commonly misidentified cell lines were used.

Animals and other organisms

Policy information about [studies involving animals](#); [ARRIVE guidelines](#) recommended for reporting animal research

Laboratory animals	<p>Female Sprague Dawley rats (12 weeks, 225–275 g) were purchased from Charles River Laboratories.</p> <p>Male db/db mice (strain # 000642, received at 10 weeks and wounded at 12 weeks, 47–53 g) and male nude mice (strain # 002019, received at 5 weeks, grafted at 6 weeks, STZ diabetes induction at 11 weeks, wounded when 18 weeks old; 27–30 g) were purchased from Jackson Laboratories.</p> <p>One male and one female miniature Yucatan diabetic pigs (wounded when 10 months old; a 23.7-kg male and a 24-kg female) were purchased from Sinclair Bio Resources.</p>
Wild animals	The study did not involve wild animals.
Field-collected samples	The study did not involve samples collected from the field.
Ethics oversight	Animal procedures for the rat experiments were reviewed and approved by the Massachusetts Institute of Technology Committee on Animal Care. Animal procedures for the experiments with db/db mice, nude mice and swine were reviewed and approved by the BIDMC Institutional Animal Care and Use Committee.

Note that full information on the approval of the study protocol must also be provided in the manuscript.

Flow Cytometry

Plots

Confirm that:

- ☒ The axis labels state the marker and fluorochrome used (e.g. CD4-FITC).
- ☒ The axis scales are clearly visible. Include numbers along axes only for bottom left plot of group (a 'group' is an analysis of identical markers).
- ☒ All plots are contour plots with outliers or pseudocolor plots.
- ☒ A numerical value for number of cells or percentage (with statistics) is provided.

Methodology

Sample preparation	Immediately following euthanasia, mouse skin comprising of wound and approximately 0.5 mm of peri-wound tissue was excised and kept on ice cold sterile PBS until processing within 2 h. Four wounds from two mice were pooled as one sample to ensure enough single cells. The skin was finely minced with a scalpel and placed for 30 min at 37 °C on a shaker in a digesting enzyme cocktail of 2 mg/ml Collagenase P (Roche), 2 mg/ml Dispase (Gibco) and 1 mg/ml DNase I (Stemcell Technologies) in DMEM (Gibco) with 10% FBS and 1% P/S, using glass pipettes to break down the extracellular matrix every 10 min. Single cell suspensions were passed through a 40 µm cell strainer, counted with a K2 cellometer (Nexcelom Bioscience) and cryopreserved in 90% FBS 10% dimethyl sulfoxide until processing.
Instrument	CytoFLEX LX flow cytometer (Beckman Coulter)
Software	CytExpert software (Beckman Coulter)
Cell population abundance	Cells were quickly thawed and adjusted to a concentration of 1 million cells / mL. A LIVE/DEAD fixable dead cell stain kit was used to exclude dead cells from the analysis (ThermoFisher). AbC total antibody and amine reactive ArC compensation beads kits (ThermoFisher, A10497 and A10346) were included for single stain controls. After completing the viability stain per the manufacturer's instructions, cells were blocked (Biolegend FACS buffer with 0.05% anti-mouse CD16/32 Biolegend, 101320 and 0.05% Tru-stain monocyte blocker Biolegend, 426103) for 10 min at RT.
Gating strategy	A forward and side scatter density plot was used for debris exclusion followed by a forward scatter area vs forward scatter height density plot for doublet exclusion. Live immune cells (CD45+) were then characterized as neutrophils, macrophages (and different subtypes), monocytes, monocyte-derived dendritic cells and T cells (and different subtypes) with appropriate cell-surface antibody staining and sequential gating. The gating strategy is illustrated in Supplementary Figs. 15 and 16.
<input checked="" type="checkbox"/> Tick this box to confirm that a figure exemplifying the gating strategy is provided in the Supplementary Information.	

Supplementary information

A strain-programmed patch for the healing of diabetic wounds

In the format provided by the
authors and unedited

Contents

Supplementary Methods

Supplementary Discussion 1 | Hydration-based shape-memory of the strain-programmed patch

Supplementary Discussion 2 | Rapid and on-demand detachable wet adhesion

Supplementary Discussion 3 | Modeling of wound contraction and stress remodeling

Supplementary References

Supplementary Fig. 1 | Mechanical properties of the strain-programmed patch

Supplementary Fig. 2 | Fabrication of the strain-programmed patch

Supplementary Fig. 3 | Swelling of the strain-programmed patch

Supplementary Fig. 4 | Comparison between Flory-Rehner and neo-Hookean models

Supplementary Fig. 5 | Long-term adhesion and wound contraction performance

Supplementary Fig. 6 | Fracture toughness of the strain-programmed patch

Supplementary Fig. 7 | Interfacial toughness between elastomer backing and bioadhesive in the strain-programmed patch

Supplementary Fig. 8 | Schematic configuration for the analytical modeling

Supplementary Fig. 9 | Comparison of analytical and finite-element analyses

Supplementary Fig. 10 | Finite-element modeling for wound closure by the strain-programmed patch

Supplementary Fig. 11 | Mechanical modulation of diabetic mouse skin wounds

Supplementary Fig. 12 | Strain-programmed patch for large diabetic wounds

Supplementary Fig. 13 | Skin wound healing in human, wild type rodent, and db/db mouse

Supplementary Fig. 14 | RT-qPCR gene expression analysis of diabetic mouse wound

Supplementary Fig. 15 | Gating strategy for the flow cytometry analysis of dissociated wound tissues

Supplementary Fig. 16 | Additional gating strategy for T-cell subsets and polarized macrophages

Supplementary Fig. 17 | Visualization of RNA sequencing results

Supplementary Fig. 18 | No strain vs TD differential expression and functional analyses

Supplementary Fig. 19 | Mouse wound bulk RNA-seq deconvolution using the GSE141814 scRNA-seq mouse dataset as reference

Supplementary Fig. 20 | Mechanical modulation of porcine skin wounds

Supplementary Fig. 21 | Different wound geometries

Supplementary Fig. 22 | RT-qPCR gene expression analysis of porcine wounds

Supplementary Fig. 23 | RT-qPCR gene expression analysis of humanized mouse wounds

Supplementary Fig. 24 | Spin-coating of backing layer

Supplementary Fig. 25 | Tensile properties of *ex vivo* human skin

Supplementary Data Captions

Supplementary Video Captions

Supplementary Methods

Mechanical characterization. Unless otherwise indicated, the strain-programmed patch ($\lambda_{\text{patch}}^{\text{pre}} = 1.3$) was applied after hydration of the tissue surfaces with PBS followed by 5 s pressing (with 1 kPa pressure applied by either mechanical testing machine or equivalent weight). Unless otherwise indicated, all mechanical tests on samples were performed 1 h after initial pressing to ensure equilibrium swelling of the adhered strain-programmed patch. The application of commercially-available tissue adhesives and wound dressings followed the manufacturer's manual for each product.

To measure interfacial toughness, adhered samples with widths of 2.5 cm were prepared and tested by the standard 180-degree peel test (ASTM F2256) using a mechanical testing machine (2.5-kN load-cell, Zwick/Roell Z2.5). All tests were conducted with a constant peeling speed of 50 mm min⁻¹. The measured force reached a plateau as the peeling process entered the steady-state. Interfacial toughness was determined by dividing two times the plateau force by the width of the tissue sample. Hydrophilic nylon filters (1 μm pore size, TISCH Scientific) were applied as a stiff backing for the strain-programmed patch. Poly(methyl methacrylate) (PMMA) films (with a thickness of 50 μm ; Goodfellow) were applied using cyanoacrylate glue (Krazy Glue) as a stiff backing for porcine skin tissues.

To measure shear strength, the adhered samples with an adhesion area of 2.5 cm in width and 1 cm in length were prepared and tested by the standard lap-shear test (ASTM F2255) with a mechanical testing machine (2.5-kN load-cell, Zwick/Roell Z2.5). All tests were conducted with a constant tensile speed of 50 mm min⁻¹. Shear strength was determined by dividing the maximum force by the adhesion area. Hydrophilic nylon filters were applied as a stiff backing for the strain-programmed patch. PMMA films were applied using cyanoacrylate glue (Krazy Glue) as a stiff backing for porcine skin tissues.

To measure wound closure strength, the adhered samples with 2.5 cm in width and 1 cm in overlap length (between adhesive and tissue) were prepared and tested by the standard wound closure strength test (ASTM F2458-05) with a mechanical testing machine (2.5-kN load-cell, Zwick/Roell Z2.5). All tests were conducted with a constant tensile speed of 50 mm min⁻¹. Wound closure strength was determined by measuring the maximum force.

The tensile properties and fracture toughness of the strain-programmed patch were measured using pure-shear tensile tests of thin rectangular samples (10 mm in length, 30 mm in width, and 0.5 mm in thickness) with a mechanical testing machine (20-N load-cell, Zwick/Roell Z2.5). All tests were conducted with a constant tensile speed of 50 mm min⁻¹. The fracture toughness of the strain-programmed patch was calculated by following the previously reported method based on tensile tests of unnotched and notched samples (Supplementary Fig. 6).

The tensile properties of db/db mouse skin, porcine skin, and human skin were measured with a mechanical testing machine (2.5-kN load-cell, Zwick/Roell Z2.5). All tests were conducted with a constant tensile speed of 50 mm min⁻¹. The nominal stress vs stretch curves of skin were fitted with the incompressible Ogden hyperelastic model as

$$s = \frac{2\mu}{\alpha\lambda} \left(\lambda^\alpha - \lambda^{-\frac{1}{2}\alpha} \right)$$

where s is nominal stress (i.e., the measured force divided by the cross-sectional area of an undeformed sample), μ is shear modulus, and α is Ogden coefficient. For db/db mouse skin, $\mu_{\text{mouse}} = 25$ kPa and $\alpha_{\text{mouse}} = 7$. For porcine skin, $\mu_{\text{pig}} = 57$ kPa and $\alpha_{\text{pig}} = 8$. For human skin, $\mu_{\text{human}} = 40$ kPa and $\alpha_{\text{human}} = 20$ (Supplementary Fig. 25).

In vitro biocompatibility study. *In vitro* biocompatibility tests were conducted by using the strain-programmed patch-conditioned media for cell culture. To prepare the strain-programmed patch-conditioned media for *in vitro* biocompatibility tests, 20 mg of the swollen strain-programmed patch was incubated in 1 mL Dulbecco's modified eagle medium (DMEM) at 37 °C for 24 h. The pristine DMEM was used as a control. Wild-type mouse embryonic fibroblasts (NIH/3T3, ATCC CRL-1658) were plated in 96-well plate ($N = 6$ per each group). The cells were then treated with the strain-programmed patch-conditioned media and incubated at 37 °C for 24 h in 5 % CO₂. The cell viability was determined with a LIVE/DEAD viability/cytotoxicity kit for mammalian cells (Thermo Fisher Scientific) by adding 4 μM calcein and ethidium homodimer-1 into the culture media. A confocal microscope (SP 8, Leica) was used to image live cells with excitation/emission at 495nm/515nm, and dead cells at 495nm/635nm, respectively. The cell viability was calculated by counting live (green fluorescence) and dead (red fluorescence) cells by using ImageJ (version 2.1.0).

***In vivo* biocompatibility study.** All animal surgeries for *in vivo* biocompatibility study were reviewed and approved by the Committee on Animal Care at the Massachusetts Institute of Technology. Female Sprague Dawley rats (12 weeks, 225-250 g, Charles River Laboratories) were used. Before implantation, the strain-programmed patch was prepared using aseptic techniques and was further sterilized for 3 h under UV light. For implantation in the dorsal subcutaneous space, rats were anesthetized using isoflurane (1–2% isoflurane in oxygen) in an anesthetizing chamber. Anesthesia was maintained using a nose cone. The back hair was removed and the animals were placed over a heating pad for the duration of the surgery. The subcutaneous space was accessed by a 1-2 cm skin incision per implant in the center of the animal's back. To create space for implant placement, blunt dissection was performed from the incision towards the animal shoulder blades. For the sham surgery group, no implant was placed in the subcutaneous pocket ($n = 4$). For the on-demand detachment group, the strain-programmed patch (10 mm in width and 20 mm in length) was placed in the subcutaneous pocket and detached 5 min by applying 1 mL of the detachment solution ($n = 4$). For the patch group, the strain-programmed patch (10 mm in width and 20 mm in length) was placed in the subcutaneous pocket without detachment ($n = 4$). For commercially-available tissue adhesive groups, 0.5 mL of Coseal ($n = 4$) and Dermabond cyanoacrylate adhesive ($n = 4$) were injected in the subcutaneous pocket. The incision was closed using interrupted sutures (4-0 Vicryl, Ethicon) and 3-6 mL of saline were injected subcutaneously. Up to four implants were placed per animal ensuring no overlap between subcutaneous pockets. After 2 weeks following the implantation, the animals were euthanized by CO₂ inhalation. Subcutaneous regions of interest were excised and fixed in 10 % formalin for 24 h for histological analyses.

Fixed tissue samples were placed into 70 % ethanol and submitted for histological processing and hematoxylin and eosin (H&E) staining at the Hope Babette Tang (1983) Histology Facility in the Koch Institute for Integrative Cancer Research at the Massachusetts Institute of Technology. Histological assessment was performed by a blinded pathologist on a scale of 0-4 (0, normal; 1, mild; 2, moderate; 3, severe; 4, very severe) to evaluate the degree of inflammation in the tissues surrounding the subcutaneous implants. Representative images of each group were shown in the corresponding figures.

Digital image correlation analysis. Random speckles were applied on *ex vivo* human skin by using a black spray painter to provide tracking markers for digital image correlation (DIC) analysis. The speckled skin sample was photographed from top view before and after applying pre-strain. The images were analyzed by a commercial DIC software package (Vic-2D 2009, Correlated Solutions, Inc.) to generate engineering strain maps in x- and y-directions.

Supplementary Discussion 1 | Hydration-based shape-memory of the strain-programmed patch

To achieve desirable contraction and stress remodeling of wet wounded tissues, we develop a hydration-based shape-memory mechanism and an associated theoretical framework for predictable and reproducible fabrication for the strain-programmed patch. In the following paragraphs, we will discuss (i) a physical picture of the proposed hydration-based shape-memory mechanism, (ii) fabrication of the strain-programmed patch, and (iii) mechanical properties of the strain-programmed patch.

1. Hydration-based shape-memory mechanism

Shape-memory polymers are the class of polymers capable of memorizing a certain macroscopic deformed configuration in the stable fixed state and relaxing to the original undeformed configuration under external stimuli¹⁻³. The transition from the fixed deformed configuration to the relaxed original configuration relies on a drastic mechanical property change between the glassy fixed state and the rubbery relaxed state¹⁻³. In the glassy state, polymer chains in the shape-memory polymers are “frozen” with suppressed mobility and high macroscopic stiffness (i.e., high Young’s modulus). In the rubbery state, polymer chains in the shape-memory polymers recover their entropic elasticity with low macroscopic stiffness (i.e., low Young’s modulus) where the memorized deformation in the fixed glassy state can be elastically relaxed. The glassy to rubbery state transition in shape-memory polymers are conventionally achieved by tuning environmental temperature across the transition temperature (T_{trans}) where the shape-memory polymers are in the glassy state in low temperature ($T < T_{\text{trans}}$) and in the rubbery state in high temperature ($T > T_{\text{trans}}$), respectively¹⁻⁴. T_{trans} is a critical temperature where the chain mobility of the shape-memory polymers changes drastically, which can be either the glass transition temperature (T_g) for amorphous polymers or the melting temperature (T_m) for crystalline polymers.

In this work, we propose a non-thermal hydration-based shape-memory mechanism without the need of changing environmental temperature to achieve predictable and facile contraction and mechanical modulations of wet wounded tissues in synergistic combination with the dry-crosslinking mechanism for rapid robust wet adhesion^{5,6}. The hydration-based shape-memory mechanism relies on the hydrogels’ unique transition between the glassy state and the rubbery state based on hydration level. In hydrated or swollen state, hydrogels are elastically deformable solids in the rubbery state with low macroscopic stiffness (i.e., low Young’s modulus). However, when hydrogels are dried to remove water, hydrogels transit into the glassy state whose polymer chains are frozen with suppressed mobility and high macroscopic stiffness (i.e., high Young’s modulus), providing ability to stably fix or memorize the deformed configuration and program the applied pre-stretches. By re-hydrating the dried hydrogels, hydrogels can recover their soft and elastic properties in the rubbery state during which the programmed pre-stretches can be elastically relaxed (Fig. 2a).

This hydration-based transition between the glassy and rubber states is due to the reduction of polymer network’s T_g during hydration. A simplified expression for T_g is provided as^{7,8}

$$T_g = \frac{\alpha_1 \phi_1 T_{g1} + \alpha_2 \phi_2 T_{g2}}{\alpha_1 \phi_1 + \alpha_2 \phi_2} \quad (\text{S1})$$

where α_1 and α_2 are the thermal expansion coefficients of the polymer and the solvent, and ϕ_1 and ϕ_2 are the volume fraction of the polymer and solvent, T_{g1} and T_{g2} are the glass transition temperature of the polymer and the melting point of the solvent, respectively. The melting point T_{g2} of water is much lower than the glass transition temperature T_{g1} of typical polymers for hydrogels. Notably, the time required to fully hydrate a hydrogel with a thickness of H can be expressed as $t_{\text{hydrate}} = (H/k_h)^2$ where k_h is the hydration coefficient of the hydrogel⁶.

Hence, the proposed hydration-based shape-memory mechanism provides a facile and effective strain-programming and -release strategy for hydrogels, including the bioadhesive layer of the strain-programmed patch, only by natively present water in wet physiological environment without the need of thermal or other complex external stimuli. The hydration-based shape-memory mechanism’s highly versatile and tunable strain-programming capability and water-based biocompatible triggering of the programmed strain release are particularly advantageous for biomedical and clinical applications operating in wet physiological environments.

2. Fabrication of the strain-programmed patch

Taking advantage of the hydration-based shape-memory mechanism, the strain-programmed patch can be fabricated based on multiple steps of pre-stretching and drying processes as summarized in Supplementary Fig. 2. Since the non-adhesive elastomer backing and the bioadhesive layer in the strain-programmed patch can have different swelling ratio in wet physiological environments (Supplementary Fig. 3), the fabrication process of the strain-programmed patch involves canceling of swelling mismatch between the two layers as well as swelling of the assembled patch.

The fabrication of the strain-programmed patch starts from the as-prepared bioadhesive in the rubbery state with the dimension of $\lambda_{\text{adhesive}}^0$ ($=1.48$ for the bioadhesive used in this work) in length and width and $H_{\text{adhesive}}\lambda_{\text{adhesive}}^0$ in thickness where the reference state (i.e., isotropically dried bioadhesive) has the dimension of H_{adhesive} in thickness and unity in length and width. The fabrication process consists of five distinctive steps as the following:

Step 1. Introduce the non-adhesive elastomer backing resin (i.e., before curing) on the as-prepared bioadhesive layer, and pre-stretch the bioadhesive layer by ratio of

$$\lambda_{\text{adhesive}}^{\text{pre}} = \frac{\lambda_{\text{adhesive}}^{\infty}}{\lambda_{\text{adhesive}}^0 \lambda_{\text{backing}}^{\infty}} \quad (\text{S2})$$

in both directions to cancel out the swelling mismatch between the non-adhesive elastomer backing and the bioadhesive layer (Step 1 in Supplementary Fig. 2), where $\lambda_{\text{adhesive}}^{\infty}$ is the equilibrium swelling ratio of the bioadhesive layer and $\lambda_{\text{backing}}^{\infty}$ is the equilibrium swelling ratio of the non-adhesive elastomer backing. For the bioadhesive and the elastomer backing used in this work, $\lambda_{\text{adhesive}}^{\infty} = 3.46$ and $\lambda_{\text{backing}}^{\infty} = 1.4$ which give $\lambda_{\text{adhesive}}^{\text{pre}} = 1.665$ (Supplementary Fig. 3).

After this step, the bioadhesive layer in the rubbery state has the dimension of $\lambda_{\text{adhesive}}^0 \lambda_{\text{adhesive}}^{\text{pre}}$ in length and width and $(H_{\text{adhesive}}\lambda_{\text{adhesive}}^0)(\lambda_{\text{adhesive}}^{\text{pre}})^{-2}$ in thickness.

Step 2. Cure the non-adhesive elastomer backing on the pre-stretched bioadhesive layer (Step 2 in Supplementary Fig. 2).

After this step, the non-adhesive elastomer backing in the rubbery state has the dimension of $\lambda_{\text{adhesive}}^0 \lambda_{\text{adhesive}}^{\text{pre}}$ in length and width and H_{backing} in thickness; the bioadhesive layer in the rubbery state has the dimension of $\lambda_{\text{adhesive}}^0 \lambda_{\text{adhesive}}^{\text{pre}}$ in length and width and $(H_{\text{adhesive}}\lambda_{\text{adhesive}}^0)(\lambda_{\text{adhesive}}^{\text{pre}})^{-2}$ in thickness.

Step 3. Pre-stretch both non-adhesive elastomer backing and bioadhesive layer by ratio of

$$\lambda_{\text{backing}}^{\text{pre}} = \lambda_{\text{backing}}^{\infty} \quad (\text{S3})$$

in both directions to cancel out the dimensional change of the patch by swelling in wet physiological environments (Step 3 in Supplementary Fig. 2).

After this step, the non-adhesive elastomer backing in the rubbery state has the dimension of $\lambda_{\text{adhesive}}^0 \lambda_{\text{adhesive}}^{\text{pre}} \lambda_{\text{backing}}^{\text{pre}}$ in length and width and $(H_{\text{backing}})(\lambda_{\text{backing}}^{\text{pre}})^{-2}$ in thickness; the bioadhesive layer in the rubbery state has the dimension of $\lambda_{\text{adhesive}}^0 \lambda_{\text{adhesive}}^{\text{pre}} \lambda_{\text{backing}}^{\text{pre}}$ in length and width and $(H_{\text{adhesive}}\lambda_{\text{adhesive}}^0)(\lambda_{\text{adhesive}}^{\text{pre}} \lambda_{\text{backing}}^{\text{pre}})^{-2}$ in thickness.

Step 4. Pre-stretch both non-adhesive elastomer backing and bioadhesive layer by ratios of $\lambda_{\text{patch}}^{\text{pre1}}$ and $\lambda_{\text{patch}}^{\text{pre2}}$ to each direction to program desired strains (direction 1 in length, direction 2 in width), respectively (Step 4 in Supplementary Fig. 2).

After this step, the non-adhesive elastomer backing in the rubbery state has the dimension of $\lambda_{\text{adhesive}}^0 \lambda_{\text{adhesive}}^{\text{pre}} \lambda_{\text{backing}}^{\text{pre}} \lambda_{\text{patch}}^{\text{pre1}}$ in length, $\lambda_{\text{adhesive}}^0 \lambda_{\text{adhesive}}^{\text{pre}} \lambda_{\text{backing}}^{\text{pre}} \lambda_{\text{patch}}^{\text{pre2}}$ in width, and $(H_{\text{backing}}) \left((\lambda_{\text{backing}}^{\text{pre}})^2 \lambda_{\text{patch}}^{\text{pre1}} \lambda_{\text{patch}}^{\text{pre2}} \right)^{-1}$ in thickness; the bioadhesive layer in the rubbery state has the

dimension of $\lambda_{\text{adhesive}}^0 \lambda_{\text{adhesive}}^{\text{pre}} \lambda_{\text{backing}}^{\text{pre}} \lambda_{\text{patch}}^{\text{pre1}}$ in length, $\lambda_{\text{adhesive}}^0 \lambda_{\text{adhesive}}^{\text{pre}} \lambda_{\text{backing}}^{\text{pre}} \lambda_{\text{patch}}^{\text{pre2}}$ in width, and $(H_{\text{adhesive}} \lambda_{\text{adhesive}}^0) \left((\lambda_{\text{adhesive}}^{\text{pre}} \lambda_{\text{backing}}^{\text{pre}})^2 \lambda_{\text{patch}}^{\text{pre1}} \lambda_{\text{patch}}^{\text{pre2}} \right)^{-1}$ in thickness.

Step 5. Dry the assembled strain-programmed patch to shape-memory the pre-stretched configuration (Step 5 in Supplementary Fig. 2), completing the fabrication of the strain-programmed patch.

After this step, the non-adhesive elastomer backing in the rubbery state has the dimension of $\lambda_{\text{adhesive}}^0 \lambda_{\text{adhesive}}^{\text{pre}} \lambda_{\text{backing}}^{\text{pre}} \lambda_{\text{patch}}^{\text{pre1}}$ in length, $\lambda_{\text{adhesive}}^0 \lambda_{\text{adhesive}}^{\text{pre}} \lambda_{\text{backing}}^{\text{pre}} \lambda_{\text{patch}}^{\text{pre2}}$ in width, and $(H_{\text{backing}}) \left((\lambda_{\text{backing}}^{\text{pre}})^2 \lambda_{\text{patch}}^{\text{pre1}} \lambda_{\text{patch}}^{\text{pre2}} \right)^{-1}$ in thickness; the bioadhesive layer in the glassy state has the dimension of $\lambda_{\text{adhesive}}^0 \lambda_{\text{adhesive}}^{\text{pre}} \lambda_{\text{backing}}^{\text{pre}} \lambda_{\text{patch}}^{\text{pre1}}$ in length, $\lambda_{\text{adhesive}}^0 \lambda_{\text{adhesive}}^{\text{pre}} \lambda_{\text{backing}}^{\text{pre}} \lambda_{\text{patch}}^{\text{pre2}}$ in width, and $(H_{\text{adhesive}}) \left((\lambda_{\text{adhesive}}^0 \lambda_{\text{adhesive}}^{\text{pre}} \lambda_{\text{backing}}^{\text{pre}})^2 \lambda_{\text{patch}}^{\text{pre1}} \lambda_{\text{patch}}^{\text{pre2}} \right)^{-1}$ in thickness.

3. Mechanical properties of the strain-programmed patch

3.1. Measurement of physical parameters of the strain-programmed patch

Since both non-adhesive elastomer backing and bioadhesive layer of the strain-programmed patch used in this work become hydrogel in wet physiological environments, we take the swollen strain-programmed patch as a Flory-Rehner hydrogel with thermodynamic parameters of N_{adhesive} , N_{backing} , χ_{adhesive} , and χ_{backing} for simplicity of the analysis, where N_{adhesive} is the number of polymer chains per unit volume of the bioadhesive at the reference state (Supplementary Fig. 2), N_{backing} is the number of polymer chains per unit volume of the elastomer backing at the reference state (Supplementary Fig. 2), χ_{adhesive} is the Flory solvent-polymer interaction parameter for the bioadhesive, and χ_{backing} is the Flory solvent-polymer interaction parameter for the elastomer backing^{9,10}.

To determine N_{adhesive} , the shear modulus μ_{adhesive}^0 is measured for the as-prepared bioadhesive and N_{adhesive} is then calculated from¹¹

$$\mu_{\text{adhesive}}^0 = \frac{1}{\lambda_{\text{adhesive}}^0} N_{\text{adhesive}} kT \quad (\text{S4})$$

where k is the Boltzmann constant, T is the absolute temperature. To measure χ_{adhesive} , we carry out free-swelling experiment for the as-prepared bioadhesive without constraint (i.e., freely swelling in PBS). The Cauchy stress $\sigma_{\text{eq,adhesive}}$ in any direction of the unconstrained equilibrium swollen bioadhesive can be expressed as¹¹

$$\sigma_{\text{eq,adhesive}} = N_{\text{adhesive}} kT (\lambda_{\text{adhesive}}^{\infty -1} - \lambda_{\text{adhesive}}^{\infty -3}) + \frac{kT}{\nu} [\ln(1 - \lambda_{\text{adhesive}}^{\infty -3}) + \lambda_{\text{adhesive}}^{\infty -3} + \chi_{\text{adhesive}} \lambda_{\text{adhesive}}^{\infty -6}] \quad (\text{S5})$$

where ν is the volume of the water molecule. Due to the traction-free boundary condition, the Cauchy stress $\sigma_{\text{eq,adhesive}}$ is zero in Eq. (S5). In this study, we used $T = 310$ K (i.e., body temperature), $\nu = 3.0 \times 10^{-29} \text{ m}^3$ and experimentally-measured values of $\mu_{\text{adhesive}}^0 = 45 \text{ kPa}$, $\lambda_{\text{adhesive}}^0 = 1.48$, and $\lambda_{\text{adhesive}}^{\infty} = 3.46$. By implementing these values and solving Eq. (S5), we can calculate $N_{\text{adhesive}} = 1.56 \times 10^{25} \text{ m}^{-3}$ and $\chi_{\text{adhesive}} = 0.29$.

Similarly, to determine N_{backing} , the shear modulus $\mu_{\text{backing}}^{\infty}$ is measured for the equilibrium swollen elastomer backing and N_{backing} is then calculated from¹¹

$$\mu_{\text{backing}}^{\infty} = \frac{1}{\lambda_{\text{backing}}^{\infty}} N_{\text{backing}} kT \quad (\text{S6})$$

To measure χ_{backing} , we carry out free-swelling experiment for the elastomer backing without constraint (i.e., freely swelling in PBS). The Cauchy stress $\sigma_{\text{eq,backing}}$ in any direction of the unconstrained equilibrium swollen elastomer backing can be expressed as¹¹

$$\sigma_{\text{eq,backing}} = N_{\text{backing}} kT (\lambda_{\text{backing}}^{\infty -1} - \lambda_{\text{backing}}^{\infty -3}) + \frac{kT}{\nu} [\ln(1 - \lambda_{\text{backing}}^{\infty -3}) + \lambda_{\text{backing}}^{\infty -3} + \chi_{\text{backing}} \lambda_{\text{backing}}^{\infty -6}] \quad (\text{S7})$$

Due to the traction-free boundary condition, the Cauchy stress $\sigma_{\text{eq,backing}}$ is zero in Eq. (S7). In this study, we used $T = 310$ K (i.e., body temperature), $\nu = 3.0 \times 10^{-29} \text{ m}^3$ and experimentally-measured values of $G_{\text{backing}}^{\infty} = 720 \text{ kPa}$ and $\lambda_{\text{backing}}^{\infty} = 1.4$. By implementing these values and solving Eq. (S7), we can calculate $N_{\text{backing}} = 2.36 \times 10^{26} \text{ m}^{-3}$ and $\chi_{\text{backing}} = 0.65$.

3.2. Flory-Rehner model of the strain-programmed patch

In the equilibrium swollen state, the Cauchy stresses (or true stresses) generated by the bioadhesive layer σ_{adhesive} and the elastomer backing σ_{backing} can be expressed as^{11,12}

$$\begin{aligned}\sigma_{\text{adhesive},i} &= \frac{N_{\text{adhesive}}kT}{J_{\text{adhesive}}}(\lambda_{\text{adhesive},i}^2 - 1) + \frac{kT}{\nu} \left(\ln \frac{J_{\text{adhesive}} - 1}{J_{\text{adhesive}}} + \frac{1}{J_{\text{adhesive}}} + \frac{\chi_{\text{adhesive}}}{J_{\text{adhesive}}^2} \right) \\ \sigma_{\text{backing},i} &= \frac{N_{\text{backing}}kT}{J_{\text{backing}}}(\lambda_{\text{backing},i}^2 - 1) + \frac{kT}{\nu} \left(\ln \frac{J_{\text{backing}} - 1}{J_{\text{backing}}} + \frac{1}{J_{\text{backing}}} + \frac{\chi_{\text{backing}}}{J_{\text{backing}}^2} \right)\end{aligned}\quad (\text{S8})$$

where σ_i is the Cauchy stress for each principal direction ($i = 1$ for length, 2 for width, and 3 for thickness direction, respectively), λ_i is the stretch from the reference state for each principal direction ($i = 1$ for length, 2 for width, and 3 for thickness direction, respectively), $J_{\text{adhesive}} = \lambda_{\text{adhesive},1}\lambda_{\text{adhesive},2}\lambda_{\text{adhesive},3}$, and $J_{\text{backing}} = \lambda_{\text{backing},1}\lambda_{\text{backing},2}\lambda_{\text{backing},3}$.

Since the strain-programmed patch consists of the elastomer backing and the bioadhesive layer, the overall Cauchy stress generated by the strain-programmable patch in equilibrium swollen state can be expressed as

$$\sigma_{\text{patch},i} = \gamma_{\text{backing}}\sigma_{\text{backing},i} + (1 - \gamma_{\text{backing}})\sigma_{\text{adhesive},i} \quad (\text{S9})$$

where γ_{backing} is the ratio of the elastomer backing thickness in the total thickness of the equilibrium swollen strain-programmed patch which can be calculated as

$$\gamma_{\text{backing}} = \frac{H_{\text{backing}}\lambda_{\text{backing}}^{\infty}}{H_{\text{adhesive}}\lambda_{\text{adhesive}}^{\infty} + H_{\text{backing}}\lambda_{\text{backing}}^{\infty}} \quad (\text{S10})$$

where H_{backing} and H_{adhesive} are thicknesses of the elastomer backing and the bioadhesive at the reference state, respectively (Supplementary Fig. 2).

3.3. Neo-Hookean model approximation of the strain-programmed patch

While we model the strain-programmed patch in equilibrium swollen state as a Flory-Rehner hydrogel, we also investigate approximation of the strain-programmed patch as an incompressible neo-Hookean solid¹³ for simplicity of the analysis, particularly in finite-element modeling. To obtain shear moduli of materials for incompressible neo-Hookean models, we first fit the uniaxial tensile test data of the elastomer backing, the bioadhesive layer, and the strain-programmed patch in equilibrium swollen state by using the following expression

$$S = \mu \left(\lambda - \frac{1}{\lambda^2} \right) \quad (\text{S11})$$

where S is the nominal or engineering stress, μ is the shear modulus, and λ is the stretch of sample in tensile tests. As a result, we obtain shear moduli of the elastomer backing $\mu_{\text{backing}}^{\infty} = 720$ kPa, the bioadhesive layer $\mu_{\text{adhesive}}^{\infty} = 13$ kPa, and the strain-programmed patch $\mu_{\text{patch}}^{\infty} = 17.2$ kPa in equilibrium swollen state, respectively (Supplementary Fig. 1).

As illustrated in Supplementary Fig. 4, the Flory-Rehner model and the incompressible neo-Hookean model show good agreement for the equilibrium swollen strain-programmed patch. This indicates that the simpler incompressible neo-Hookean model can be used to describe the mechanical behavior of the strain-programmed patch.

Supplementary Discussion 2 | Rapid and on-demand detachable wet adhesion

1. Dry-crosslinking mechanism

Unlike healthy skin in dry environment, wounded skin especially with chronic wounds such as DFU is inherently wet due to exposed wound bed and wound exudate. Due to hydrophilicity of biological tissues, such wet tissue surface results in a thin interfacial water layer when it contacts with countersurface^{14,15}. This interfacial water layer at the tissue-wound dressing interface interferes with adhesion of conventional wound dressings (e.g., Tegaderm) by preventing physical contact and subsequent adhesion (e.g., van der Waals interactions) of their pressure-sensitive adhesives. Hence, it is critical to overcome the interfacial water layer to provide rapid, robust, and stable adhesion to wet wounded tissues required for the proposed programmed mechanical modulation of wounds.

Recently, we have developed bioadhesives capable of forming rapid and robust adhesion to wet tissues and organs within few seconds based on the dry-crosslinking mechanism^{5,6,16}. As this capability is highly favorable in synergistic combination with the hydration-based shape-memory mechanism, we adopt and implement the dry-crosslinking mechanism for the strain-programmed patch in this work. The dry-crosslinking mechanism provides rapid wet adhesion based on two key processes. First, the dry and highly hydrophilic bioadhesive rapidly absorbs interfacial water at the bioadhesive-tissue interface by coupled hydration of and water diffusion to the dry bioadhesive⁶, removing the interfacial water layer and facilitating physical contact of the bioadhesive to the tissue surface (Extended Data Fig. 1a). Subsequently, the hydrated bioadhesive forms physical crosslinks (i.e., hydrogen bonds, electrostatic interactions) and covalent crosslinks (i.e., amide bonds) to the tissue surface (Extended Data Fig. 1b). After these processes, the bioadhesive becomes a robustly adhered hydrogel on the tissue surface.

To implement the dry-crosslinking mechanism, we choose crosslinked networks of poly(acrylic acid) grafted with *N*-hydroxysuccinimide ester (PAA-NHS ester) and chitosan⁵. Highly hydrophilic poly(acrylic acid) and chitosan networks facilitate rapid removal of the interfacial water layer by the dry bioadhesive while providing mechanical robustness of the hydrated bioadhesive⁵. Carboxylic acid groups and NHS ester groups in PAA-NHS ester network provide physical crosslinks and covalent crosslinks to the tissue surface, respectively⁵ (Extended Data Fig. 1b).

2. On-demand detachment of the adhered strain-programmed patch

As we discussed in our recent work¹⁶, an adhered bioadhesive can be atraumatically detached on-demand by cleaving its crosslinks with the tissue surface (Extended Data Fig. 1a). As on-demand detachment of adhered wound dressing can be a beneficial feature for the strain-programmed patch for diabetic wound treatment, we also incorporate the on-demand detachment capability in this work.

The strain-programmed patch adheres with the tissue surface based on physical (i.e., hydrogen bonds, electrostatic interactions) and covalent (i.e., amide bonds) crosslinks at the interface (Extended Data Fig. 1b). Hence, on-demand detachment of the strain-programmed patch requires cleavage of both types of crosslinks. Following the previously reported method from our team¹⁶, we choose a biocompatible aqueous solution based on sodium bicarbonate and L-glutathione reduced to achieve on-demand cleavage and subsequent detachment of the strain-programmed patch. Sodium bicarbonate in the detachment solution cleaves physical crosslinks between the strain-programmed patch and the tissue surface by neutralizing and inactivating carboxylic acid groups (Extended Data Fig. 1c, left). L-glutathione reduced in the detachment solution cleaves covalent crosslinks between the strain-programmed patch and the tissue surface by reducing disulfide links (between the bioadhesive and the amide bond to the tissue) into thiols (Extended Data Fig. 1c, right).

Supplementary Discussion 3 | Modeling of wound contraction and stress remodeling

To provide quantitative and predictive design framework for contraction and stress remodeling of skin wounds by the strain-programmed patch, we develop analytical and finite-element models based on mechanical properties of the strain-programmed patch and tissues. In this study, without loss of generality, our models are developed based on a circular wound in the skin which is a common form for clinical diabetic wounds and an equibiaxially strain-programmed patch (i.e., $\lambda_{\text{patch}}^{\text{pre1}} = \lambda_{\text{patch}}^{\text{pre2}} = \lambda_{\text{patch}}^{\text{pre}}$).

1. Analytical modeling

1.1. Initial enlarging of wound by pre-strain in native skin

A skin wound with the initial radius denoted as a enlarges to a_1 immediately after wounding due to the relaxation of the pretension σ_∞ around the wound edge generated by the pre-strain in native skin. The reference state refers to an imaginary stress-free state in which $a_0 = a(\lambda_{\text{skin}}^{\text{pre}})^{-1}$ where $\lambda_{\text{skin}}^{\text{pre}} = 1.035$ is the experimentally measured pre-strain within the native skin. When the strain-programmed patch is applied to the wounded skin, the wound shrinks to radius a_{closure} (Supplementary Fig. 8). Axisymmetric condition is adopted for both skin and patch for equibiaxial scenario and the outer boundary of skin is assumed to be much larger than the wound (i.e., $c_0 = c(\lambda_{\text{skin}}^{\text{pre}})^{-1} \gg a_0$).

The strain-programmed patch initially has a radius of b_0 and undergoes an equibiaxial stretch of $\lambda_{\text{patch}}^{\text{pre}}$. For an incompressible neo-Hookean material under equibiaxial stretch, the Cauchy stresses are calculated as

$$\sigma_{r,\text{patch}} = \sigma_{\theta,\text{patch}} = \mu_{\text{patch}}^\infty \left(\lambda_{\text{patch}}^{\text{pre}^2} - \frac{1}{\lambda_{\text{patch}}^{\text{pre}^4}} \right) \quad (\text{S12})$$

where $\mu_{\text{patch}}^\infty$ is the shear modulus of the strain-programmed patch in equilibrium swollen state. The skin is modeled as an incompressible Ogden material and the pretension in the skin before wounding can be found as

$$\sigma_\infty = \frac{2\mu_{\text{skin}}}{\alpha} \left(\lambda_{\text{skin}}^{\text{pre}^\alpha} - \frac{1}{\lambda_{\text{skin}}^{\text{pre}^{2\alpha}} \right) \quad (\text{S13})$$

where $\mu_{\text{skin}} = 40$ kPa and $\alpha = 20$ (for human skin) are fitting parameters measured from experiment. By plugging $\lambda_{\text{skin}}^{\text{pre}} = 1.035$ into Eq. (S13), one can calculate that $\sigma_\infty = 0.17\mu_{\text{skin}}$.

Next, we can solve the wound radius a_1 immediately after wounding of the skin. Consider an arbitrary circle with radius $R \geq a_0$ in the reference state and moves to r in the deformed configuration. The incompressibility requires

$$\lambda_z(r^2 - a_1^2) = R^2 - a_0^2 \quad (\text{S14})$$

where λ_z is the stretch in z-direction. Then

$$r = a_0 \lambda_\theta \sqrt{\frac{\lambda_{\theta|a_0}^2 \lambda_z - 1}{\lambda_\theta^2 \lambda_z - 1}} \quad (\text{S15})$$

where hoop stretch $\lambda_\theta = r/R$ and $\lambda_{\theta|a_0} = a_1/a_0$ is the hoop stretch at the wound boundary $R = a_0$ and $\lambda_r \lambda_\theta \lambda_z = 1$. The equilibrium equation in current configuration can be expressed as

$$\frac{\partial \sigma_r}{\partial r} + \frac{\sigma_r - \sigma_\theta}{r} = 0 \quad (\text{S16})$$

To solve this, we can change variable from r to λ_θ . With Eq. (S16), we have

$$\frac{\partial \sigma_r}{\partial r} dr = -\frac{\sigma_r - \sigma_\theta}{r} dr = -\frac{2\mu_{skin}}{\alpha \lambda_\theta} \left(\frac{1}{\lambda_z \lambda_\theta} \right)^\alpha \frac{1 - \lambda_z^\alpha \lambda_\theta^{2\alpha}}{1 - \lambda_z \lambda_\theta^2} d\lambda_\theta \quad (S17)$$

By integrating Eq. (S17) from $r = a$ to arbitrary $r > a_1$, we obtain

$$\sigma_{rr} - \sigma_{rr}|_{r=a_1} = \phi(\lambda_z, \lambda_\theta) - \phi(\lambda_z, \lambda_{\theta|a_0}) \quad (S18)$$

where $\phi(\lambda_z, \lambda_\theta)$ is analytical function of $\lambda_z, \lambda_\theta$ and $\lambda_{\theta|a_0}$ is the hoop stretch at $r = a_0$. Due to the lengthy expression, we do not provide the complete form of $\phi(\lambda_z, \lambda_\theta)$ here. By invoking the boundary conditions at $r = a_1$, $\sigma_{rr}|_{r=a_1} = 0$, and at $r = c_1$, $\sigma_{rr}|_{r=c_1} = \sigma_\infty$, one can have

$$\sigma_\infty = \phi(\lambda_z, \lambda_{\theta|c_0}) - \phi(\lambda_z, \lambda_{\theta|a_0}) \quad (S19)$$

where $\lambda_{\theta|c_0}$ is the hoop stretch at $r = c_0$. Also, from Eq. (S18), the hydrostatic pressure in $\sigma_{rr} = 2\mu_{skin}\lambda_r^\alpha/\alpha - p(r)$ can be solved as

$$p(r) = \frac{2\mu_{skin}}{\alpha(\lambda_z \lambda_\theta)^\alpha} - [\phi(\lambda_z, \lambda_\theta) - \phi(\lambda_z, \lambda_{\theta|a_0})] \quad (S20)$$

Therefore, the Cauchy stress in the z-direction can be expressed as

$$\sigma_z = \frac{2\mu_{skin}\lambda_z^\alpha}{\alpha} - p(r) = \frac{2\mu_{skin}\lambda_z^\alpha}{\alpha} - \frac{2\mu_{skin}}{\alpha(\lambda_z \lambda_\theta)^\alpha} + [\phi(\lambda_z, \lambda_\theta) - \phi(\lambda_z, \lambda_{\theta|a_0})] \quad (S21)$$

To solve Eq. (S21), instead of assuming $\sigma_z = 0$, we adopt the relaxed boundary condition of zero resultant force at the arbitrary z-plane¹⁷ as

$$0 = \int_{a_1}^{c_1} \sigma_z r dr = \int_{\lambda_{\theta|a_0}}^{\lambda_{\theta|c_0}} \sigma_z \frac{a_0^2 \lambda_\theta (1 - \lambda_z \lambda_{\theta|a_0}^2)}{(1 - \lambda_z \lambda_\theta^2)^2} d\lambda_\theta \quad (S22)$$

where the incompressibility enforces that

$$\lambda_z (\lambda_{\theta|c_0}^2 c_0^2 - \lambda_{\theta|a_0}^2 a_0^2) = c_0^2 - a_0^2 \quad (S23)$$

Therefore, one can solve three unknowns $\lambda_z, \lambda_{\theta|c_0}, \lambda_{\theta|a_0}$ with Eqs. (S19), (S22), and (S23). Then, we can solve the deformation field

$$\lambda_\theta = \sqrt{\frac{R^2 - a_0^2 + \lambda_z a_1^2}{\lambda_z R^2}} \quad (S24)$$

$$\lambda_r = \frac{1}{\lambda_z \lambda_\theta}$$

as well as the stress field

$$\sigma_\theta = \frac{2\mu_{skin}\lambda_\theta^\alpha}{\alpha} - p(r)$$

$$\sigma_r = \frac{2\mu_{skin}\lambda_r^\alpha}{\alpha} - p(r) \quad (S25)$$

which are plotted in Supplementary Fig. 9. It is apparent that when the out boundary is considerably large (i.e., $c_0/a_0 \gg 1$), the converged analytical solutions show that hoop stretch at wound edge $\lambda_{\theta|a_0} = a_1/a_0 = 1.09$. In other words, the size of wound becomes 1.09 times larger than the initial size (i.e., $a_1/a = 1.05$) due to the presence of pre-strain in the native skin.

1.2. Contraction of wound by the strain-programmed patch

Next, we can solve a_{closure} after applying the strain-programmed patch to the wounded skin. Analytical solutions can be obtained when the strain-programmed patch has the same size as that of the enlarged wound (i.e., $\lambda_{\text{patch}}^{\text{pre}} b_0 = a_1 = 1.05a$) without overlapping area. Let $\sigma_{r,\text{patch}}^i$ and $\sigma_{r,\text{skin}}^i$ denote the interfacial radial stress on the strain-programmed patch and the skin, respectively. The force balance requires that

$$\sigma_{r,\text{patch}}^i H_{\text{patch}} = \sigma_{r,\text{skin}}^i H_{\text{skin}} \quad (\text{S26})$$

where H_{patch} and H_{skin} are thickness of the strain-programmed patch and the skin, respectively. As for the skin, stress boundary conditions at $r = a_{\text{closure}}$ now changes to $\sigma_{rr}|_{r=a_{\text{closure}}} = \sigma_{r,\text{skin}}^i$. Similar analysis can be performed to find three equations as

$$\begin{aligned} \sigma_{\infty} - \sigma_{r,\text{skin}}^i &= \phi(\lambda_z, \lambda_{\theta}) - \phi(\lambda_z, \lambda_{\theta|a_0}) \\ 0 &= \int_{a_{\text{closure}}}^{c_2} \sigma_z r dr \\ \lambda_z (\lambda_{\theta|c_0}^2 c_0^2 - \lambda_{\theta|a_0}^2 a_0^2) &= c_0^2 - a_0^2 \end{aligned} \quad (\text{S27})$$

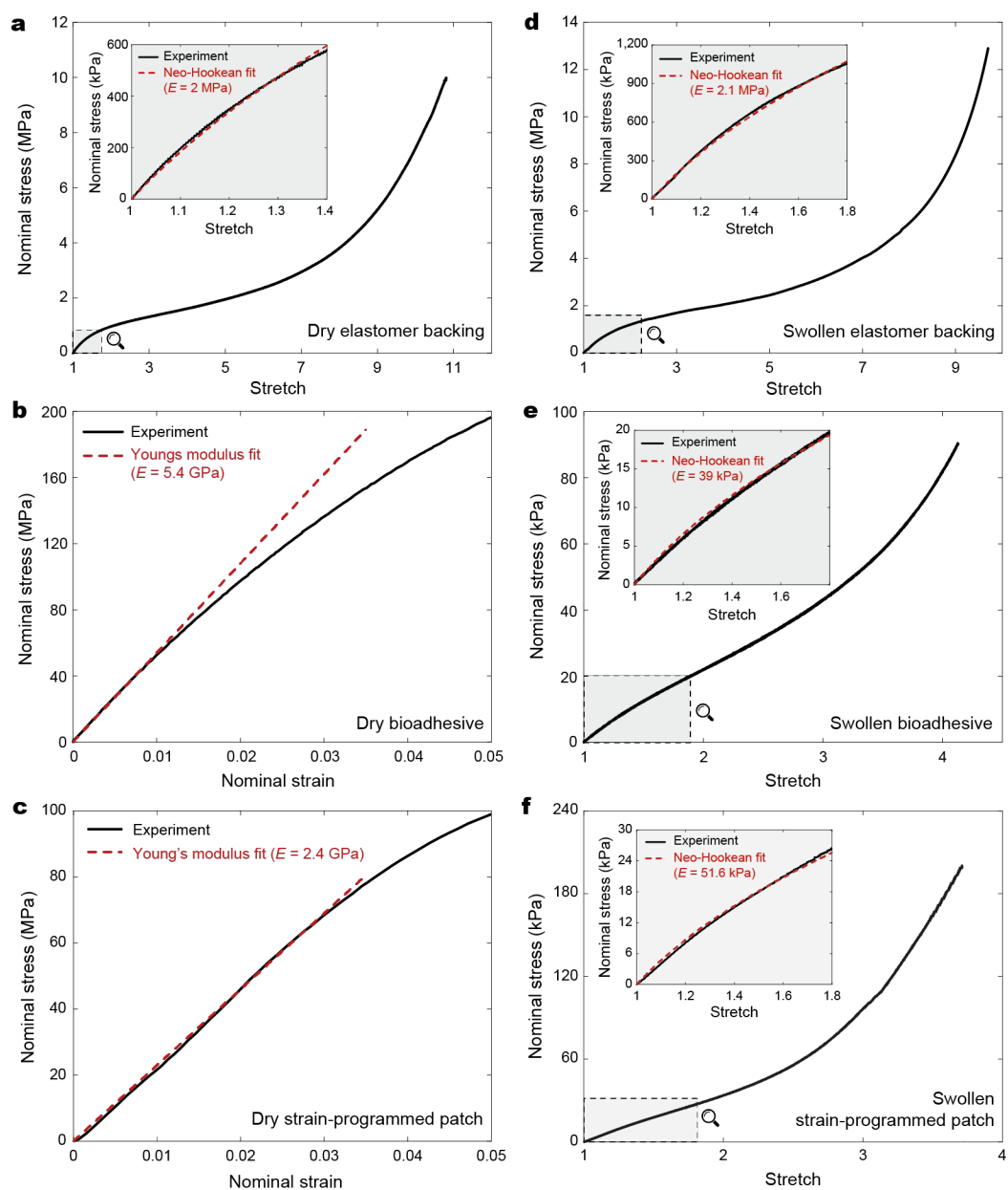
from which one can solve λ_z , $\lambda_{\theta|a_0} = a_{\text{closure}}/a$, and $\lambda_{\theta|c_0} = c_2/c_0$ as a function of $\lambda_{\text{patch}}^{\text{pre}}$. The analytical solution from Eq. (S27) are plotted in Fig. 3d, Supplementary Figs. 11d, and 20d which validates the finite-element results. Note that the analytical solutions are only available when the strain-programmed patch size equals to $a_1 = 1.1a$ for diabetic mouse and porcine skin and $a_1 = 1.05a$ for human skin. For the strain-programmed patch with larger sizes, finite-element modeling-based analysis is required as discussed in the following section.

2. Finite-element modeling

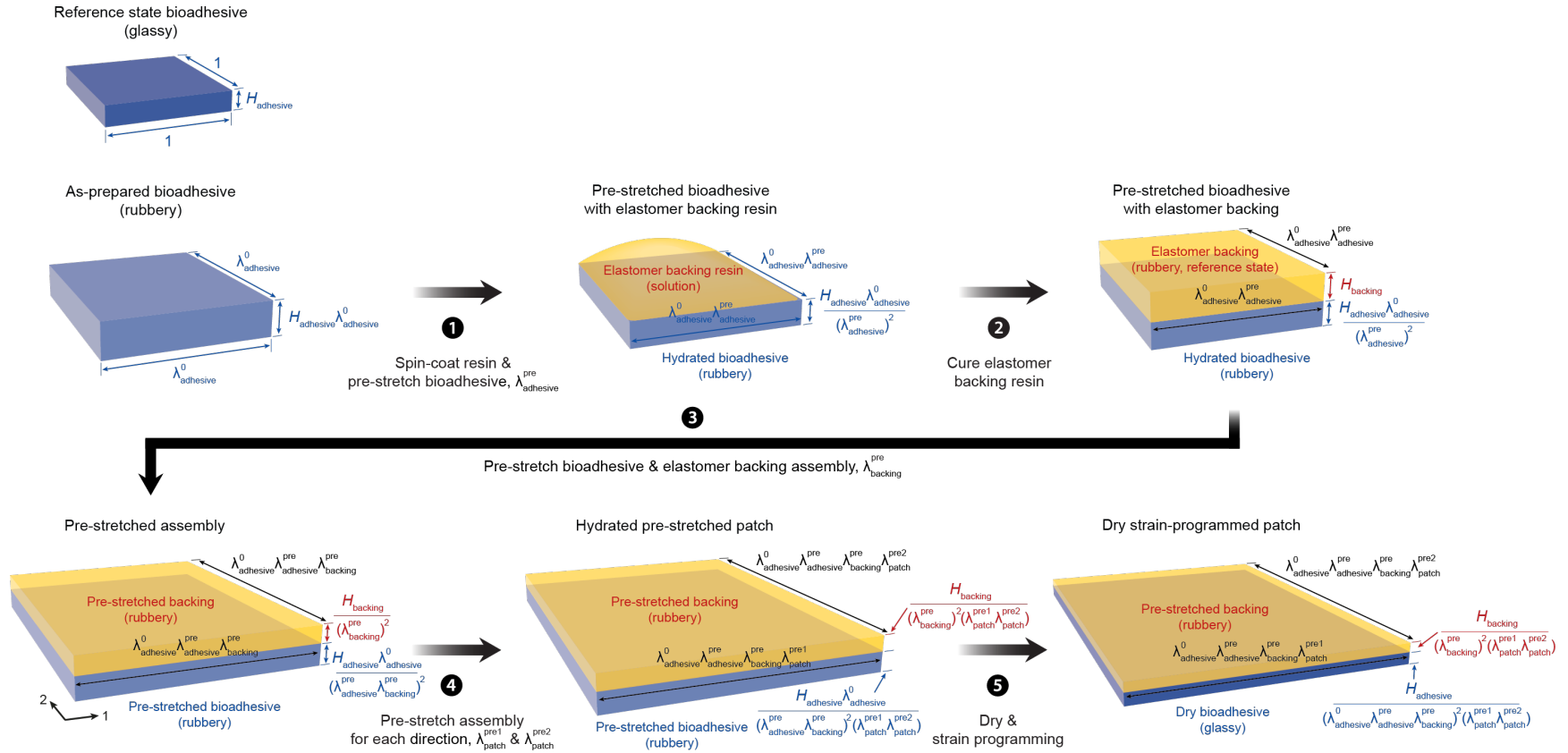
To quantitatively analyze the closure and stress remolding of wounds by the strain-programmed patch larger than the wound size (i.e., $b_0 > 1.1a$ for diabetic mouse and porcine skin, $b_0 > 1.05a$ for human skin), we develop 2D axisymmetric finite-element models based on a commercially-available software (ABAQUS/Standard 2017, Dassault Systèmes®). The finite-element setups are illustrated in Supplementary Fig. 10. The human skin was modeled as an incompressible Ogden hyperelastic solid (fitting parameters: $\mu_{\text{human}} = 40$ kPa, $\alpha_{\text{human}} = 20$) with 3.5 % tensile pre-strain¹⁸. The db/db mouse skin was modeled as an incompressible Ogden hyperelastic solid (fitting parameters: $\mu_{\text{mouse}} = 25$ kPa, $\alpha_{\text{mouse}} = 7$) with 3.5 % tensile pre-strain. The porcine skin was modeled as Ogden hyperelastic solid (fitting parameters: $\mu_{\text{pig}} = 57$ kPa, $\alpha_{\text{pig}} = 8$) with 3.5 % tensile pre-strain. The strain-programmed patch was modeled as a neo-Hookean solid (fitting parameter: $\mu_{\text{patch}}^{\infty} = 17.2$ kPa) with varying patch sizes and pre-stretches used in strain-programming process. Three mechanical quantities, (i) wound closure ratio defined as a_{closure}/a (Fig. 3d, Supplementary Figs. 11d, and 20d), (ii) normalized hoop stress $\sigma_{\theta}/\sigma_{\infty}$ (Fig. 3e, Supplementary Figs. 11e, and 20e), and (iii) normalized radial stress σ_r/σ_{∞} (Fig. 3f, Supplementary Figs. 11f, and 20f) are obtained from the finite-element models for human, db/db mouse, and porcine skin.

Supplementary References

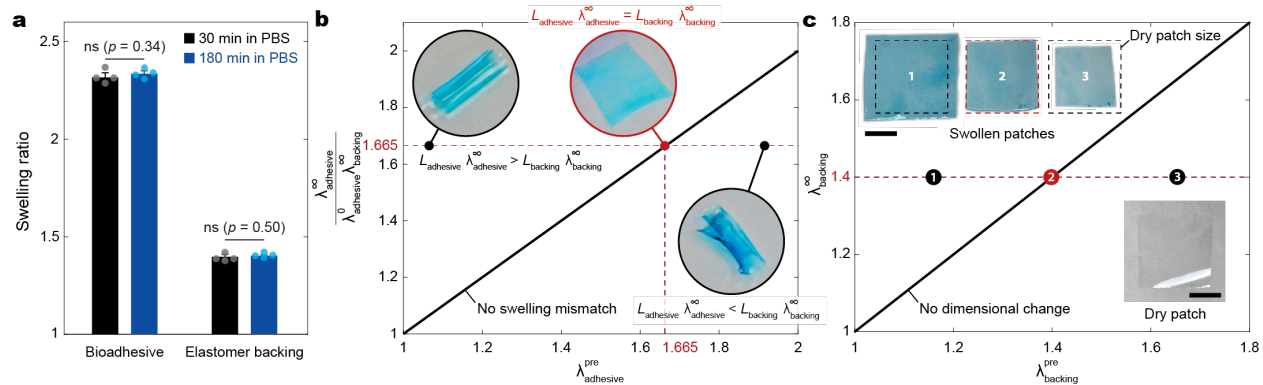
- 1 Liu, C., Qin, H. & Mather, P. Review of progress in shape-memory polymers. *Journal of Materials Chemistry* **17**, 1543-1558 (2007).
- 2 Mather, P. T., Luo, X. & Rousseau, I. A. Shape memory polymer research. *Annual Review of Materials Research* **39**, 445-471 (2009).
- 3 Meng, H. & Li, G. A review of stimuli-responsive shape memory polymer composites. *Polymer* **54**, 2199-2221 (2013).
- 4 Lendlein, A. & Langer, R. Biodegradable, elastic shape-memory polymers for potential biomedical applications. *Science* **296**, 1673-1676 (2002).
- 5 Yuk, H. *et al.* Dry double-sided tape for adhesion of wet tissues and devices. *Nature* **575**, 169-174 (2019).
- 6 Mao, X., Yuk, H. & Zhao, X. Hydration and swelling of dry polymers for wet adhesion. *Journal of the Mechanics and Physics of Solids* **137**, 103863 (2020).
- 7 Frisch, H., Wang, T. & Kwei, T. Diffusion in glassy polymers. II. *Journal of Polymer Science Part A-2: Polymer Physics* **7**, 879-887 (1969).
- 8 Kelley, F. N. & Bueche, F. Viscosity and glass temperature relations for polymer-diluent systems. *Journal of Polymer Science* **50**, 549-556 (1961).
- 9 Flory, P. J. & Rehner Jr, J. Statistical mechanics of cross-linked polymer networks I. Rubberlike elasticity. *The Journal of Chemical Physics* **11**, 512-520 (1943).
- 10 Flory, P. J. *Principles of polymer chemistry*. (Cornell University Press, 1953).
- 11 Bouklas, N. & Huang, R. Swelling kinetics of polymer gels: comparison of linear and nonlinear theories. *Soft Matter* **8**, 8194-8203 (2012).
- 12 Cai, S. & Suo, Z. Equations of state for ideal elastomeric gels. *Europhysics Letters* **97**, 34009 (2012).
- 13 Yeoh, O. H. Some forms of the strain energy function for rubber. *Rubber Chemistry and Technology* **66**, 754-771 (1993).
- 14 Michel, R. *et al.* Interfacial fluid transport is a key to hydrogel bioadhesion. *Proceedings of the National Academy of Sciences* **116**, 738-743 (2019).
- 15 Sun, M., Kumar, N., Dhinojwala, A. & King, H. Attractive forces slow contact formation between deformable bodies underwater. *Proceedings of the National Academy of Sciences* **118** (2021).
- 16 Chen, X., Yuk, H., Wu, J., Nabzdyk, C. S. & Zhao, X. Instant tough bioadhesive with triggerable benign detachment. *Proceedings of the National Academy of Sciences* **117**, 15497-15503, doi:doi: 10.1073/pnas.2006389117 (2020).
- 17 Liang, X., Tao, F. & Cai, S. Creasing of an everted elastomer tube. *Soft Matter* **12**, 7726-7730 (2016).
- 18 Berezovsky, A. B. *et al.* Primary contraction of skin grafts: a porcine preliminary study. *Plast Aesthet Res Serial Online* **25**, 22-26 (2015).
- 19 Volk, S. W. & Bohling, M. W. Comparative wound healing—are the small animal veterinarian's clinical patients an improved translational model for human wound healing research? *Wound Repair and Regeneration* **21**, 372-381 (2013).
- 20 Scherer, S. S. *et al.* Wound healing kinetics of the genetically diabetic mouse. *Wounds* **20**, 18-28 (2008).
- 21 Wang, X. T., McKeever, C. C., Vonu, P., Patterson, C. & Liu, P. Y. Dynamic histological events and molecular changes in excisional wound healing of diabetic DB/DB mice. *Journal of Surgical Research* **238**, 186-197 (2019).
- 22 Gay, D. *et al.* Phagocytosis of Wnt inhibitor SFRP4 by late wound macrophages drives chronic Wnt activity for fibrotic skin healing. *Science Advances* **6**, eaay3704 (2020).



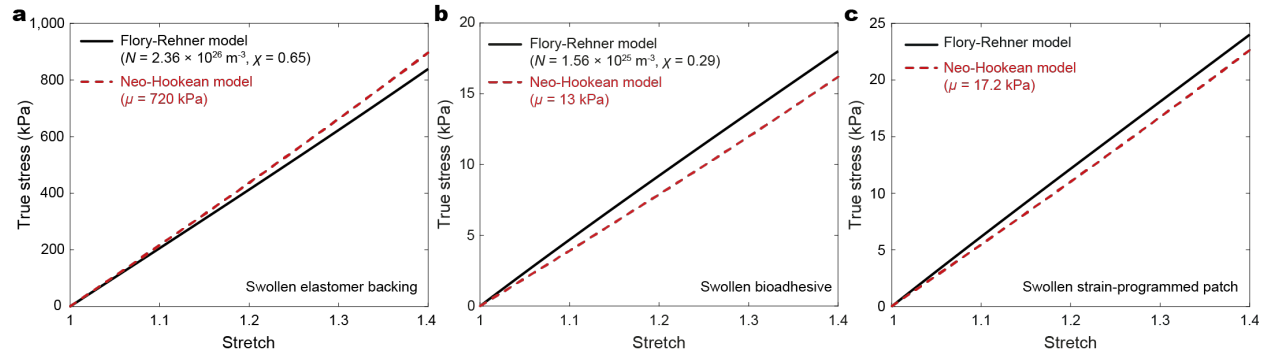
Supplementary Fig. 1 | Mechanical properties of the strain-programmed patch. a-c, Nominal stress vs. stretch curves for dry elastomer backing (a), bioadhesive (b), and strain-programmed patch (c). **d-f**, Nominal stress vs. stretch curves for fully swollen elastomer backing (d), bioadhesive (e), and strain-programmed patch (f).



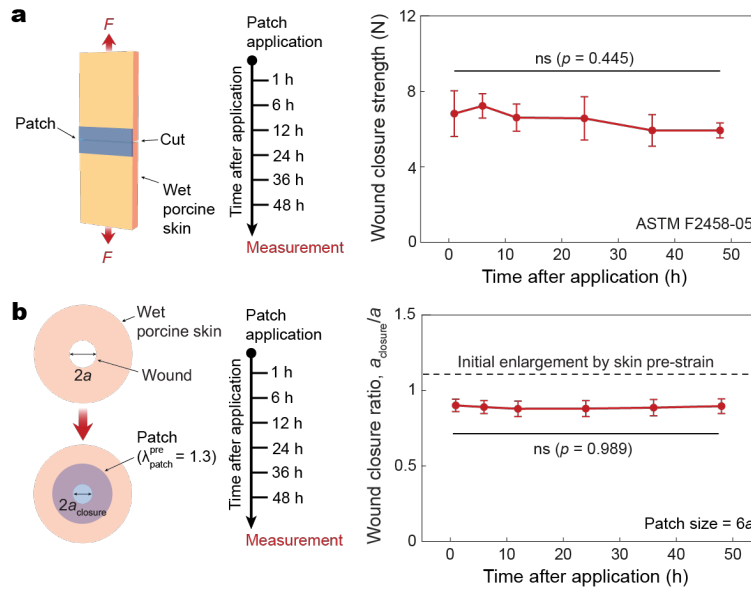
Supplementary Fig. 2 | Fabrication of the strain-programmed patch. (1) Spin-coat elastomer backing resin on an as-prepared bioadhesive and pre-stretch the as-prepared bioadhesive by ratio of $\lambda_{\text{adhesive}}^{\text{pre}}$. (2) Cure elastomer backing resin while keeping the bioadhesive hydrated. (3) Pre-stretch the bioadhesive and elastomer backing assembly by ratio of $\lambda_{\text{backing}}^{\text{pre}}$. (4) Pre-stretch the bioadhesive patch along two in-plane directions by ratios of $\lambda_{\text{patch}}^{\text{pre1}}$ and $\lambda_{\text{patch}}^{\text{pre2}}$, respectively. (5) Dry the bioadhesive for shape-memory to finalize fabrication of the strain-programmed patch.



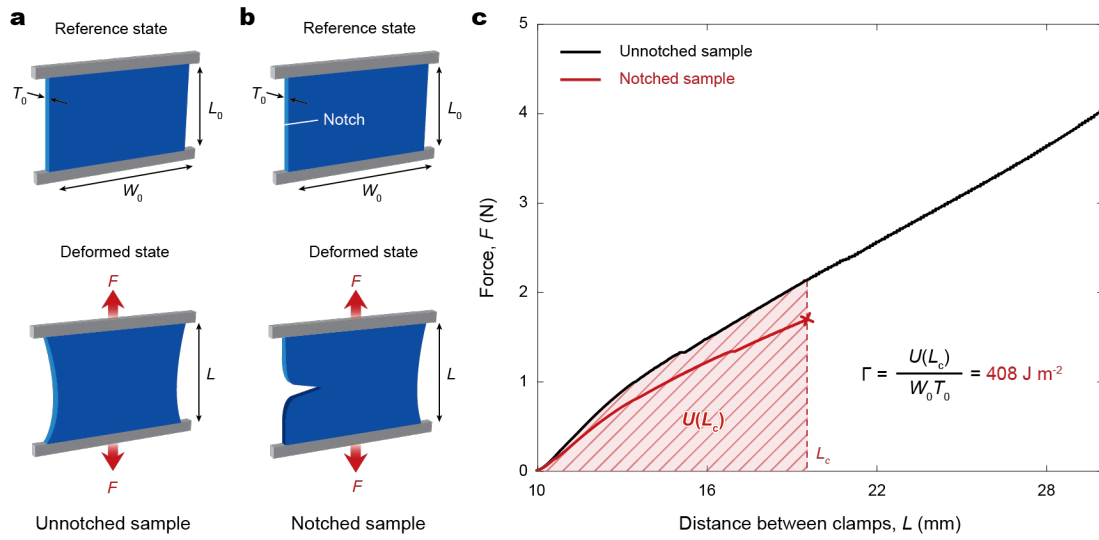
Supplementary Fig. 3 | Swelling of the strain-programmed patch. **a**, Swelling ratios of elastomer backing and bioadhesive in a PBS bath. **b**, Swelling mismatch canceling between elastomer backing and bioadhesive in the strain-programmed patch. **c**, Swelling canceling of the strain-programmed patch. Values in **a** represent the mean and the standard deviation ($n = 4$; independent samples). Statistical significance and p values are determined by two-sided t -test; ns, not significant. Scale bars, 10 mm (c).



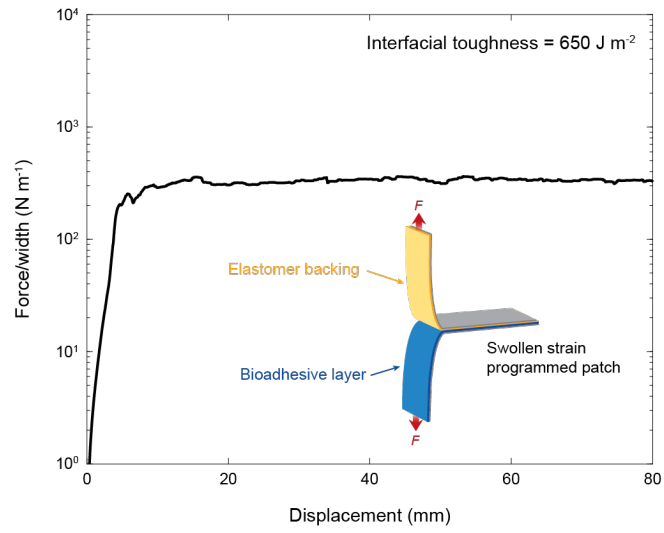
Supplementary Fig. 4 | Comparison between Flory-Rehner and neo-Hookean models. a-c, True stress vs. stretch obtained based on Flory-Rehner and neo-Hookean models for swollen elastomer backing (a), bioadhesive (b), and strain-programmed patch (c).



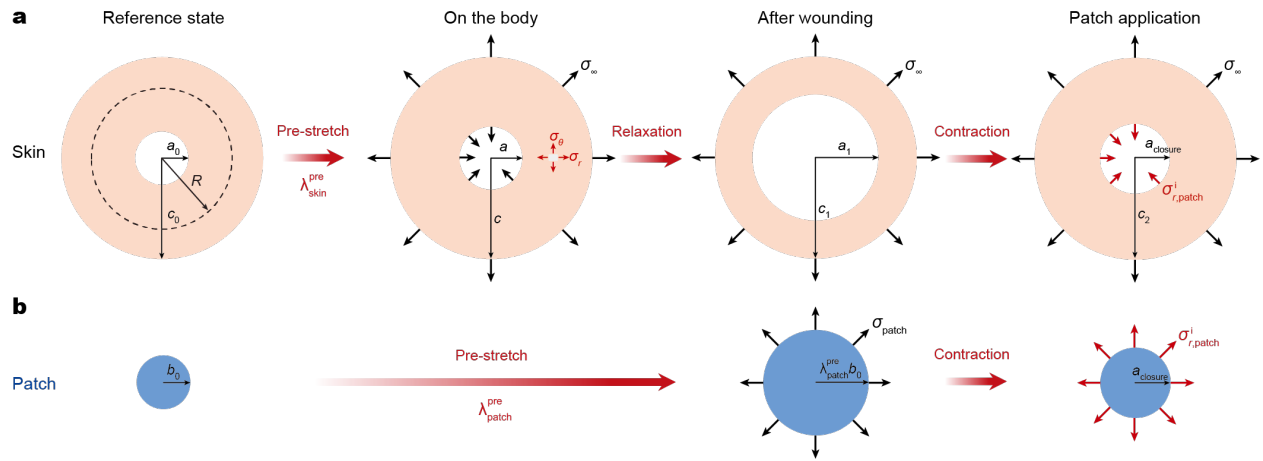
Supplementary Fig. 5 | Long-term adhesion and wound contraction performance. a, Wound closure strength of the strain-programmed patch over different time after the initial application on wet porcine skin. **b**, Wound closure ratio by the strain-programmed patch over different time after the initial application on wet porcine skin. Values represent the mean and the standard deviation ($n = 3$; independent samples). Statistical significance and p values are determined by one-way ANOVA followed by Tukey's multiple comparison test; ns, not significant.



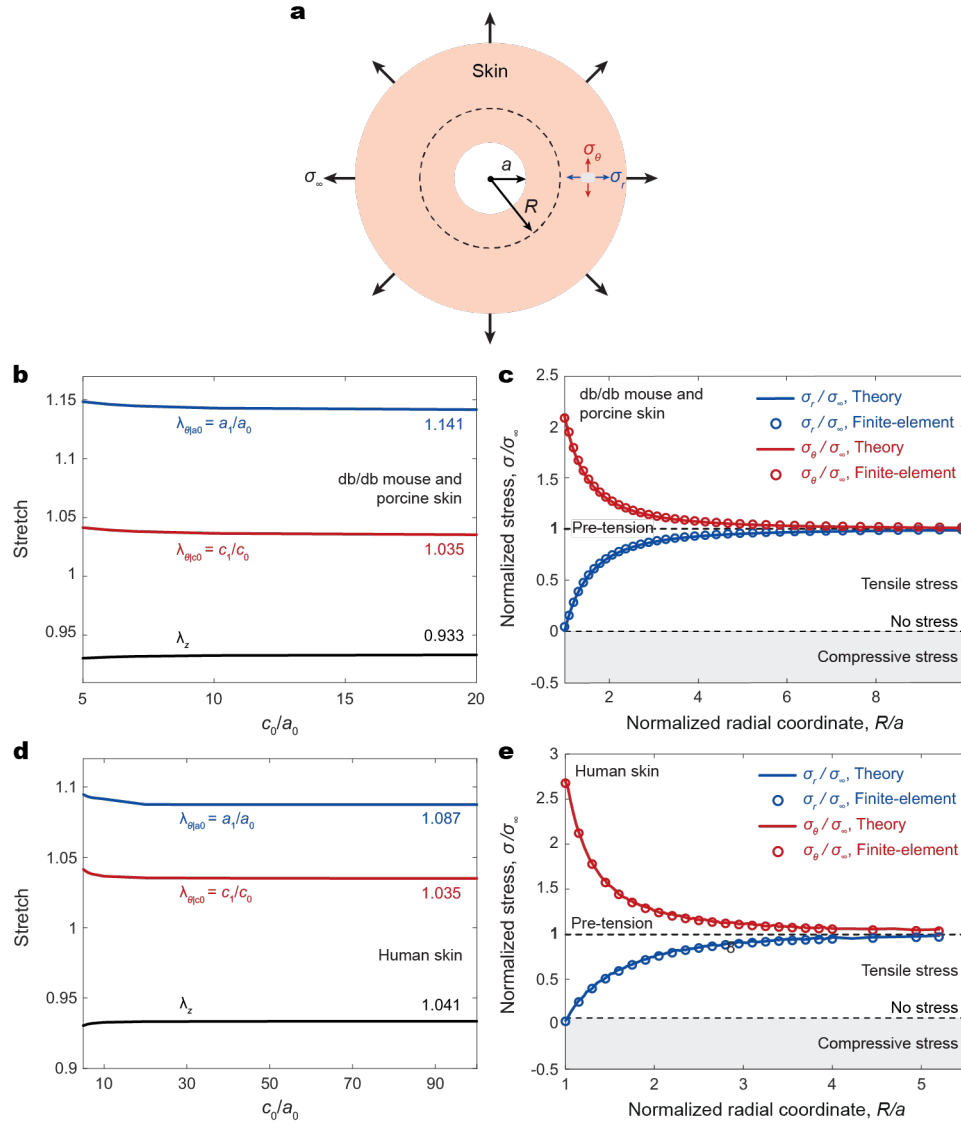
Supplementary Fig. 6 | Fracture toughness of the strain-programmed patch. **a,b**, Schematic illustrations of pure-shear test for an unnotched sample (a) and a notched sample (b). **c**, Force vs. distance between clamps for the unnotched and notched fully swollen strain-programmed patch for fracture toughness measurement. L_c indicates the critical distance between the clamps at which the notch turns into a running crack. The measured fracture toughness of the strain-programmed patch is 408 J m^{-2} .



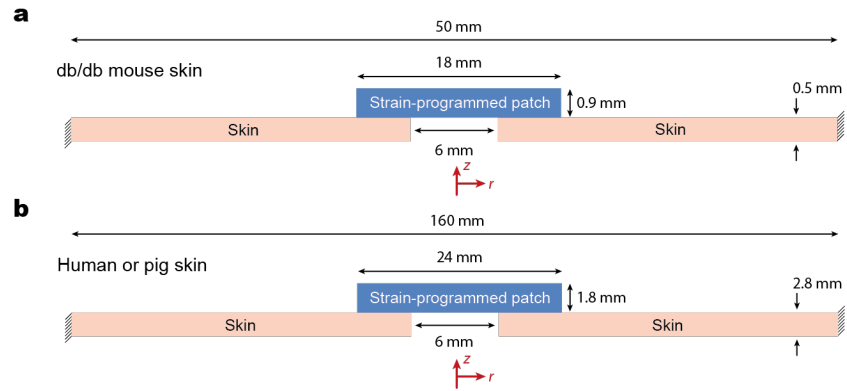
Supplementary Fig. 7 | Interfacial toughness between elastomer backing and bioadhesive in the strain-programmed patch. The measured interfacial toughness between swollen elastomer backing and bioadhesive is 650 J m⁻².



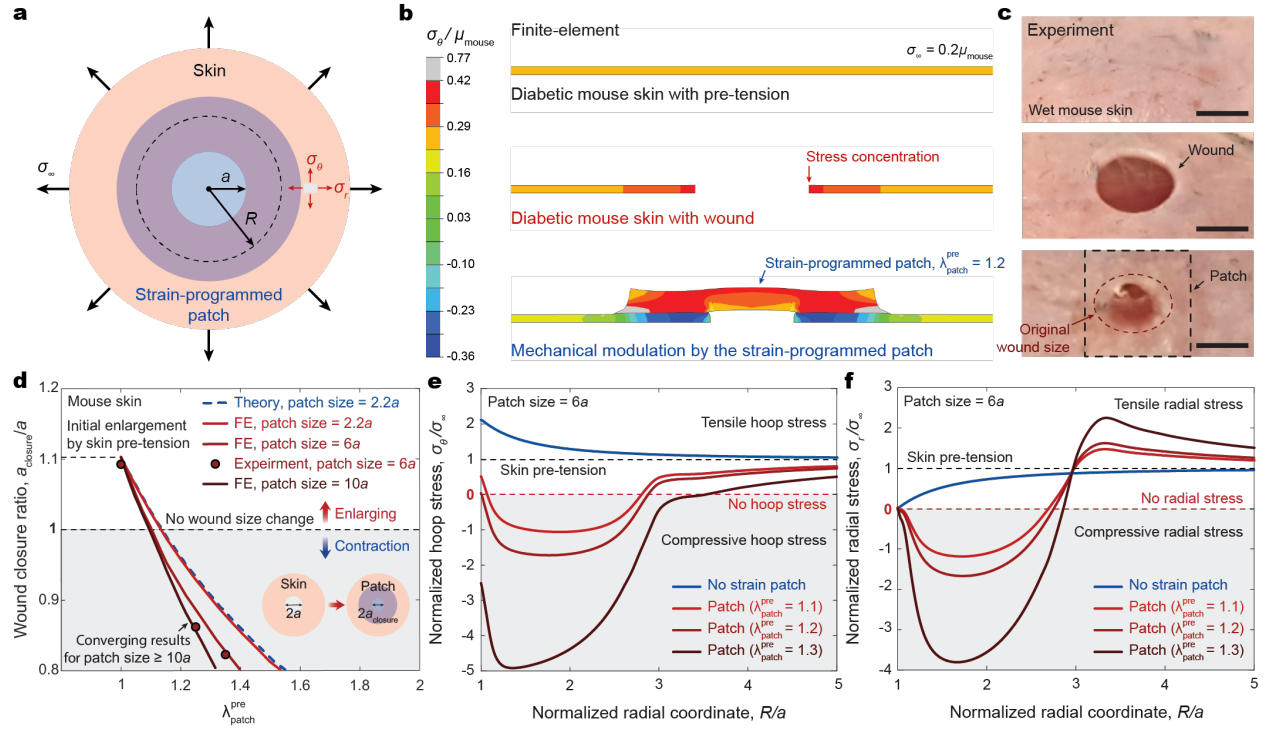
Supplementary Fig. 8 | Schematic configuration for the analytical modeling. a,b, Axisymmetric configuration of the wounded skin (a) and the strain-programmed patch (b).



Supplementary Fig. 9 | Comparison of analytical and finite-element analyses. a, Schematic illustration for axisymmetric configuration for analytical and finite-element analyses. **b**, Analytically solved stretches of the wounded db/db mouse and porcine skin as a function of c_0/a_0 . **c**, Stress distribution within the wounded db/db mouse and porcine skin calculated from the analytical solutions (solid lines) and the corresponding finite-element results (circles). **d**, Analytically solved stretches of the wounded human skin as a function of c_0/a_0 . **e**, Stress distribution within the wounded human skin calculated from the analytical solutions (solid lines) and the corresponding finite-element results (circles).



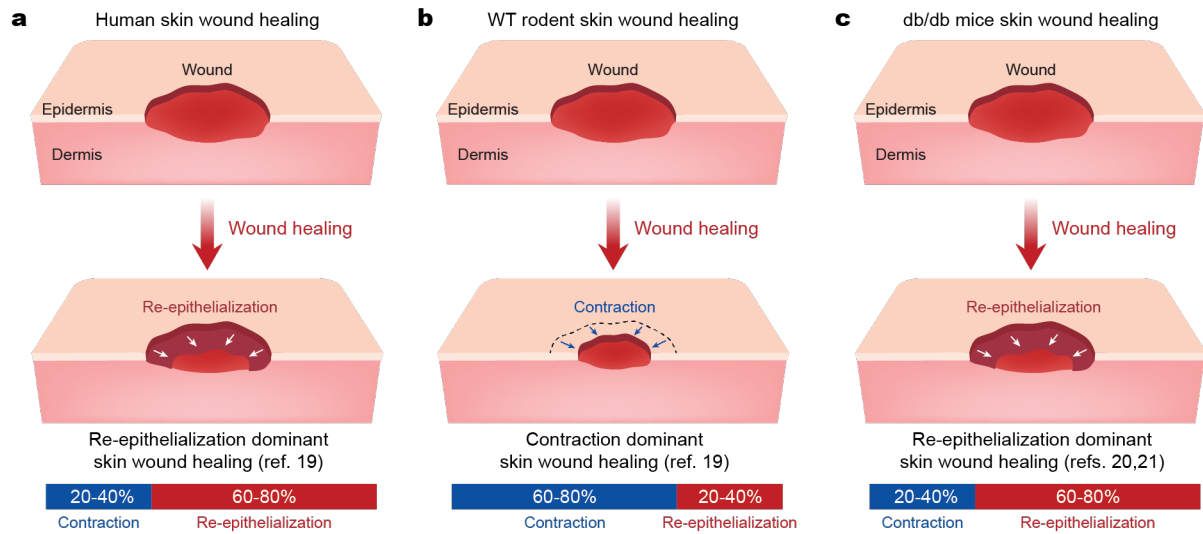
Supplementary Fig. 10 | Finite-element modeling for wound closure by the strain-programmed patch. a,b, Finite-element setups for db/db mouse skin (a) and human and porcine skin (b) with wound and the strain-programmed patch.



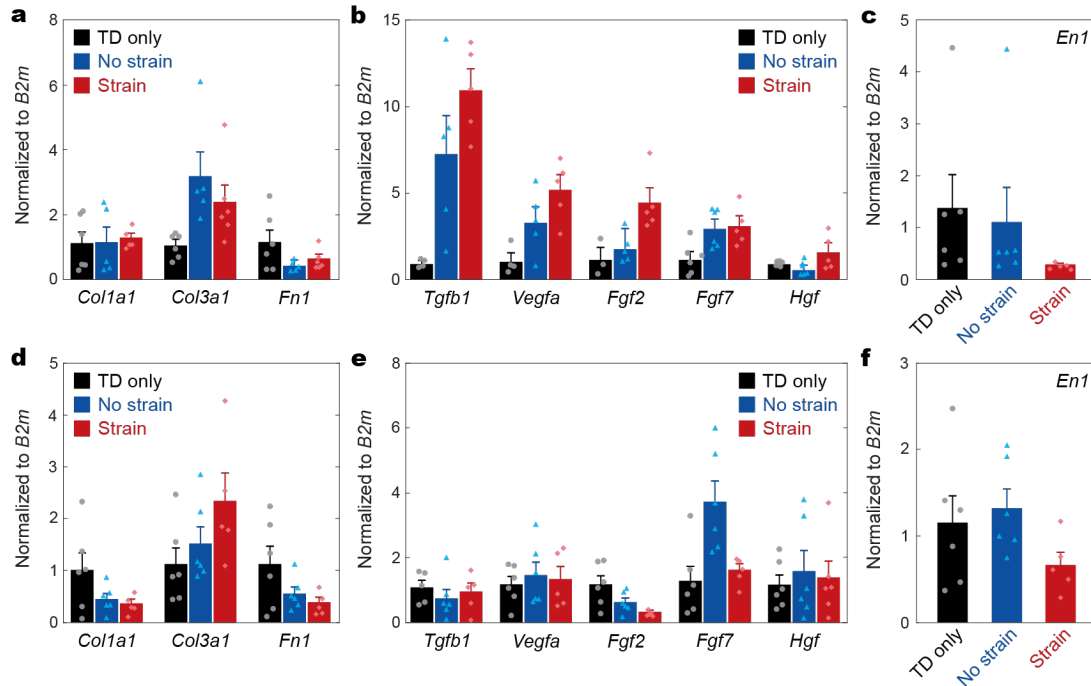
Supplementary Fig. 11 | Mechanical modulation of diabetic mouse skin wounds. **a**, Schematic illustration for the theoretical and finite-element analyses. **b,c**, Representative finite-element results (**b**) and the corresponding experiment images of the db/db mouse skin (**c**) mechanically modulated by the strain-programmed patch ($\lambda_{\text{patch}}^{\text{pre}} = 1.2$; size = 3 times of the wound diameter). The shear modulus of the diabetic mouse skin is denoted as μ_{mouse} , the hoop stress in the diabetic mouse skin as σ_θ , and the residual stress in the intact diabetic mouse skin as σ_∞ . **d**, Finite-element and experimental results for the wound closure ratio as a function of $\lambda_{\text{patch}}^{\text{pre}}$. **e,f**, Finite-element results for the hoop (σ_θ , **e**) and the radial (σ_r , **f**) stress around the wound for the strain-programmed patch with varying $\lambda_{\text{patch}}^{\text{pre}}$. Scale bars, 5 mm (**c**).



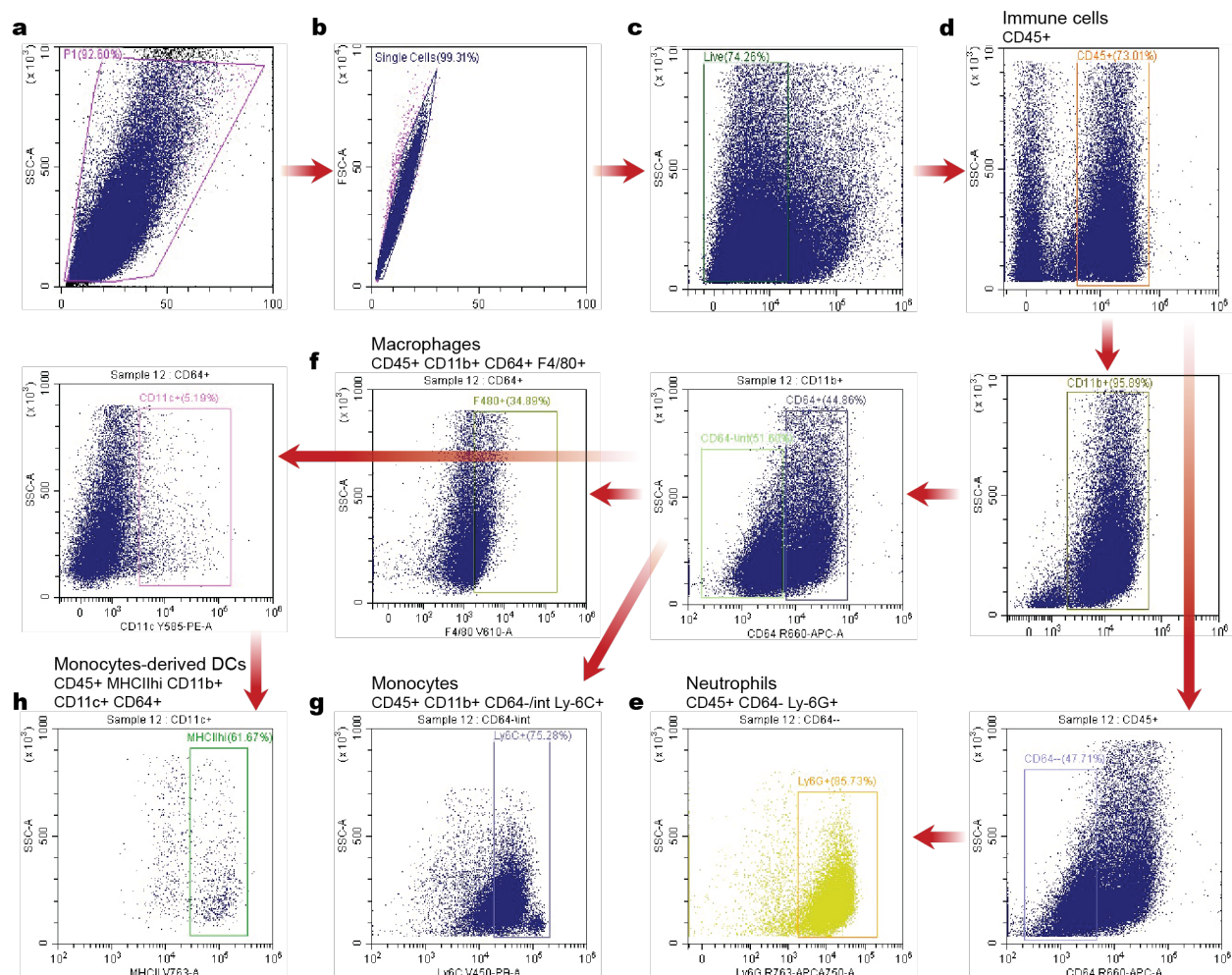
Supplementary Fig. 12 | Strain-programmed patch for large diabetic wounds. **a**, Representative example of large diabetic foot ulcer (DFU) in patients. **b**, *Ex vivo* porcine skin wound based on the large DFU example. **c**, Mechanical modulation of *ex vivo* porcine skin wound by the strain-programmed patch ($\lambda_{\text{patch}}^{\text{pre}} = 1.3$). Scale bars, 5 mm.



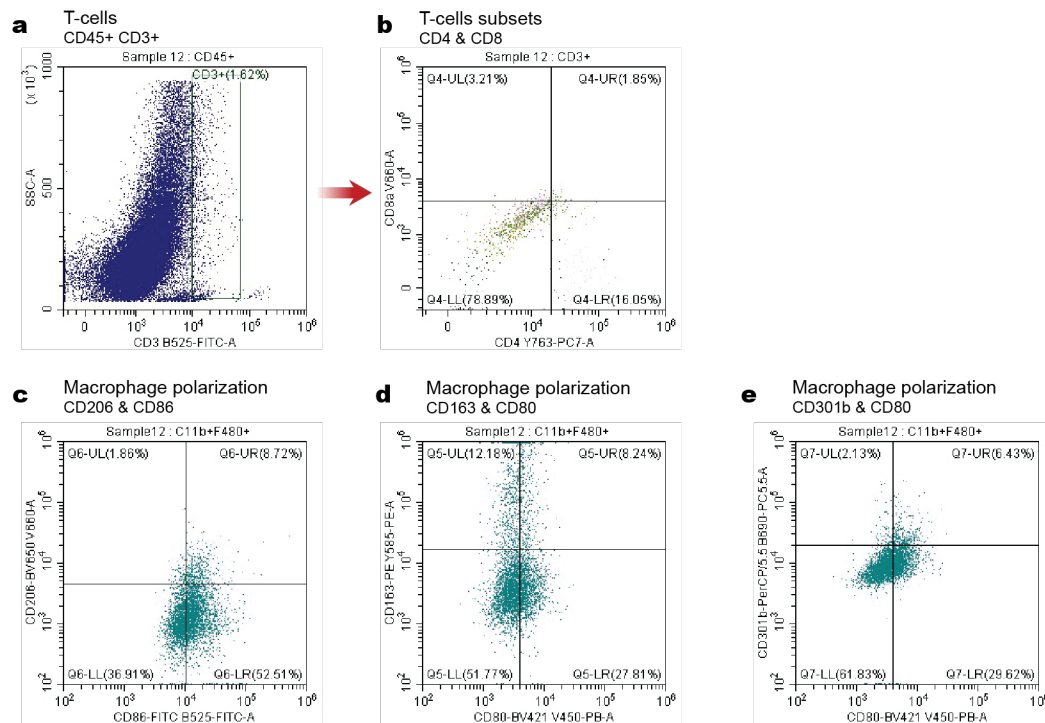
Supplementary Fig. 13 | Skin wound healing in human, wild type rodent, and db/db mouse. a-c, Skin wound healing by contraction and re-epithelialization in human¹⁹ (a), wild type (WT) rodent¹⁹ (b), and db/db mouse^{20,21} (c).



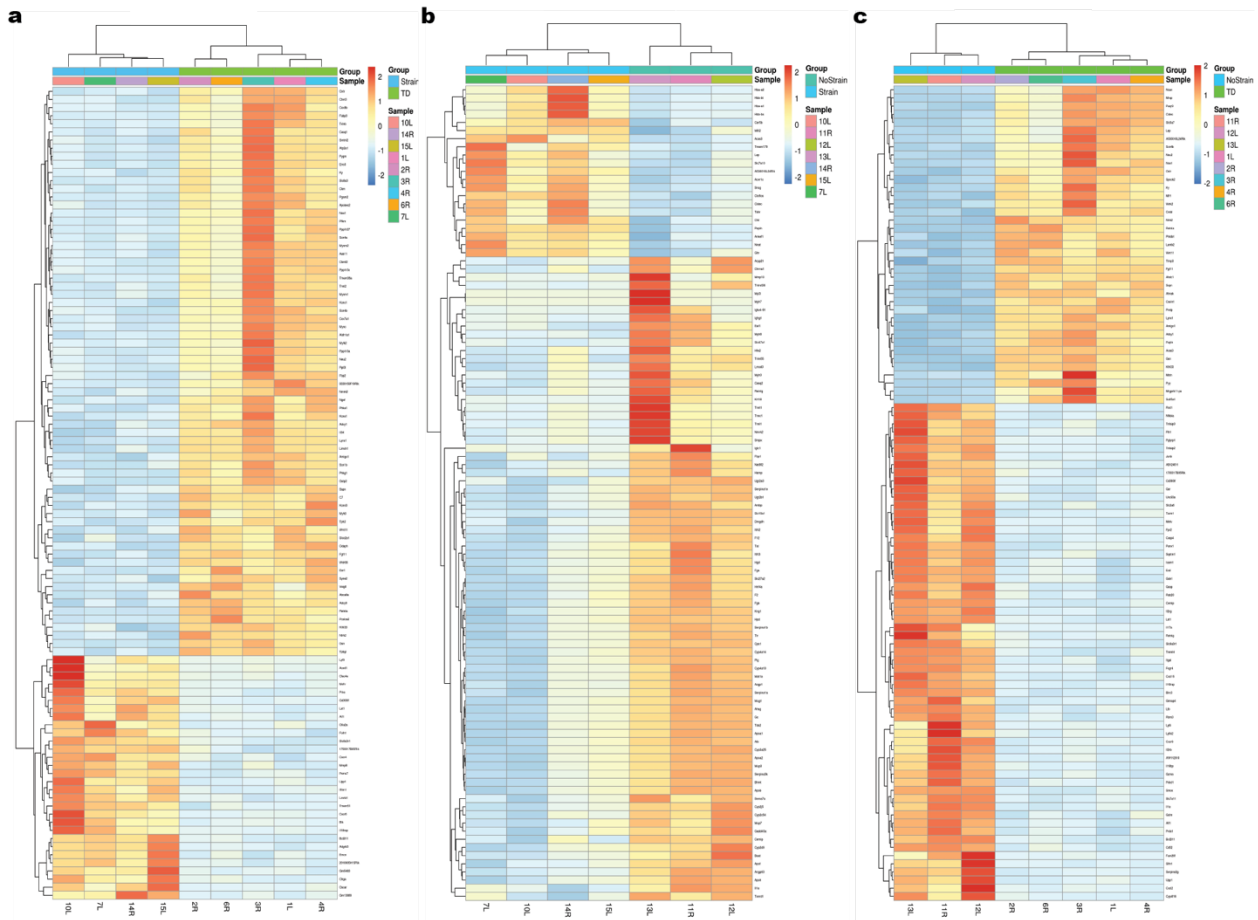
Supplementary Fig. 14 | RT-qPCR gene expression analysis of diabetic mouse wound. a,b, RT-qPCR analysis on day 5 (D5) wounds for ECM-related (a) and growth factor (b) genes. **c,** *Engrailed-1* (*En1*) wound expression on D5. **d,e,** RT-qPCR analysis on day 10 (D10) wounds for ECM-related (d) and growth factor (e) genes. **f,** *Engrailed-1* (*En1*) wound expression on D10. Values represent the mean and the standard error of the mean ($n = 6$ for TD Only, 5 for No Strain and 6 for Strain except for *Col1a1* where it is 5 in **a**; $n = 4$ for TD Only, 5 for No Strain and 5 for Strain for *Tgfb1* and *Vegfa*; $n = 3$ for TD Only, 5 for No Strain and 5 for Strain for *Fgf2*; $n = 6$ for TD Only, 6 for No Strain and 5 for Strain for *Fgf7* and *Hgf* in **b**; $n = 6$ for TD Only, 6 for No Strain and 5 for Strain in **c**; $n = 6$ for TD Only, 6 for No Strain and 5 for Strain in **d**; $n = 5$ for TD Only, 6 for No Strain and 5 for Strain for *Tgfb1*; $n = 6$ for TD Only, 6 for No Strain and 5 for Strain for *Vegfa*, *Fgf2* and *Fgf7*; $n = 6$ for TD Only, 6 for No Strain and 6 for Strain for *Hgf* in **e**; $n = 6$ for TD Only, 6 for No Strain and 5 for Strain in **f**; independent samples).



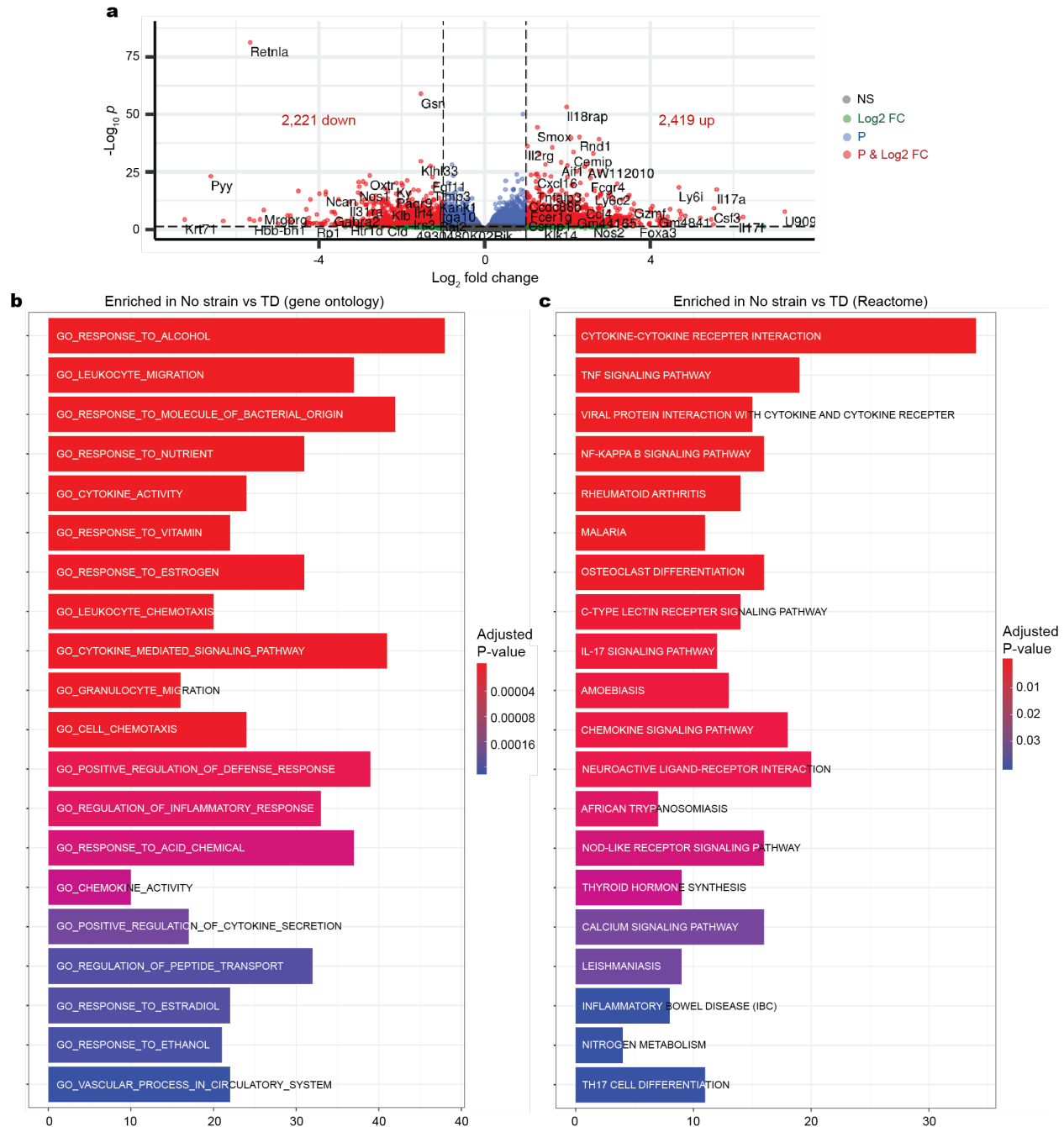
Supplementary Fig. 15 | Gating strategy for the flow cytometry analysis of dissociated wound tissues. **a-h**, Forward and side scatter density plot (a) was used for debris exclusion followed by forward scatter area vs forward scatter height density plot (b) for doublet exclusion. Live (c) immune cells (d) were then characterized as neutrophils (e), macrophages (f), monocytes (g), and monocyte derived dendritic cells (h) with appropriate cell surface antibody staining and sequential gating.



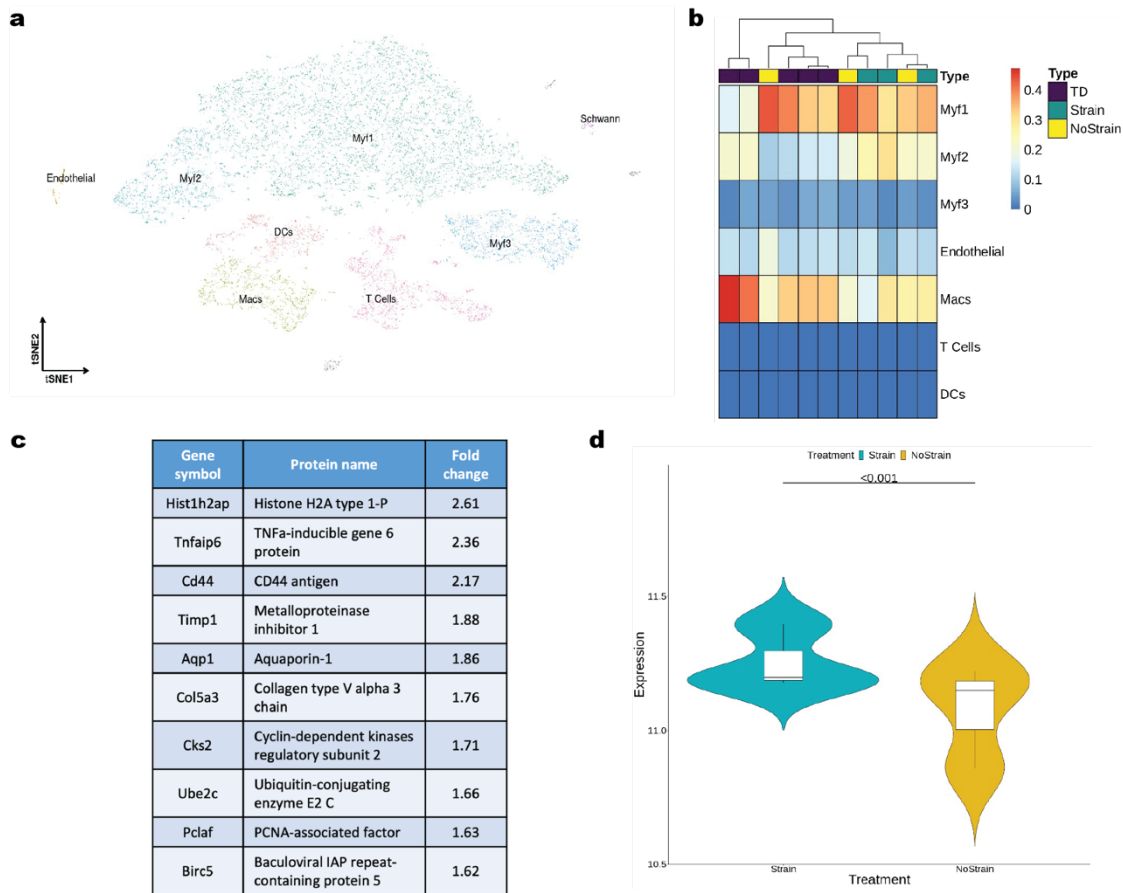
Supplementary Fig. 16 | Additional gating strategy for T-cell subsets and polarized macrophages.
a-e, Single, live, immune cells were characterized as T-cells (a) and further gated according to CD4 and CD8 expression (b). Density plot graphs were also used to distinguish macrophage (single, live, CD45+CD11b+CD64+F4/80+ cells') polarized states (c-e).



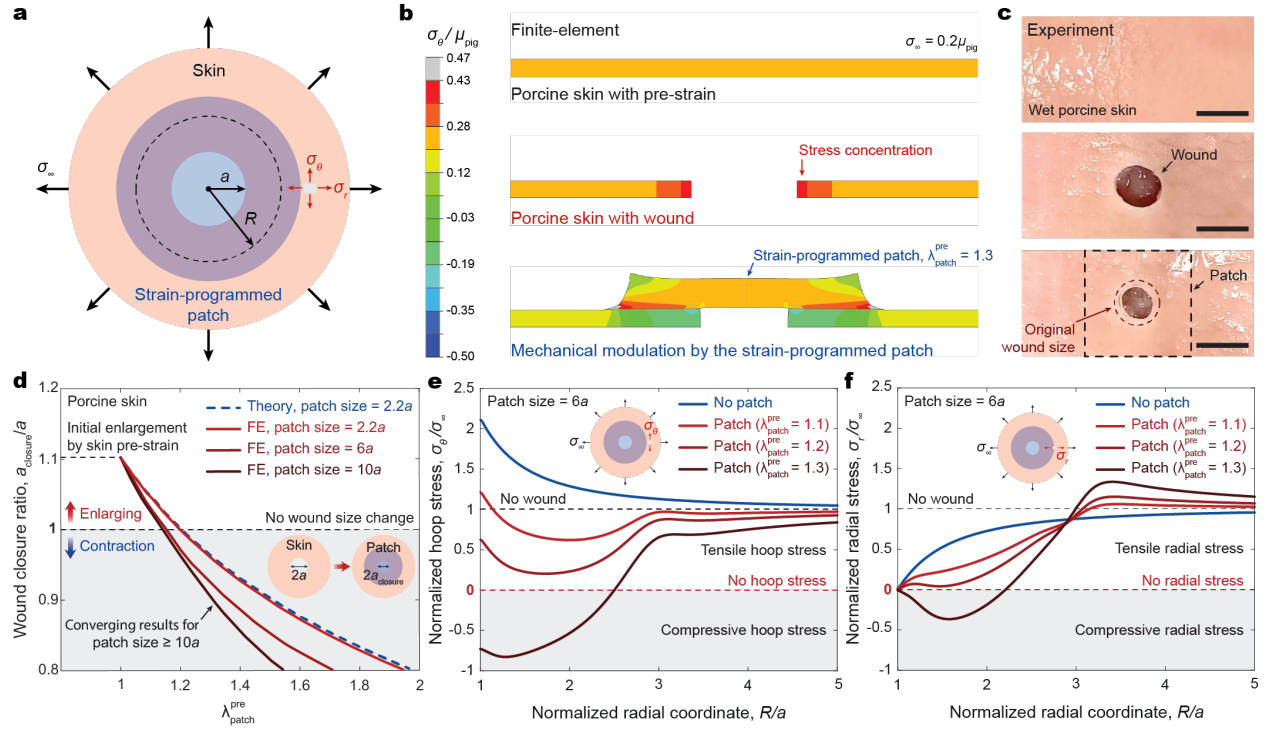
Supplementary Fig. 17 | Visualization of RNA sequencing results. a-c, Heatmaps generated from the top 100 differentially expressed features of Strain vs TD (a), No strain vs Strain (b), and No strain vs TD (c) comparisons. Dendrograms were drawn from Ward hierarchical clustering. Higher expression levels correspond to warmer colors.



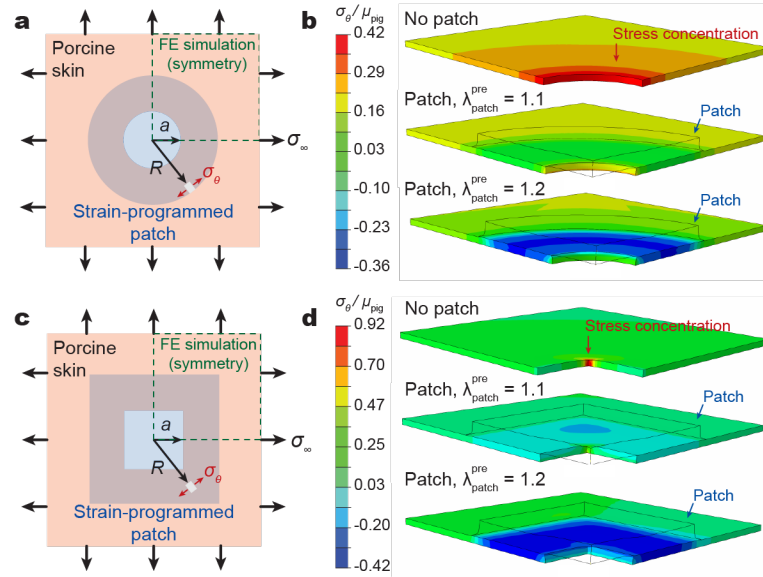
Supplementary Fig. 18 | No strain vs TD differential expression and functional analyses. a, Volcano plot displaying gene expression profile. Red colored data points represent genes that meet the thresholds of fold change (FC) above 1 or under -1 , False Discovery Rate (FDR) < 0.05 . **b,c**, Functional over-representation analysis utilizing the top 500 differentially expressed genes results in gene ontology (GO) (b) and Reactome (c) databases. The x-axis corresponds to the number of genes implicated in each pathway and the color of the bars correlates with the adjusted p values as shown in the legends. The p values are determined by one-sided Fisher's exact test and adjusted by Storey's correction method.



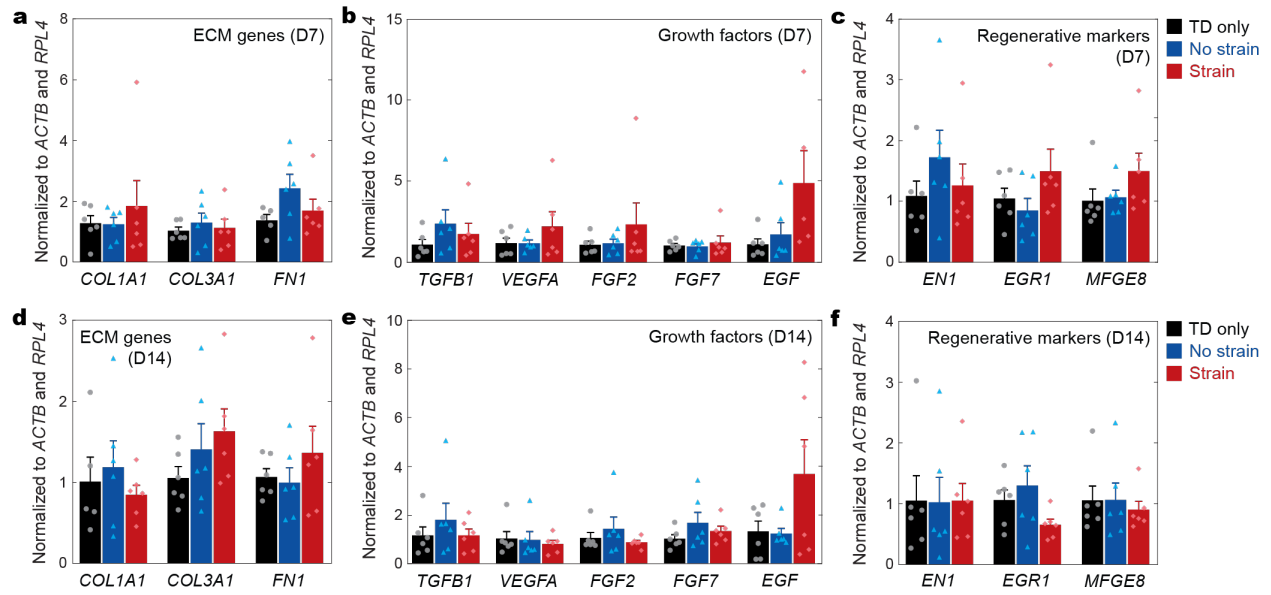
Supplementary Fig. 19 | Mouse wound bulk RNA-seq deconvolution using the GSE141814 scRNA-seq mouse dataset as reference. **a**, *t*-distributed stochastic neighbor embedding (tSNE) plot illustrating the annotated cell clusters of 13,169 single cells from the dermis of day 18 wounds in wound induced hair neogenesis (WIHN) model as reported in Gay *et. al*²² (GSE141814). **b**, CIBERSORTx abundance estimate of cell types accounting for at least 1% of cells in the scRNA-seq dataset in our bulk RNA-seq data reveals enrichment of the Myofibroblast II cluster (Myf2) in the strain-programmed patch treated wounds. Warmer colors denote higher expression. **c**, Top 10 significantly differentially expressed genes in the Myf2 cluster sorted by fold change descending order. **d**, Comparison of Myf2 gene expression signature between the strain-programmed and no strain patch treatments confirms enrichment of Myf2 in the strain-programmed patch treated wounds. The signature was constructed using all Myf2 marker genes in single-cell which had log-fold change over 1 and the signature score was computed as the mean of the expression of all markers in the two conditions. Gene Set Enrichment Analysis (GSEA) was used to assess the difference, revealing statistically significant difference in the signature's expression between the strain-programmed patch treated and no strain patch treated wounds. The box plot within the violin plot represents the median, 25th and 75th percentiles and the whiskers extend to maximum and minimum values; ($n = 3$ wounds for No Strain and 4 for Strain; independent samples).



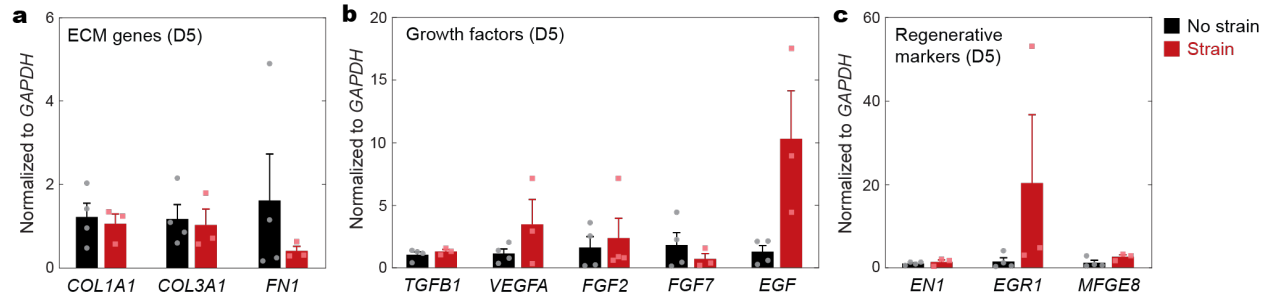
Supplementary Fig. 20 | Mechanical modulation of porcine skin wounds. **a**, Schematic illustration for the theoretical and finite-element analyses. **b,c**, Representative finite-element results (**b**) and the corresponding experiment images of the porcine skin (**c**) mechanically modulated by the strain-programmed patch ($\lambda_{\text{patch}}^{\text{pre}} = 1.3$; size = 3 times of the wound diameter). The shear modulus of the porcine skin is denoted as μ_{pig} , the hoop stress in the porcine skin as σ_θ , and the residual stress in the intact porcine skin as σ_∞ . **d**, Finite-element and experimental results for the wound closure ratio as a function of $\lambda_{\text{patch}}^{\text{pre}}$. **e,f**, Finite-element results for the hoop (σ_θ , **e**) and the radial (σ_r , **f**) stress around the wound for the strain-programmed patch with varying $\lambda_{\text{patch}}^{\text{pre}}$. Scale bars, 10 mm (**c**).



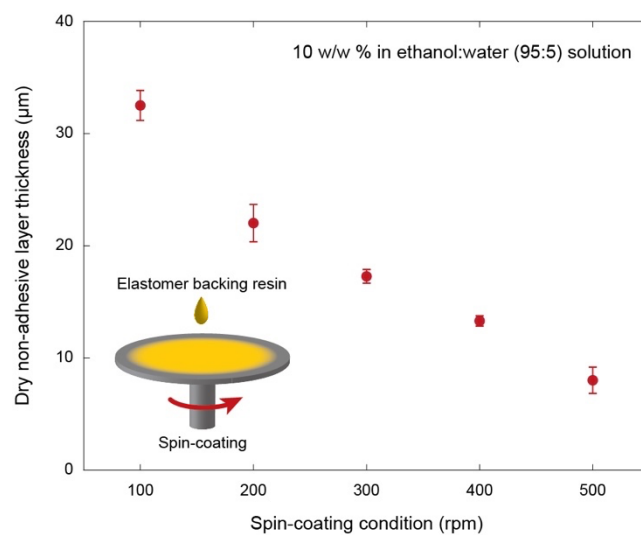
Supplementary Fig. 21 | Different wound geometries. **a,b**, Schematic illustration for the finite-element analysis (a) and the representative finite-element results (b) for porcine skin with circular wound mechanically modulated by the strain-programmed patch. **c,d**, Schematic illustration for the finite-element analysis (c) and the representative finite-element results (d) for porcine skin with square wound mechanically modulated by the strain-programmed patch.



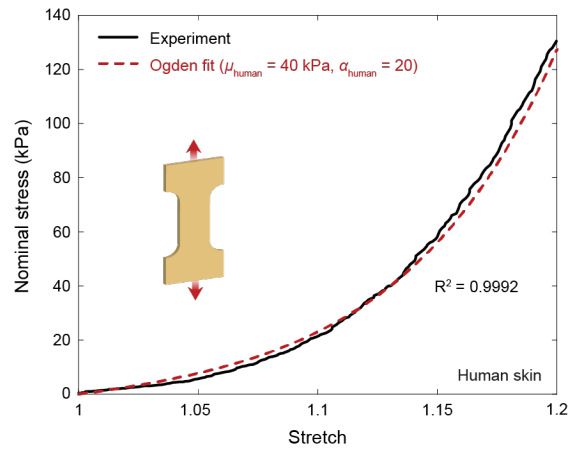
Supplementary Fig. 22 | RT-qPCR gene expression analysis of porcine wounds. a-c, RT-qPCR analysis on day 7 (D7) wounds for ECM-related (a), growth factor (b), and regenerative genes (c). **d-f,** RT-qPCR analysis on day 14 (D14) wounds for ECM-related (d), growth factor (e), and regenerative genes (f). Values represent the mean and the standard error of the mean ($n = 6$ for TD Only, 6 for No Strain and 6 for Strain, except for *FN1* where TD Only is 5 in **a**; $n = 6$ for TD Only, 6 for No Strain and 6 for Strain, except for *EGF* where Strain is 5 in **b**; $n = 6$ in **c**; $n = 6$ for TD Only, 6 for No Strain and 6 for Strain, except for *COL1A1* where TD Only is 5 in **d**; $n = 6$ in **e** and **f**; independent samples).



Supplementary Fig. 23 | RT-qPCR gene expression analysis of humanized mouse wounds. a-c, RT-qPCR analysis on day 5 wounds for ECM-related (a), growth factor (b), and regenerative (c) genes. Values represent the mean and the standard error of the mean ($n = 4$ for No Strain and 3 for Strain in **a** and **c**; $n = 4$ for No Strain and 3 for Strain, except for *FGF2* where Strain is 4 in **b**; independent samples).



Supplementary Fig. 24 | Spin-coating of backing layer. Values represent the mean and the standard deviation ($n = 4$; independent samples).



Supplementary Fig. 25 | Tensile properties of *ex vivo* human skin. Nominal stress vs. stretch curve for an *ex vivo* human skin fitted with the incompressible Ogden hyperelastic model.

Supplementary Data Captions

Supplementary Data 1 | Complete lists of differentially expressed genes from RNA-seq data.

Supplementary Data 2 | Complete list of the antibody cocktail for flow cytometry.

Supplementary Video Captions

Supplementary Video 1 | Rapid adhesion and closure of an *ex vivo* porcine skin wound by the strain-programmed patch.

Supplementary Video 2 | Rapid adhesion and closure of an incisional skin wound by the anisotropically strain-programmed patch.

Supplementary Video 3 | On-demand removal of the adhered patch from *ex vivo* porcine skin wound by applying a detachment solution.

Supplementary Video 4 | Rapid adhesion and closure of wound in a diabetic mouse skin by the strain-programmed patch.